Figure 5-12. Kriged porosity and **permeability (mD) for the B-C interbed.**
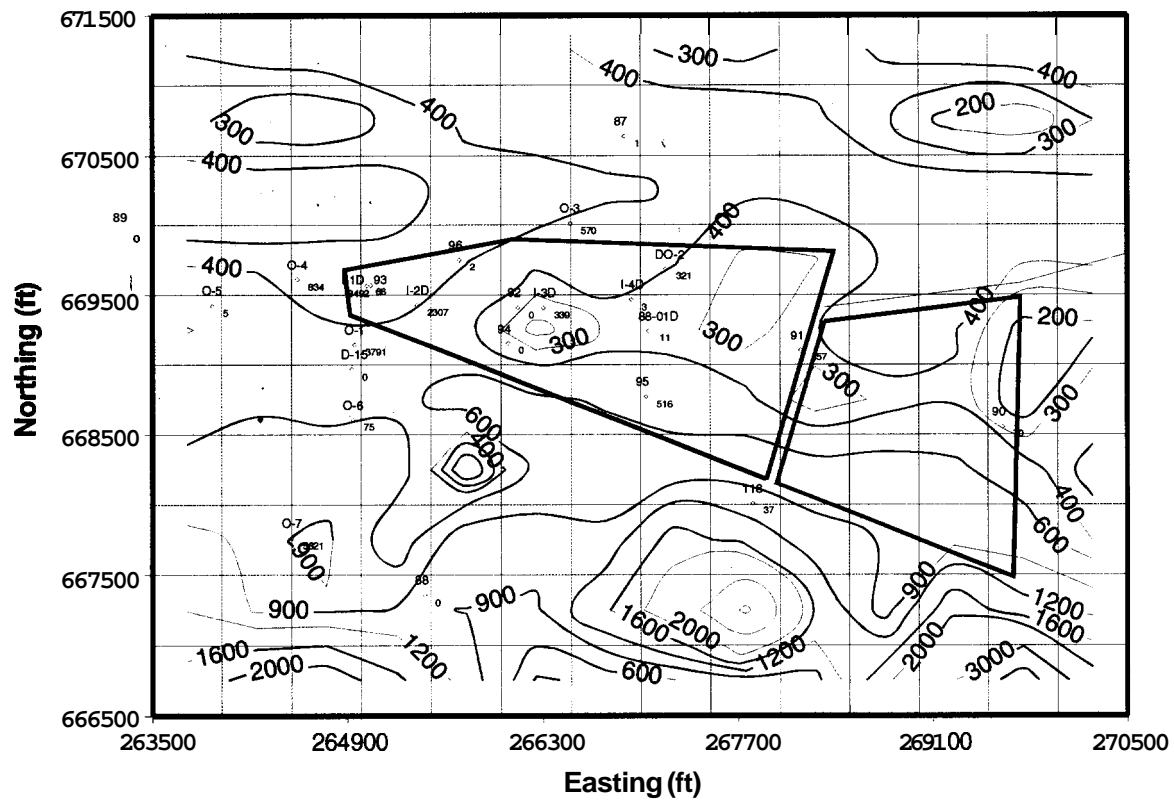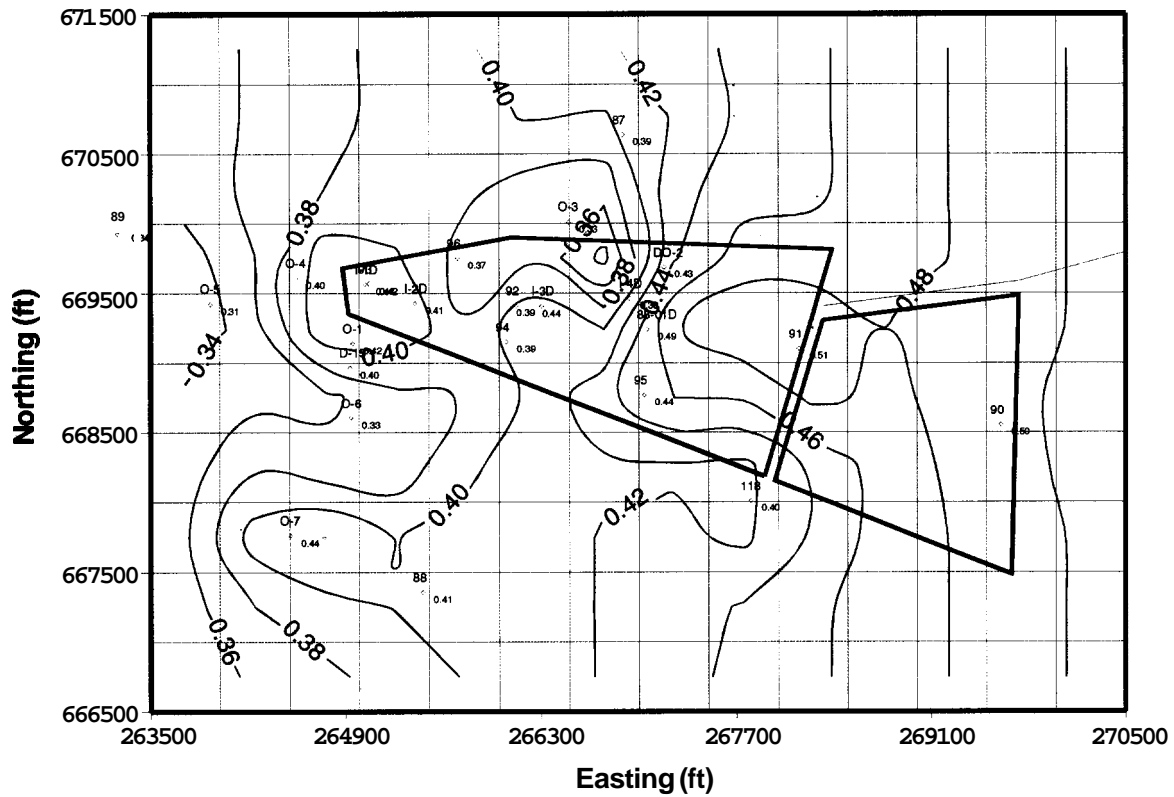
Figure 5-13. Kriged porosity and permeability (mD) for the C-D interbed.
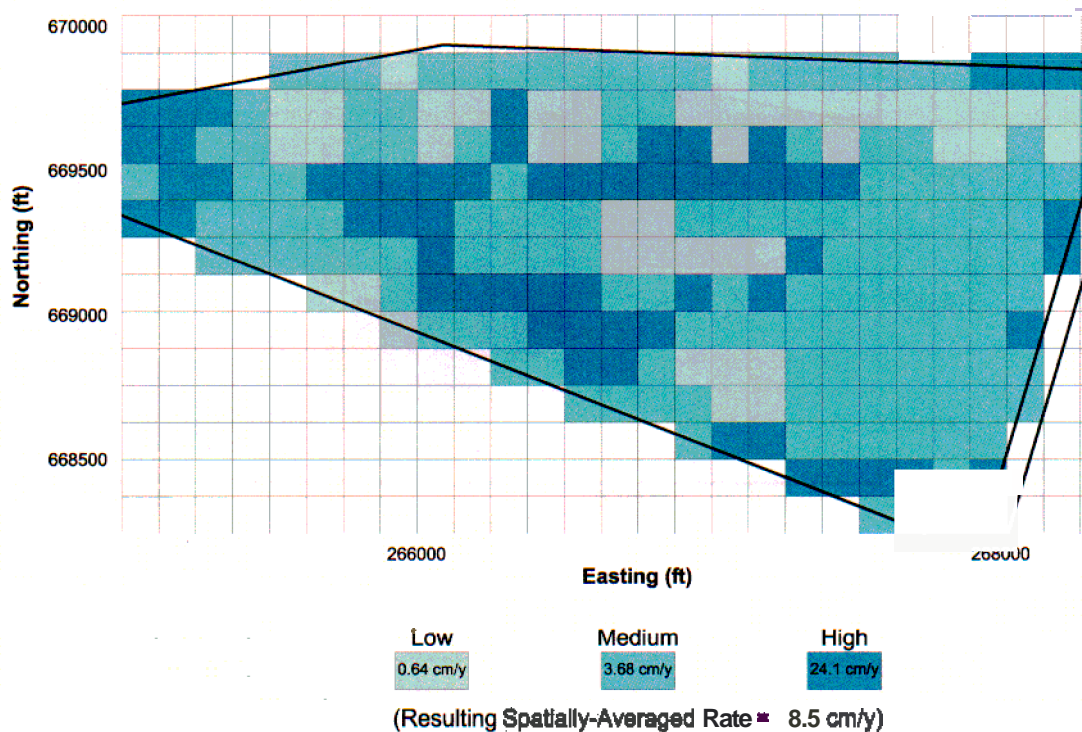
Figure 5-14. Spatially variable infiltration assignment for model domain inside the Subsurface Disposal Area.

Three historical flooding events have occurred at the SDA and also were included in the ABRA model, essentially using the same method as the IRA model but with slight differences caused by gridding. Figure 5-15 shows the locations where additional water was imposed at the surface for the 1962, 1969, and 1982 floods, respectively. Estimates of the amount of water that entered the SDA for each of the floods were taken from Vigil (1988) and are shown in Table 5-12. Each flood was assumed to last for 10 days.

Table 5-12. Historical flooding volumes and application rates at the Subsurface Disposal Area.

Year	Estimated Volume (acre-ft)	Infiltration Rate (m/day)
1962	30	2.26×10^{-2}
1969	20	1.68×10^{-2}
1982	8.3	1.24×10^{-2}

The lower boundary of the model domain was assigned a water table condition. Lateral boundaries were all assigned as no-flow boundaries. The addition of an assumed water source from the spreading areas is discussed below.

Initial conditions for all simulations were obtained by assigning an initial water saturation of 50% to the entire simulation domain. Then the simulation was run for 100,000 days (approximately 270 years) to let the system come into equilibrium. Water saturation in the C-D interbed was monitored to determine whether equilibrium had been obtained. After the first 20,000 days (approximately 55 years), the change in the saturation was negligible.
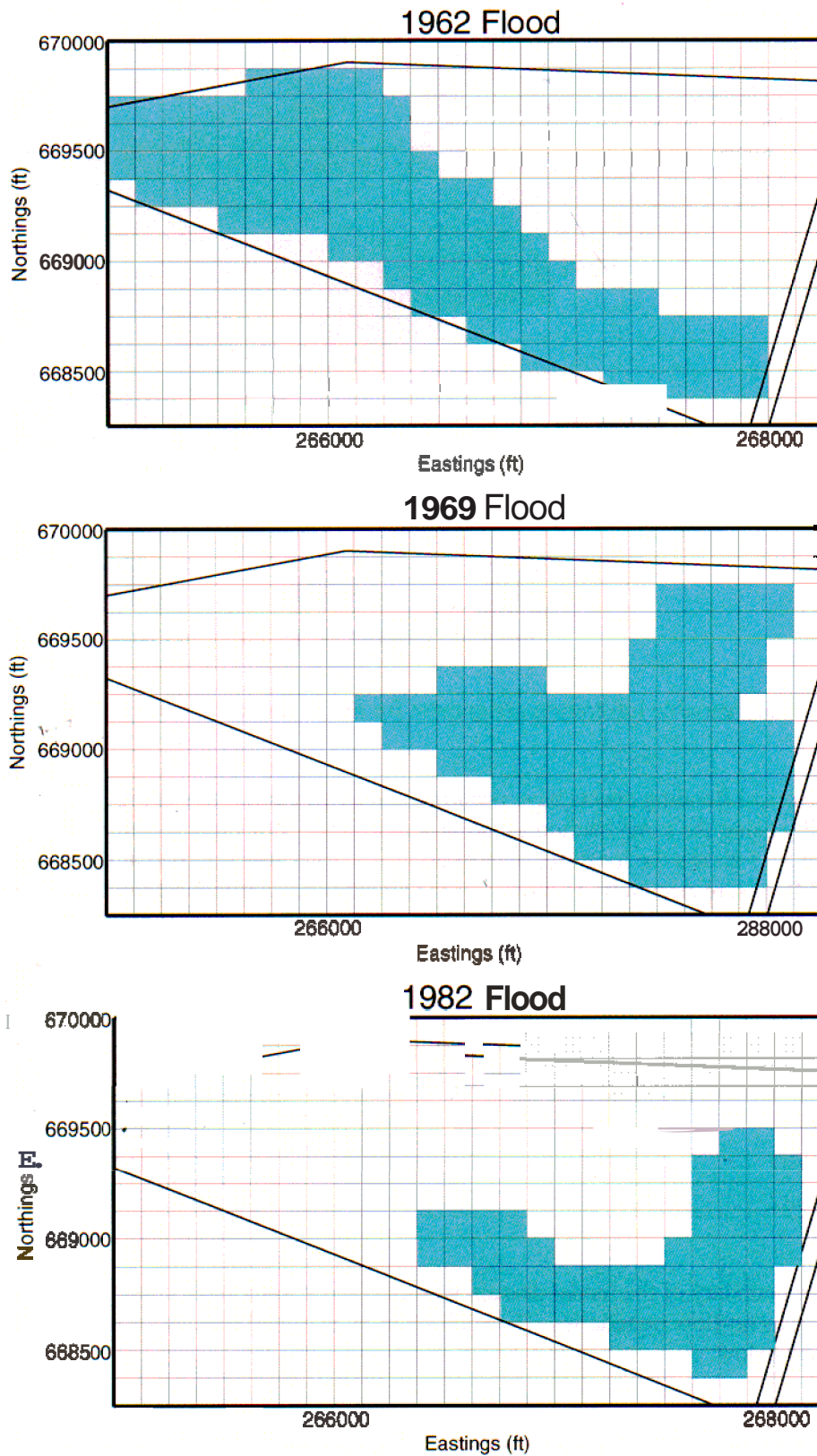
Figure 5-15. Locations of additional, water supplied by the 1962, 1969, and 1982 flooding events at the Subsurface Disposal Area.

5.2.4.3.6 Development Simulations—Simulations performed as part of the development of the ABRA model are discussed in this section.

5.2.4.3.7 Wetting FrontAdvancement at Well 76-5—The simulations presented in this section tested the appropriateness of the moisture characteristic curve used to represent the fractured basalt in the ABRA model. This same curve was used in the IRA model and in other modeling studies at the INEEL (Rodriguez et al. 1997). The use of this moisture characteristic curve has not been further investigated since it was introduced in Magnuson (1995). The testing summarized in this section provided evidence of the conservatism in the ABRA model caused by the moisture characteristic curve assigned for the fractured basalts.

A set of nested advanced tensiometers installed in Well 76-5 inside the SDA at depths of 6.7, 9.4, and 11.6 m (22, 31, and 38 ft) show changes in measured tension at each depth as a series of wetting fronts migrated downward during the period from February to April of 1999 {see Figure 5-16). The shallowest tensiometer is emplaced within fractured basalt (see Figure 5-17) and shows the influence of infiltrating water that appears to be three separate infiltration events, likely caused by snow melting at land surface. The middle tensiometer, at a depth of 9.4 m (31 ft), was emplaced within a thin interbed of approximately 15 cm (0.5 ft) thickness. The deeper tensiometer is located in fractured basalt beneath the thin interbed and shows some degree of damping of the infiltration fronts.
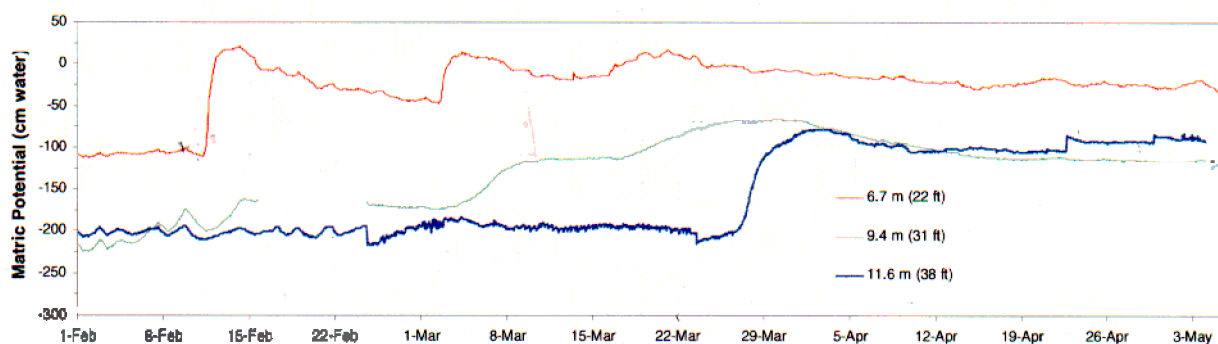

Figure 5-16. Tensiometric monitoring results in Well 76-5 during the winter and spring of 1999.

Three one-dimensional TETRAD simulations were implemented to compare simulated matric potentials to tensiometric monitoring data from Well 76-5. Figure 5-17 shows the onedimensional simulation grid juxtaposed with a well construction and instrumentation diagram for Well 76-5. The sediment moisture characteristic curve in each run was parameterized the same as that used for the ABRA model described above in Section 5.2.4.3.4. The first run applied the Corey-type fractured-basalt moisture characteristic curve implemented for the ABRA modeling. The second run applied a Corey-type moisture characteristic curve for the fractured basalt with lower capillary pressures. The third run simulated a fractured basalt van Genuchten moisture characteristic curve that partially mimics the ABRA Corey-type curve. The parameter values for the fractured basalt residual moisture content, van Genuchten alpha, and van Genuchten N were 0.001, 1.066 m^{-1}, and 1.523, respectively. The three moisture characteristic curves are shown in Figure 5-18. Initial conditions were obtained by imposing a background flux of 1 cm/year (0.4 in./year) of water for 100,000 days. Three pulses of water (related to melting events at the surface) were imposed at the top boundary by prescribing a first-type boundary condition consisting of saturated conditions for one day per melting event.
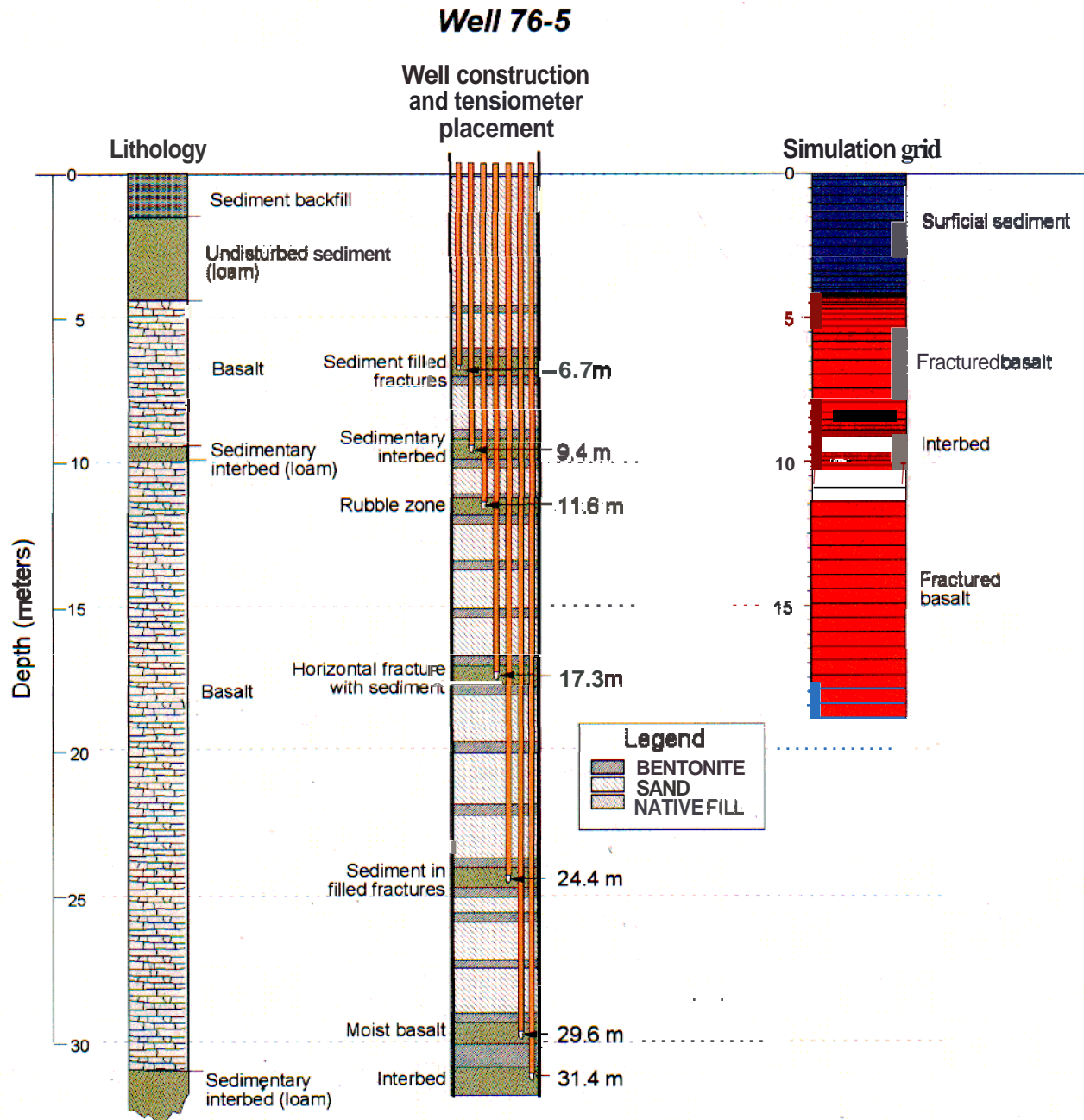
Well 76-5

Figure 5-17. Simulation grid for Well 76-1 with lithology and tensiometer monitoring locations.

The simulated matric potentials at equivalent depths for each of the three moisture characteristic curves are shown in Figure 5-19. Although there was considerable difference between the results, each simulation successfully mimicked some of the observed matric potential behavior. The results with the van Genuchten *curve* showed the lowest tensions (capillary pressures), which are more feasible in fractures than tensions indicated by either of the results from the Corey-type *curves.* The alternate Corey-type curve resulted from a desire to run the ABRA simulations without the resulting extremely high capillary pressures, However, numerical convergence could not be obtained when the alternate Corey-type curve was implemented in the full three-dimensional ABRA simulation.

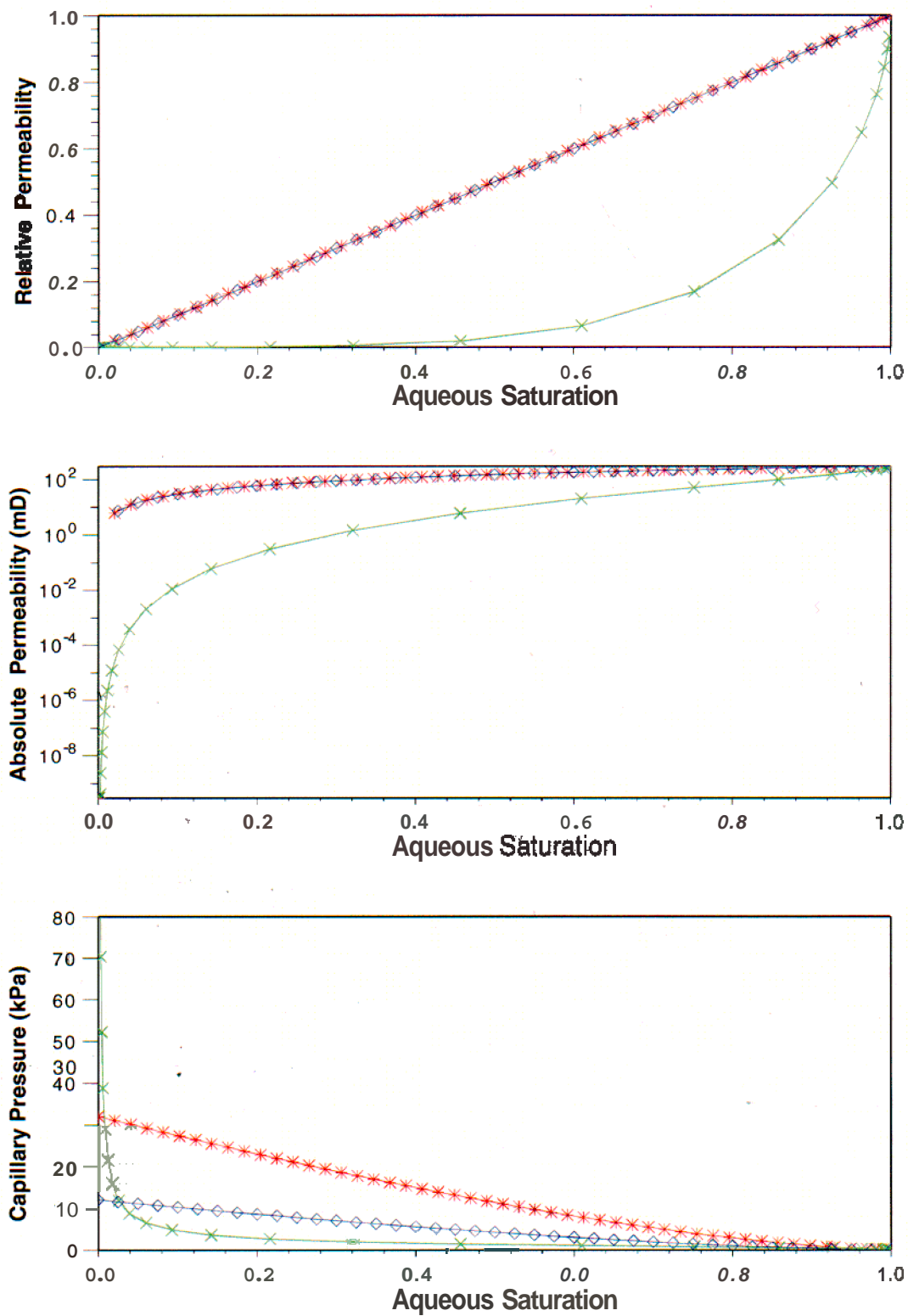Figure 5-18. Three moisture characteristic curves used in Well 76-5 infiltration simulation. The red asterisks represent the Corey-type moisture characteristic curve used in the ABRA simulations. The other two curves are an alternate Corey-type curve (blue diamonds) and a van Genuchten *curve* (green Xs).
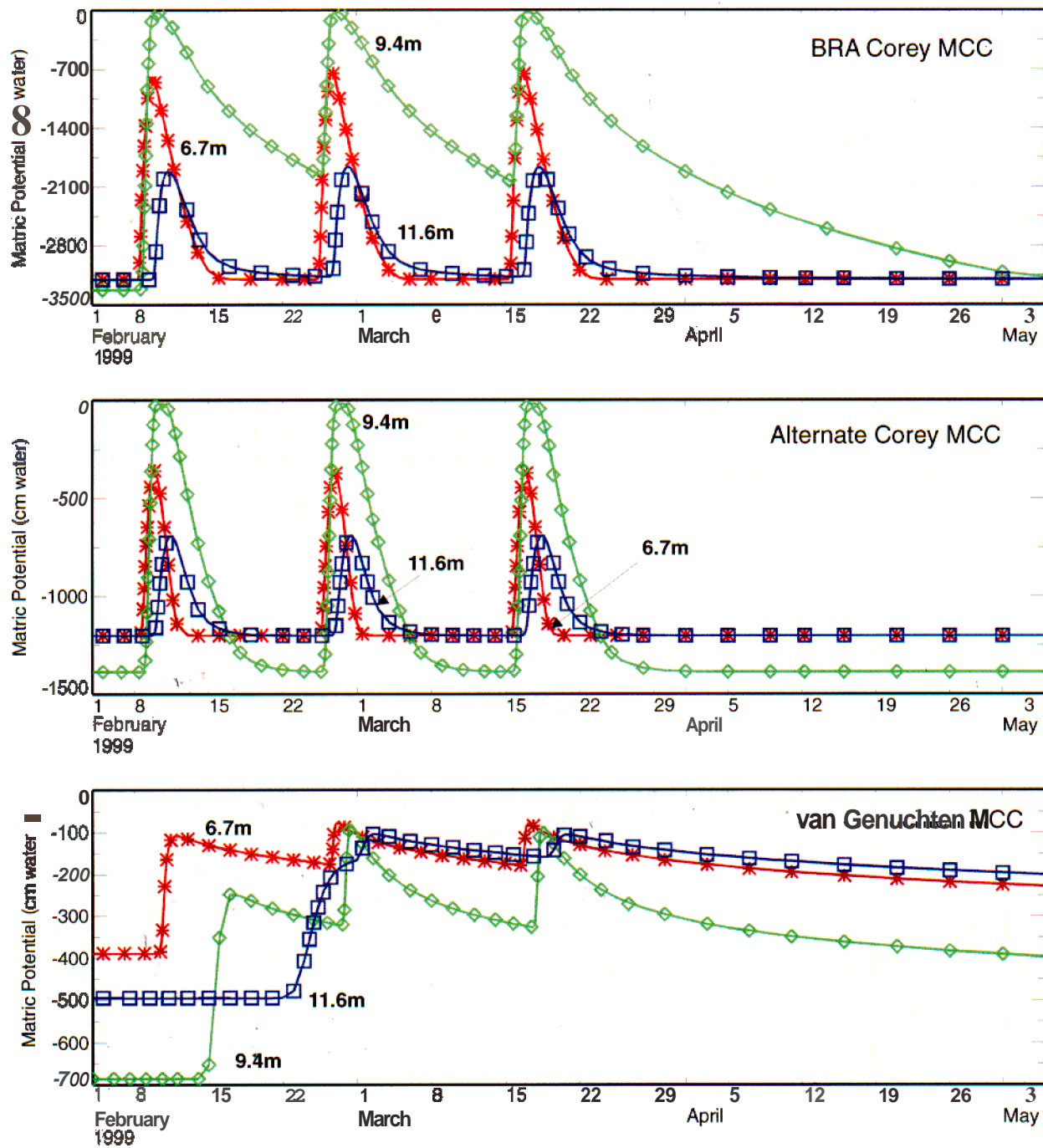
Figure **5-19. Simulated matric potentials** for **the** three **moisture characteristic curves.**

Using the van Genuchten curve, simulation results better matched the compounding behavior observed in the monitoring results where the second and third fronts resulted in increasingly wetter conditions at depth because the moisture accumulated from the earlier wetting events had not drained out of the system. Using either of the Corey-type simulations, the wetting front propagates more completely through the simulation domain for each wetting event.

To compare the three simulations, the resulting water flux at a depth of 11.6 m (38 ft) is shown for each simulation in Figure 5-20. Similar to what was seen in the matric potential results, fluxes with either of the Corey-type curves are much more compressed in time, yielding higher values and quicker penetration to depths greater than those observed in the field tensiometric monitoring. Therefore, the Corey-type curve for the fractured basalts used in the IRA model is demonstrably conservative with respect to maximizing water and contaminant movement downward through the fractured basalt. This same conservative Corey-type curve was applied in the ABRA modeling. Note that the use of first-type boundaries at the surface to impose the melting events does not require that the cumulative water flux down through the system to this depth be the same for each of the three simulations.

An alternative suite of simulations was performed to investigate the effect of using second-type prescribed fluxes as the upper boundary condition representing each melting event. The amount of water applied for each event was 2.54 cm (1 in.) over a 1-day duration. Results shown in Figure 5-21 were similar to those using first-type conditions because the Corey-type curves both allowed much faster propagation of water fronts down through the system. The time axis in Figure 5-21 was extended the full length of the 200-day simulation period to allow the flux curve resulting from the van Genuchten curve to be partially seen on the plot.

5.2.4.3.8   Spreading Area Influence in the Vadose *Zone*—The base case model for the ABRA includes the influence of water entering the domain in the vadose zone at the C-D interbed from the spreading areas. The decision to include spreading area effects resulted from the tracer test conducted by the USGS in 1999 (Nimmo et al. 2002). In that test, perched water sampled from Well 92 in the vadose zone beneath the SDA yielded a tracer within 90 days after it was applied in the spreading areas during a period when water was diverted from the Big Lost River to both Spreading Areas A and B. In the implementation for the ABRA model, the additional water that entered the simulation domain was assumed to be located just above the C-D interbed and to affect only the western portion of the C-D interbed beneath the SDA.

To mimic these effects, the initial vadose zone domain was defined to include the spreading areas. When simulations with the resulting grid from that domain were impractical, it was necessary to use a smaller domain, which did not include the spreading areas. To implement the additional spreading-area water into the simulation it was necessary to assign an amount of water, a location to apply the water, and a duration for the application. The latter is not important in the use of the ABRA model for long-term predictive simulations because they consider only a steady-state influence at depth.

A series of transient simulations was made in which additional water was added above the C-D interbed at two different locations. These simulations used the model developed above as the starting point. One of the locations, chosen to mimic Spreading Area A, was defined as two grid blocks along the central portion of the western simulation boundary. The other location represented Spreading Area B and was defined as three grid blocks along the southern boundary of the domain beginning in the extreme southwestern corner. The approximate length of time that water was present in the spreading areas in 1999 was 60 days (Nimmo et al. 2002). Amounts of water representing 0.04, 0.08, 0.2 and 0.4% of the water discharged to Spreading Area A in 1999 were applied over 60 days to the first location. Similarly, amounts of water representing 0.02, 0.05, 0.1 and 0.2% of the water discharged to Spreading Area B in 1999 were applied at the second location.
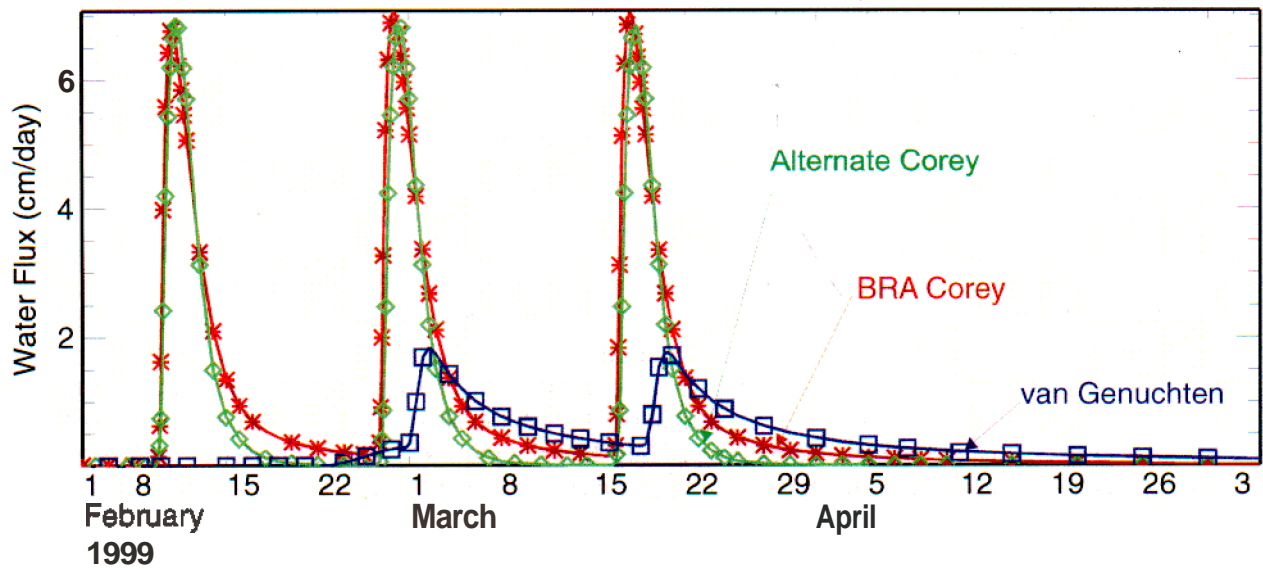
Figure 5-20. Simulated water fluxes at 11.6-m (38-ft) depth beneath a thin interbed for the three moisture characteristic curves using first-type prescribed saturation conditions for melting events,
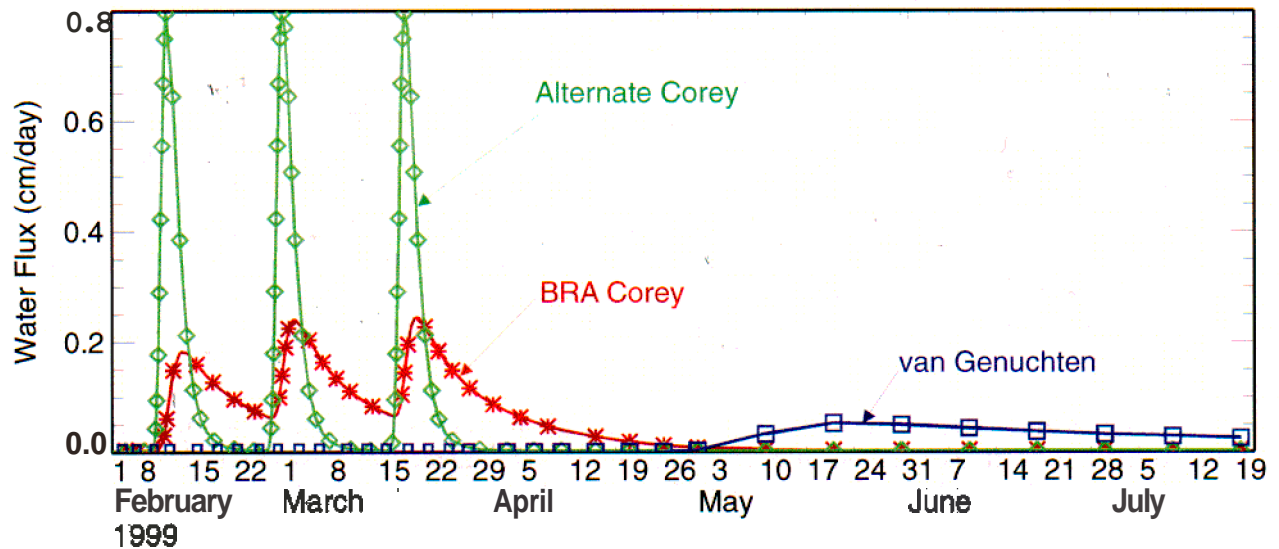

Figure 5-21. Simulated water fluxes at 11.6-m (38-ft) depth for the three moisture characteristic curves using second-type prescribed flux conditions for the melting events.

The varying slope of the **C-D** interbed had a large influence on the simulation results. The location chosen to represent Spreading Area **A** was slightly upgradient from the **SDA** compared to the location for Spreading Area B, which was off gradient. This resulted in Spreading Area **A** water easily reaching Well 92 within 90 days, while the larger amounts of water applied at the Spreading Area B location never advanced to the location of Well 92. Figures 5-22 and 5-23 show the simulation results at 90 days for each case. The contour lines show the relative fraction of water from the spreading areas compared to total water present. Well 92 is in the west-central portion of the **SDA** and is just touched by the 0.01 isoline. This **1%** concentration is approximately the same as the tracer concentration observed in Well 92 compared to the input concentration in the spreading areas (Nimmo et al. 2002). Though not conclusive, comparison of these simulation results implies that Spreading Area **A** is the source of water affecting the vadose zone beneath the **SDA.** The location that was used to represent Spreading Area **A** was chosen for use in the steady-state **ABRA** simulations. By choosing the Spreading Area **A** location, an influence from spreading-area water beneath the **SDA** is reflected in the simulation, regardless of whether the actual influence is from Spreading Area **A** or B.
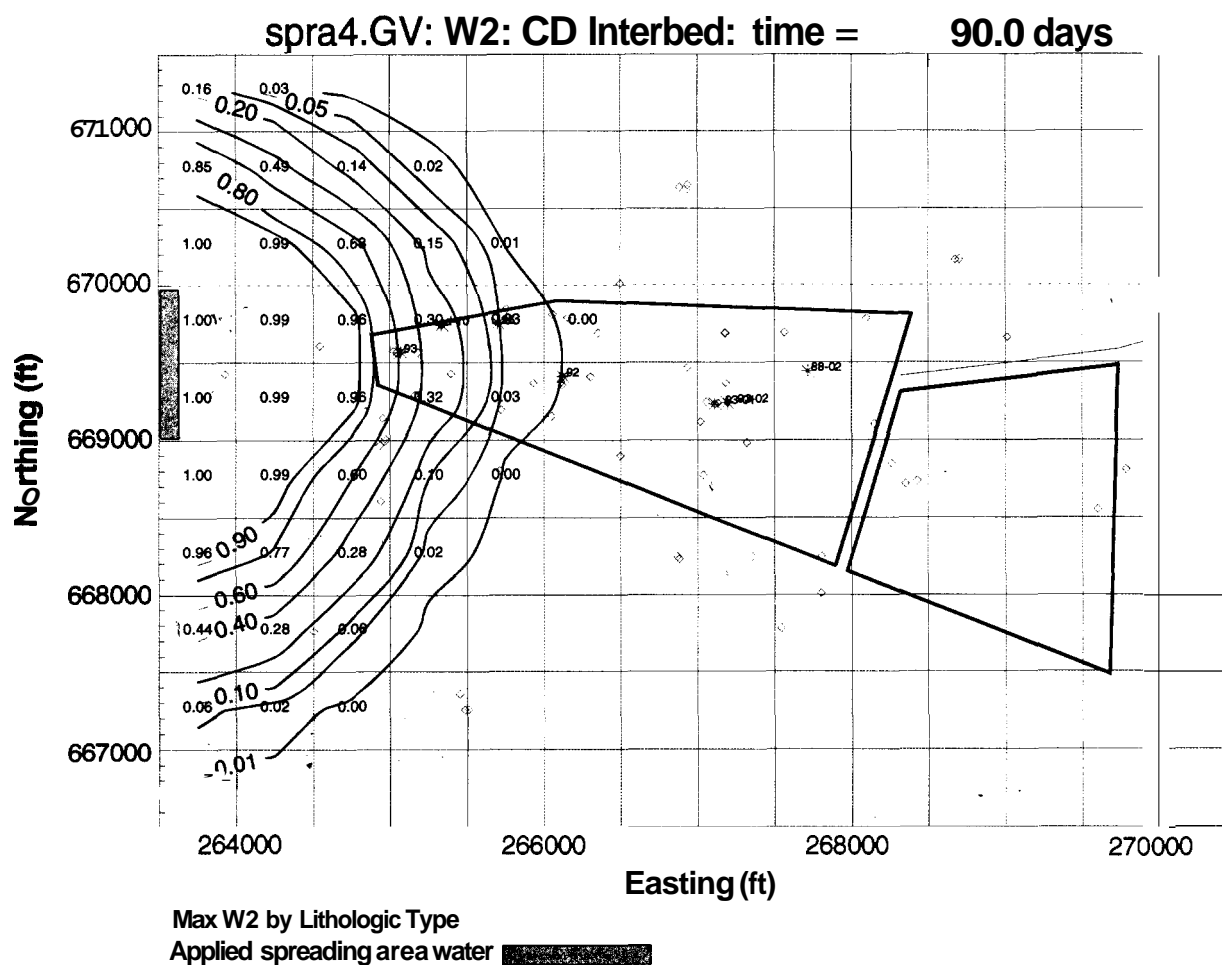

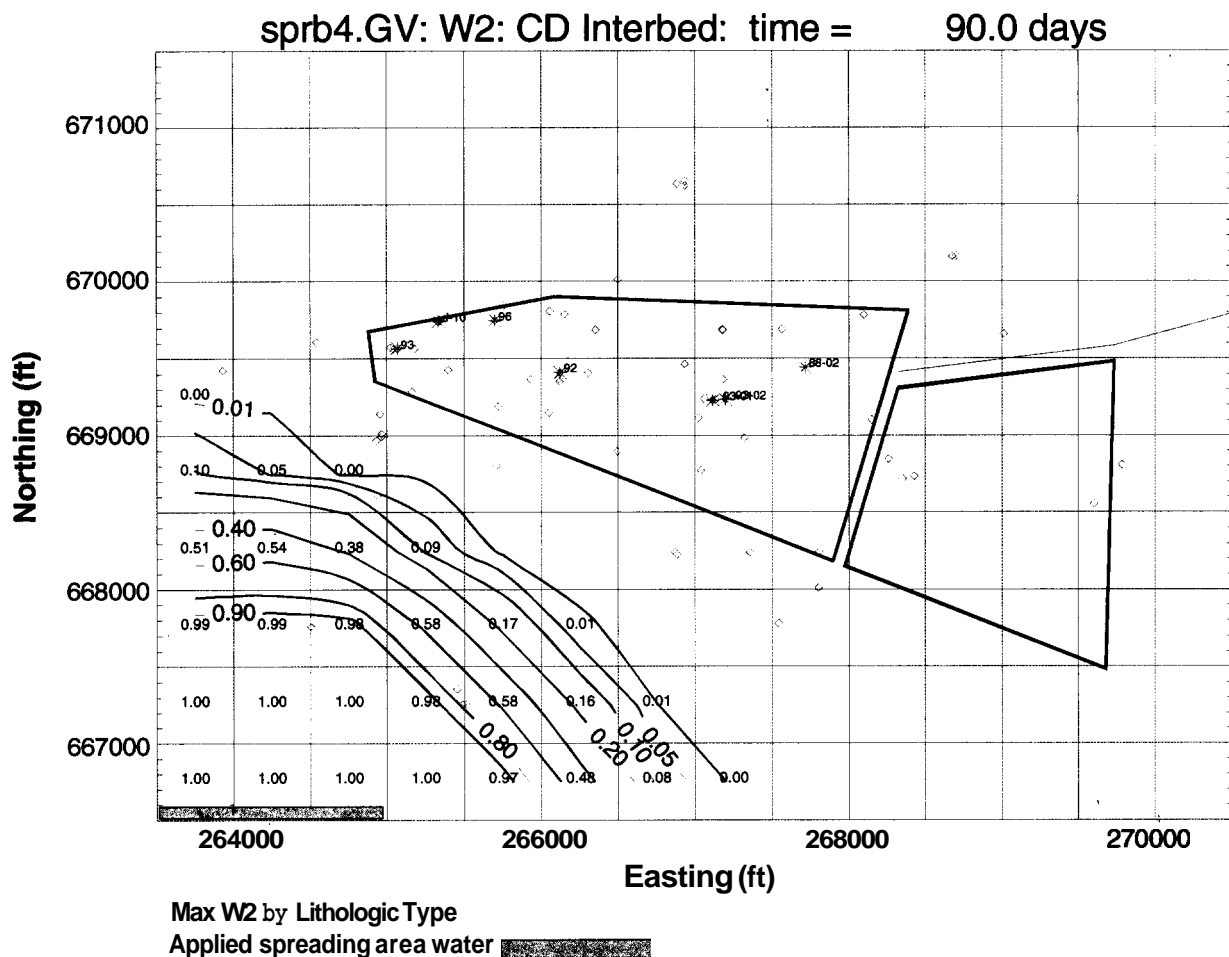Figure 5-22. Transient simulation results with water applied at Spreading Area **A.**

sprb4.GV: W2: CD Interbed: time = 90.0 days

Figure **5-23.** Transient simulation results with water applied at Spreading Area B.

The next series of simulation results (Figures **5-24, 5-25, 5-26, 5-27,** and **5-28)** indicates the sensitivity of the modeling results to the magnitude of applied spreading-area water volumes. Amounts of **1, 2, 3, 4,** and **8** acre-ft of water per day in perpetuity were evaluated. Simulations were run for **10,000** days to obtain steady-state conditions. Results shown in the figures depict relative presence of spreading-area water within the C-D interbed. As greater amounts of water are added at the western boundary, the spreading-area water spreads farther eastward because the simulated upper surface of the C-D interbed slopes east-southeast. Horizontal no-flux boundaries also impact solutions by keeping water within the simulation domain, as can be seen in the refraction of the isolines, especially along the northern boundary. In general, good modeling practice proscribes having the boundary condition influence the simulation results. However, in this case the proximity of the boundaries helps achieve the goal described earlier in this subsection of obtaining a spreading area influence under the western portion of the SDA.

Simulation with an additional **1** acre-ft **(1,233 m^3)** per day applied at the western boundary was selected for further use in the ABRA model. The **0.01** isoline bisects the SDA west to east, indicating that all locations west of this line exhibit some impact from the spreading-area water. The spreading area influence in the base case is implemented at the beginning of **1965** when the first significant flows in the Big Lost River occurred since it was constructed in **1958** (Wood **1989).** The history of diversions from the Big Lost River to the spreading areas is presented in Figure **5-29.**

Figure 5-24. Relative presence of spreading-area water with 1 acre-ft/day steady-state application. (This simulation was selected for the baseline risk assessment base case.)

Figure 5-25. Relative presence of spreading-area water with 2 acre-ft/day steady-state application.

Figure 5-26. Relative presence of spreading-area water with 3 acre-ft/day steady-state application.

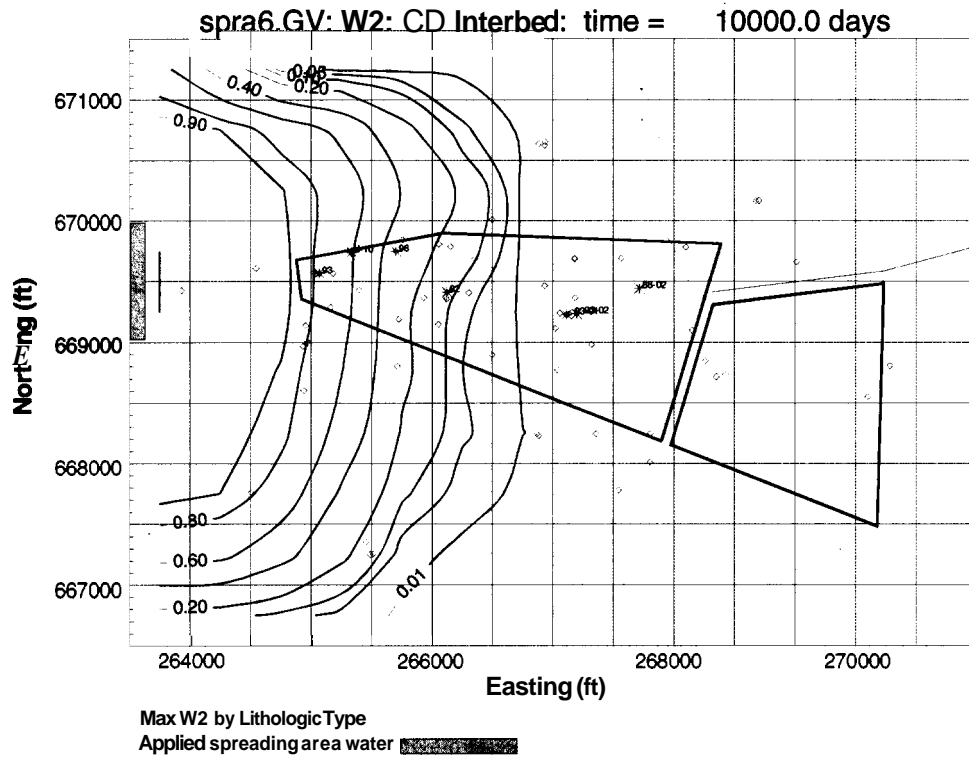**Figure 5-27. Relative presence of spreading-area water with 4 acre-ft/day steady-state application.** (This simulation was selected for the sensitivity evaluation of twice the spreading area effect.)
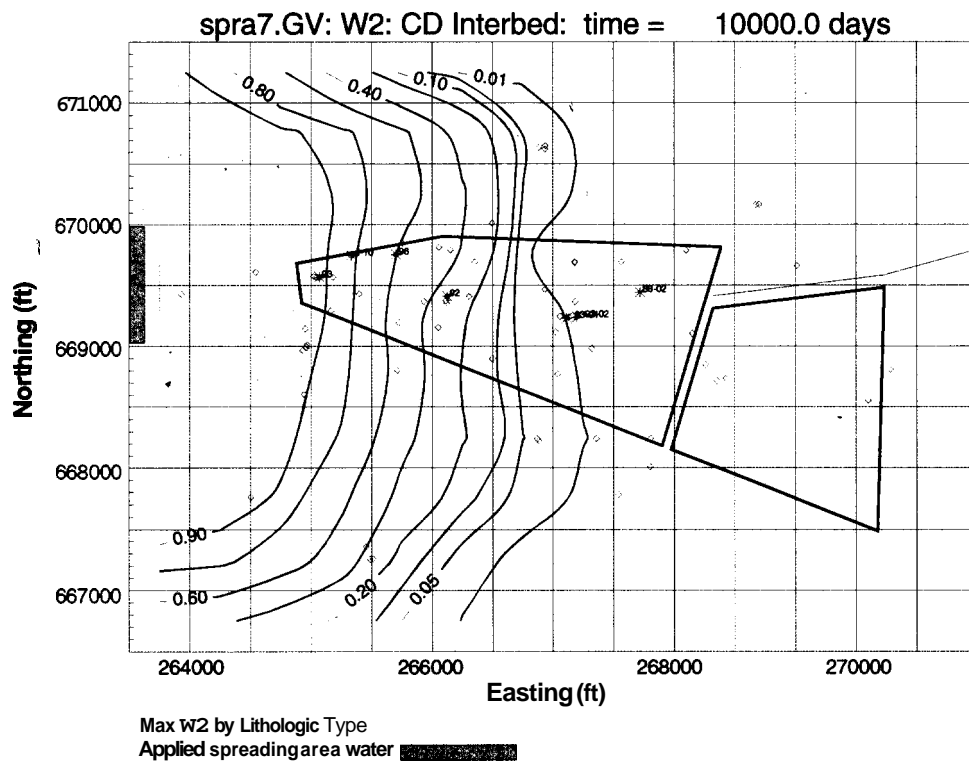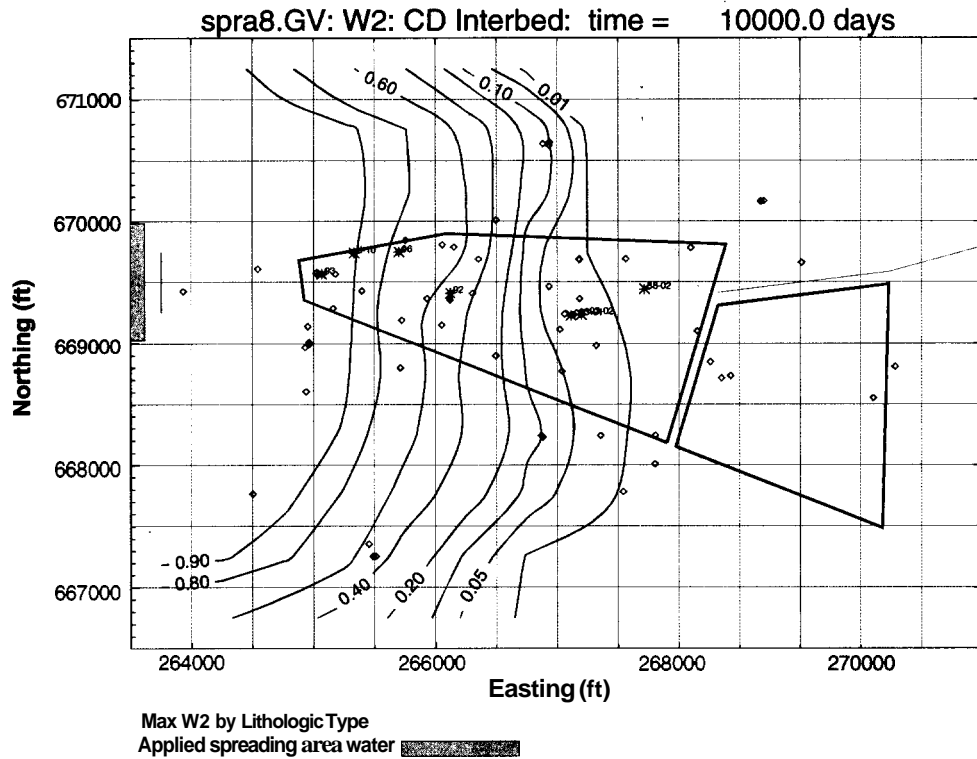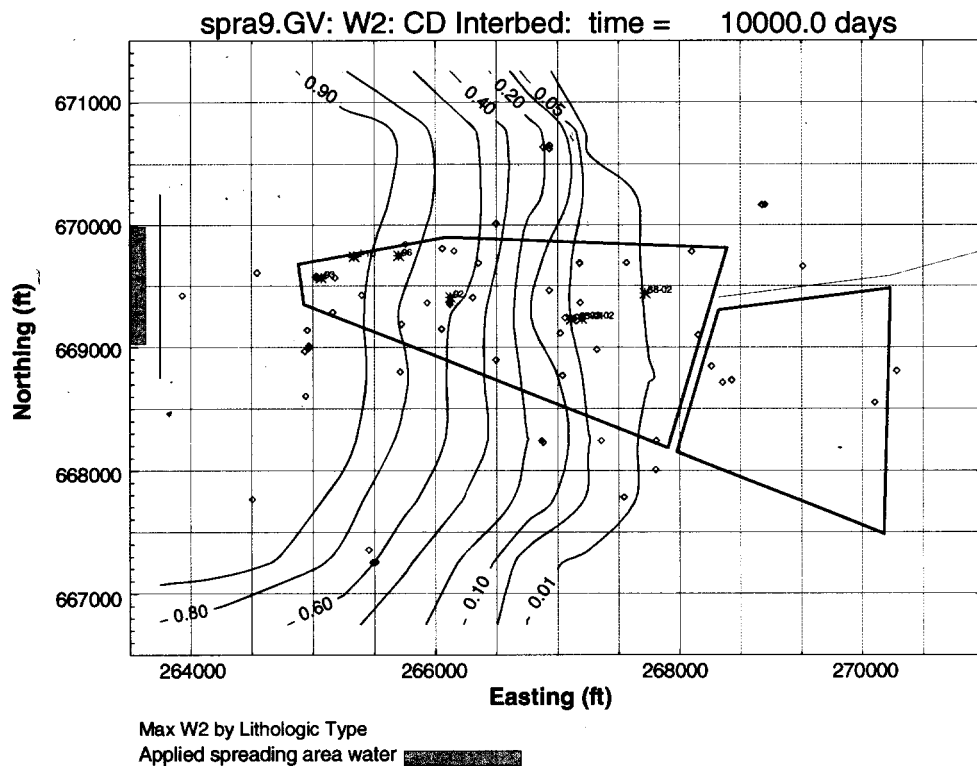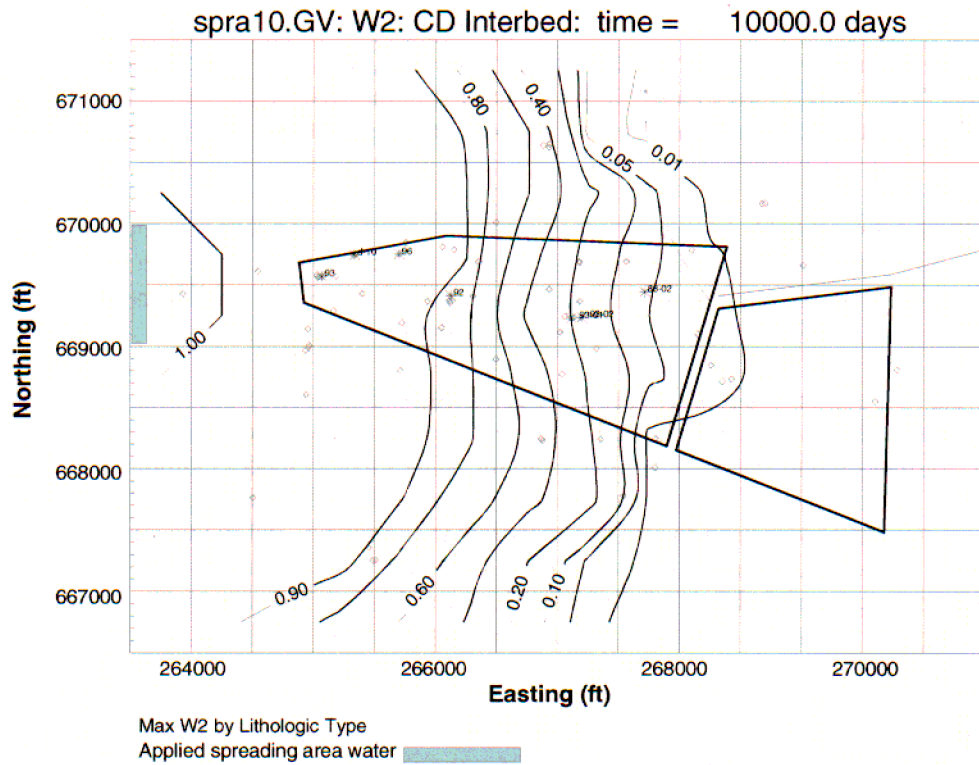
Figure 5-28. Relative presence of spreading-area water with 8 acre-ft/day steady-state application. .
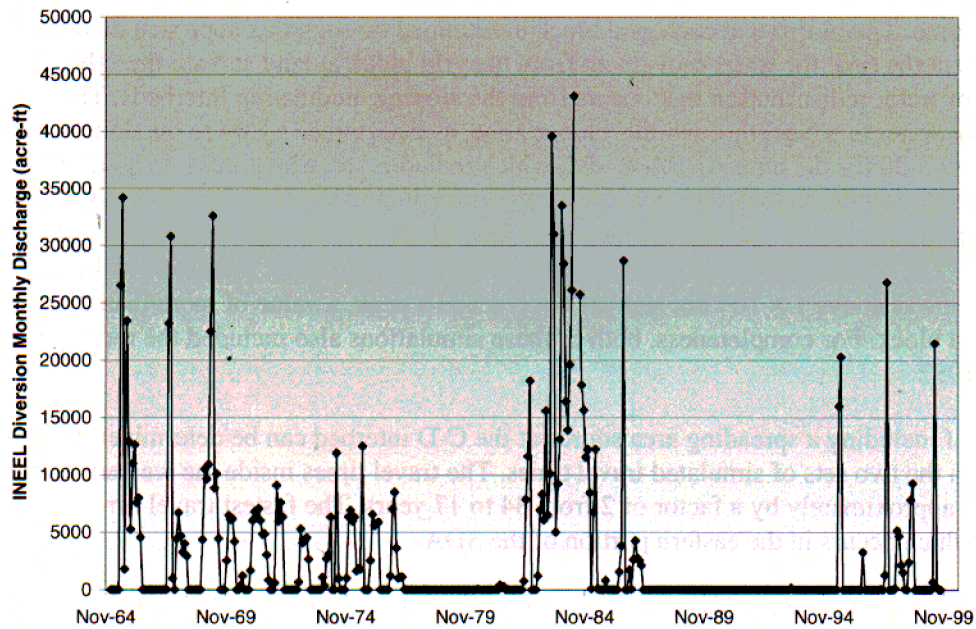

Figure 5-29. Historical diversion of Big Lost River water to the spreading areas from 1965 through 1999.

Historical data were obtained from the USGS web site (http://water.usgs.gov/id/nwis)(USGS 2001). The overall average monthly diversion for the data in the figure is 3,000 acre-ft/month, which equates to 100 acre-ft/day. The 1 acre-ft/day amount of water applied in the ABRA simulations represents 1% of the overall average diversion, which is a reasonable proportion to apply to ensure an impact beneath the SDA in the model.

One scenario evaluated below in the sensitivity analyses involved investigating the effect of twice the impact of spreading-area water on predicted contaminant migration. Rather than simply doubling the amount of water applied, the simulation with 4× the amount of water was selected because it showed an impact over nearly all the SDA, which effectively doubled the impacted area.

5.2.4.3.9 *Vadose* Zone Water Travel Times—This section provides a discussion of simulated water travel times through the vadose zone. Because no incontrovertible evidence exists to demonstrate required time to reach the aquifer from the SDA surface, model calibration is indirect and uncertain at best. Best-available knowledge based on site-specific information on infiltration, lithology, and hydrologic properties was used to assign parameters in the model, and the water travel time through the vadose zone was a simulation result. Because the simulated vadose zone water travel times impact dissolved-phase transport of mobile contaminants, these resulting vadose zone water travel times are of interest and are presented in this section. A comparison also is made to the vadose zone water travel times that resulted from the IRA model.

Travel times for the ABRA model were determined using the same method as was used for the IRA model. Starting from an equilibrium condition in 1952, the spatially distributed infiltration at land surface inside the SDA was applied as a separate nonsorbing tracer component for the first 1,000 days. At each grid block location at the bottom of the vadose zone simulation domain, the breakthrough curve for the tracer component was evaluated to determine the peak value. The time corresponding to this peak value was then decreased by 500 days, the midpoint of the initial application pulse, to determine the vadose zone water travel time. Travel times at each grid block determined through this approach do not necessarily represent the time for water movement from the grid block at land surface directly above each location because of water redistribution that occurs from the sloping, undulating interbeds. The travel times (in years) for water to advect through the vadose zone, as determined by these breakthrough curves, are shown in Figure 5-30 for the base ABRA model, which includes spreading areas. In addition, travel times are shown for a simulation that does not include the spreading areas. If the maximum value was less than a relative fraction of 1×10^{-6}, the travel time to that grid block was not determined and is represented by the symbol: **. The simulation was truncated at 100,000 days (272 years); therefore, if the breakthrough curve was above 1×10^{-6} but had yet not reached a peak, a value of more than 272 years is shown for that grid block. For completeness, both of these simulations also included the three floods of 1962, 1969, and 1982.

The effect of including a spreading area source at the C-D interbed can be determined from the difference between the two sets of simulated travel times. The travel times inside the western portion of the SDA decrease approximately by a factor of 2 from 34 to 17 years. The fastest travel time in either case is **14** years, which occurs in the eastern portion of the SDA.

For comparison to the current ABRA model, Figure 5-31 shows the simulated travel times from the IRA model, for which the fastest water travel time through the vadose zone was 23 years. Therefore, the revisions to the IRA model implemented in this ABRA model result in shorter simulated water travel times through the vadose zone. The extremely long 210-year vadose zone water travel time in the west-central portion of the SDA from the IRA model is completely absent in the ABRA modeling results.

rb.GV: W2: Breakthrough (Years) at Depth = 521.1 ft

Northing (ft) vs Easting (ft)

**	**	**	>272	>272	234	106	223	>272	**	**	**	**	
**	**	67	39	93	116	64	132	209	160	151	**	**	**
**	64	50	24	41	61	42	83	114	109	143	154	**	**
**	13	13	17	26	43	23	32	49	50	86	132	195	228
12	13	13	17	17	28	15	14	28	35	68	127	173	228
**	13	35	35	30	50	30	21	24	21	91	98	168	231
**	15	50	58	84	72	49	19	26	46	73	94	120	250
**	110	64	84	98	105	124	93	108	124	132	154	173	269
**	**	90	109	116	140	165	130	124	146	157	**	212	253
**	**	138	160	193	184	203	**	130	**	**	**	**	**

Easting (ft): 263500 — 265250 — 267000 — 268750 — 270500
Northing (ft): 671500, 670500, 669500, 668500, 667500, 666500

rbnsa.GV: W2: Breakthrough (Years) at Depth = 521.1 ft

**	**	**	>272	>272	247	106	214	>272	**	**	**	**	**
**	>272	179	>272	236	143	62	132	212	157	151	**	**	**
**	193	112	50	53	71	43	84	114	110	146	154	**	**
143	53	41	32	32	47	23	32	49	60	87	132	195	231
124	57	46	34	21	30	15	14	28	35	68	127	173	228
146	110	79	54	38	53	30	21	24	22	93	98	171	231
**	173	108	98	99	76	50	19	25	46	75	88	121	250
**	231	157	124	113	110	130	95	108	124	132	157	171	269
**	**	171	143	127	143	162	135	127	146	154	**	214	255
**	**	**	187	217	184	198	**	132	**	**	**	**	**

Easting (ft): 263500 — 265250 — 267000 — 268750 — 270500
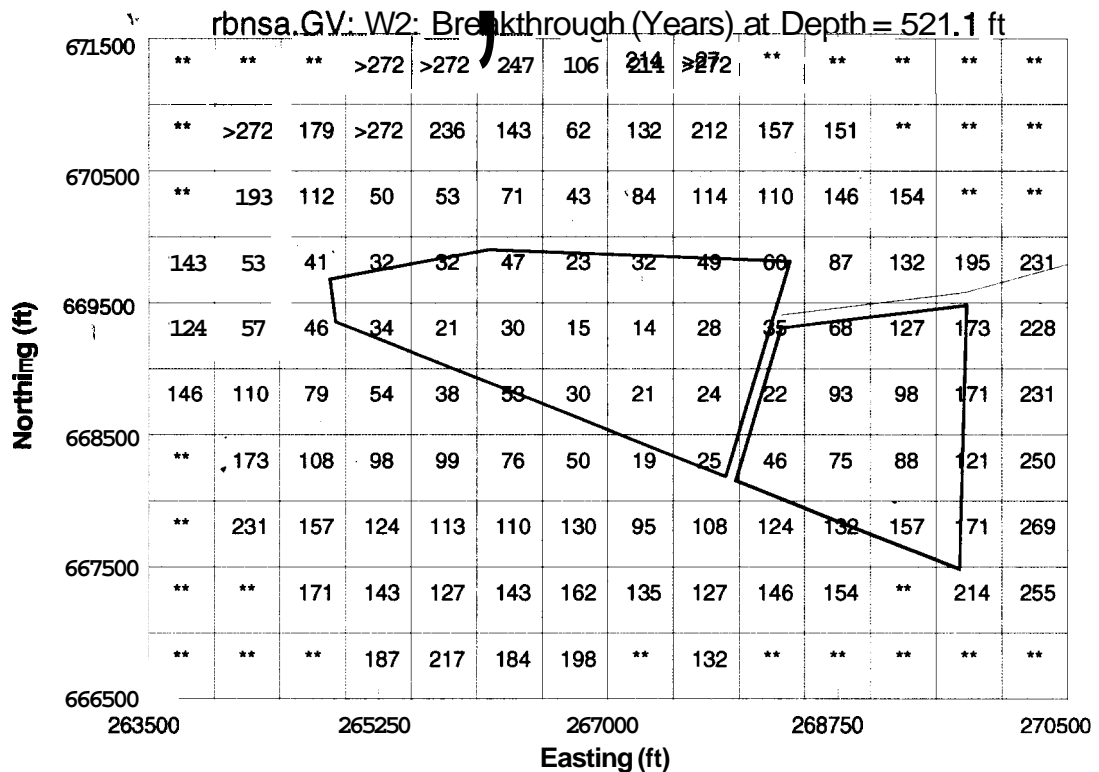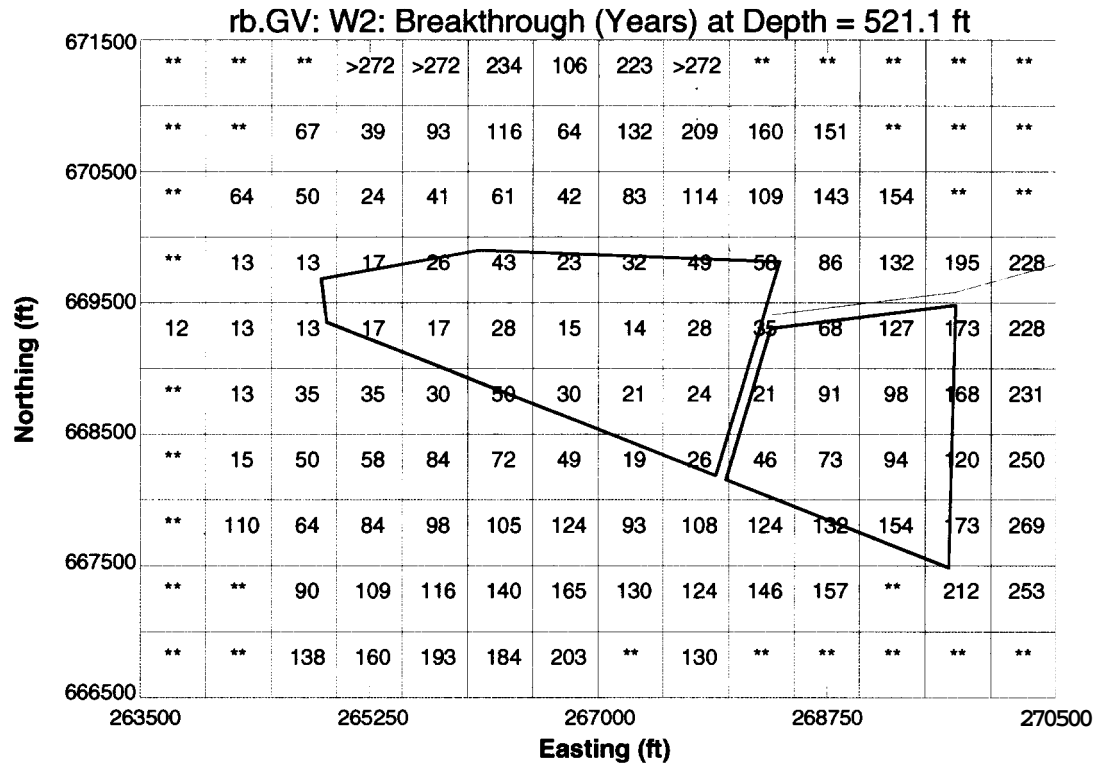Northing (ft): 671500, 670500, 669500, 668500, 667500, 666500

Figure 5-30. Water travel times in years through the vadose zone for the Ancillary Basis for Risk Analysis simulation (top) and for a case without an assumed spreading area influence (bottom).

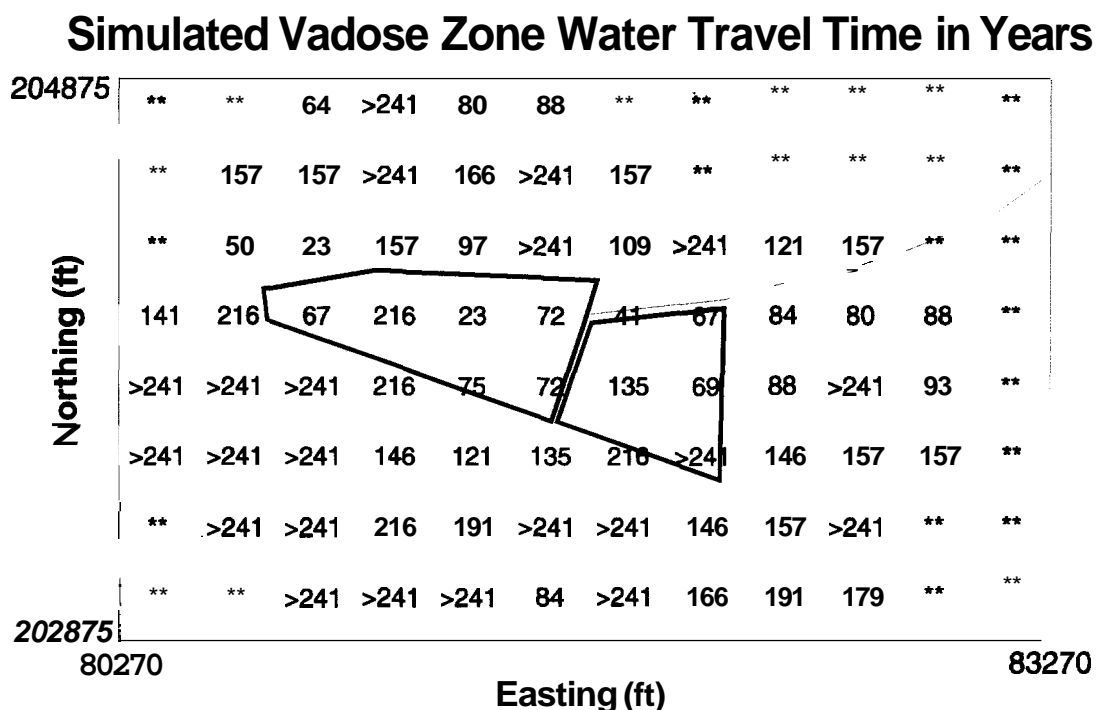## Simulated Vadose Zone Water Travel Time in Years

Figure 5-31. Simulated water travel times from the Interim Risk Assessment model.

Primary causes for reducing vadose zone water travel time were: (a) including the spatially variable hydrologic properties in the B-C and C-D interbeds, (b) the additional grid refinement in the ABRA model, and (c) using the conformable gridding approach that more closely matches the lithologic contacts between the sedimentary and fractured basalt portions of the subsurface. The application of spatially variable infiltration inside the SDA is essentially the same between models.

5.2.4.3.10 Vadose Zone lnterbed Moisture *Contents*—The last topic presented in the development of the vadose zone transport model is the simulation results for moisture content in the interbeds. Figure 5-32 shows the maximum water saturation for the most refined grid in calendar year 2001 for the B-C and C-D interbeds, respectively. All locations where perched water has been detected are shown in orange for comparison. The simulation results for calendar year 2001 reflect steady-state saturations well after the 1982 flood.

The areas of elevated moisture content partially mimic the distribution of known perched water locations. Less apparent is the control exerted by the presence or absence of the A-B interbed. The regions in the B-C interbed where the moisture content is elevated generally correspond to where the A-B interbed is absent or is very thin. This same behavior persists down into the C-D interbed, but is less obvious because of the influence of the additional water added in the simulation to represent a spreading area influence.

In the simulation results, the location containing Well 92 is still in a region of lower water content. Perched water has been observed continuously in this well since it was drilled in 1992. The proximity of the simulated elevated saturation region immediately to the west of Well 92 (see the lower plot in Figure 5-32) implies that the continuous presence of water in Well 92 could be attributed to spreading area influences.
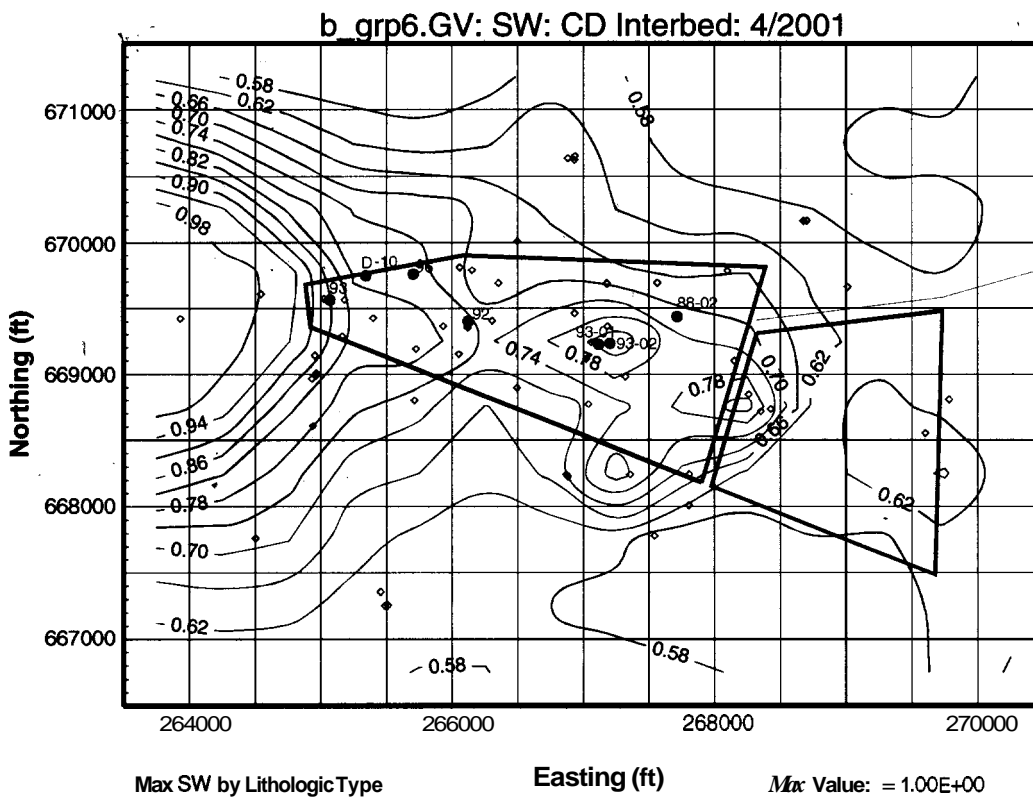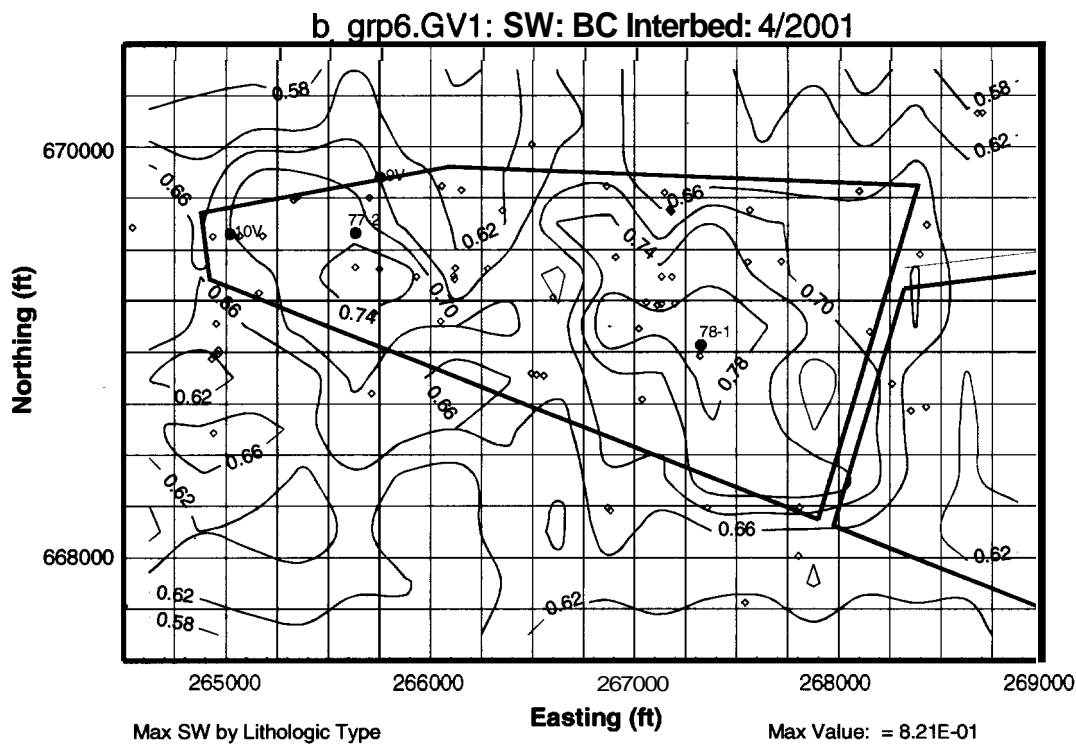
Figure 5-32. The upper plot shows the maximum simulated water saturation in the B-C interbed in calendar year 2001 and the lower plot shows the maximum simulated water saturation in the C-D interbed in calendar year 2001.

5.2.4.4 Vadose Zone *Transport* Model. This section describes development and implementation of the transport model for the vadose zone. Overall, there were very few changes in this portion of the ABRA model from that implemented in the IRA model.

5.2.4.4.1 Interface from Source Release Model into Vadose Zone *Model*—Similar to the IRA model, the vadose zone model implements the temporal source term release (described above) spatially. In addition, the release is distributed vertically at each assigned location based on the number of grid blocks within the surficial sediments. Once released, the contaminants are allowed to migrate with the simulated water movement.

5.2.4.4.2 *Partition Coefficient*—Sorption was considered to follow linear, reversible isotherms that could be described by use of K_ds, also known as distribution coefficients. A K_d lumps all possible geochemical interactions into a single parameter. Since sorption was assumed to not occur within the fractured basalt portions of either the vadose zone or the aquifer, only sediment K_d values were necessary in the **ABRA** model.

Consistent with the approach recommended in Hull (2001), sediment K_ds were assigned based on best-estimated values rather than conservative screening values. The set of best-estimate K_ds developed by Dicke (1997) was once again the primary source used in this application. Dicke (1997) placed primary reliance on site-specific measured K_ds as opposed to using literature values. Values measured on sediments from the SDA were given priority as opposed to K_ds measured on sediments from elsewhere on the INEEL. This approach is consistent with the guidance contained in EPA (1999), which includes the following statement in the introduction to Volume 1:

> It is important to note that soil scientists and geochemists knowledgeable of sorption processes in natural environments have long known that generic or default partition coefficient values found in the literature can result in significant errors when used to predict the absolute impacts of contaminant migration or site-remediation options. <u>Accordingly, one of the major recommendations of this report is that for site-specific calculations, partition coefficient values measured at site-specific conditions are absolutely essential.</u>

Table 5-13 gives the K_ds used in the ABRA model. A K_d value of 0.1 mL/g was used for C-14 based on additional site-specific work (Dicke 1998). For comparison, the K_d used for C-14 in the IRA model was 5 mL/g. One additional contaminant that was not a COPC, chromium, was also simulated, and it was assigned a K_d value of 0.1 mL/g based on Dicke (1997).

Table 5-13. Best-estimate site-specific K_ds used in the baseline risk assessment model.

Contaminant of Potential Concern	K_d (mL/g)	Contaminant of Potential Concern	K_d (mL/g)	Contaminant of Potential Concern	K_d (mL/g)
Actinium	400	Niobium	500	Radium	575
Americium	450	Neptunium	8	Technetium	0
Carbon	0.1	Protactinium	8	Thorium	500
Chlorine	0	Lead	270	Uranium	6
Iodine	0.1	Plutonium	5,100	Nitrate	0

Linear isotherms were assumed for the ABRA model for all COPCs. Results determined on SDA soil (Grossman et al. 2001) clearly demonstrate that the isotherms for uranium and neptunium were nonlinear. **An** example of a laboratory result and fitted isotherms for sample 7DS00501 is provided

in Figure 5-33. The fitted nonlinear isotherm crosses the linear isotherm (K_d approach) at concentrations greater than 250 pCi/mL. It can be argued that using a linear isotherm is conservative as long as simulated concentrations are less than this crossover point. For example, at a concentration of 100 pCi/mL, the adsorbed concentration for the linear case is ~10,000 pCi/g, while concentrations for nonlinear cases are ~17,000 pCi/g. Nonlinear isotherms thus take more of a sorbing contaminant out of solution for concentrations less than the crossover point. Results from all the other samples that were analyzed for uranium and neptunium isotherms were similar with crossover points approximately equal to 250 pCi/mL.

Maximum simulated concentrations in this modeling effort logically occurred in the most refined simulation domain closest to the source. For Np-237 and U-238, these concentrations were 20 and 100 pCi/mL, respectively. These concentrations are to the left of the crossover point of the linear and nonlinear curves on Figure 5-33. Therefore, using a linear isotherm (K_d approach) is conservative in the **ABRA** model. For completeness, from the Section 4 discussion, the maximum observed uranium isotope concentrations are on the order of 0.08 pCi/mL, which is also well within the portion of the isotherm where using a linear isotherm is conservative compared to nonlinear isotherms. Neptunium-237 has not been detected in subsurface sampling.

Cumulative frequency distribution of site-specific measured K_ds for uranium and neptunium is shown in Figures 5-34 and 5-35, respectively. These two distributions are based on the K_ds in Table 3-22. The best estimated K_d values from Dicke (1997) of 6 and 8 mL/g for uranium and neptunium (see Table 5-13), respectively, were used in the **ABRA.** These values are within the distributions, thus validating their representativeness when compared to site-specific measurements. Because they are at the low end of the site-specific measured values, they also are demonstrably conservative with respect to maximizing the likelihood of contaminant migration predicted with the **ABRA** model.
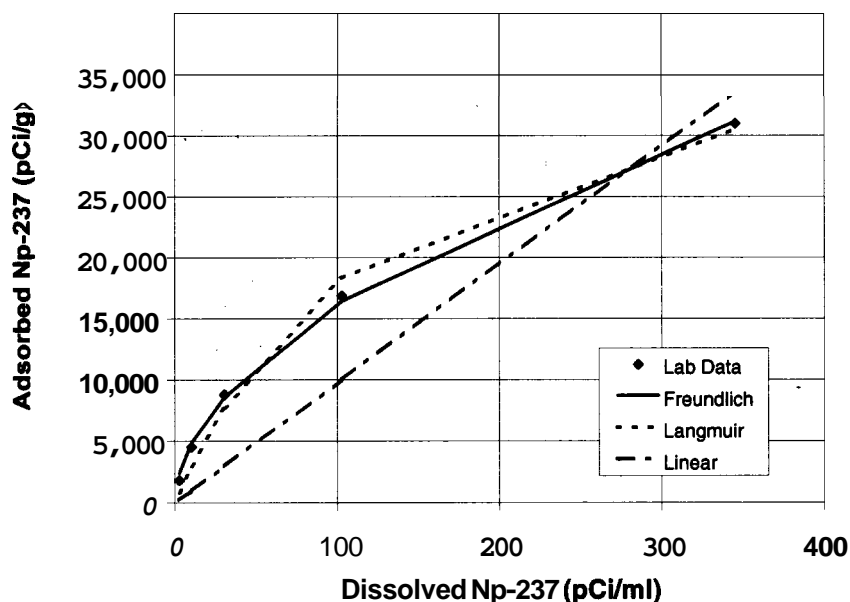

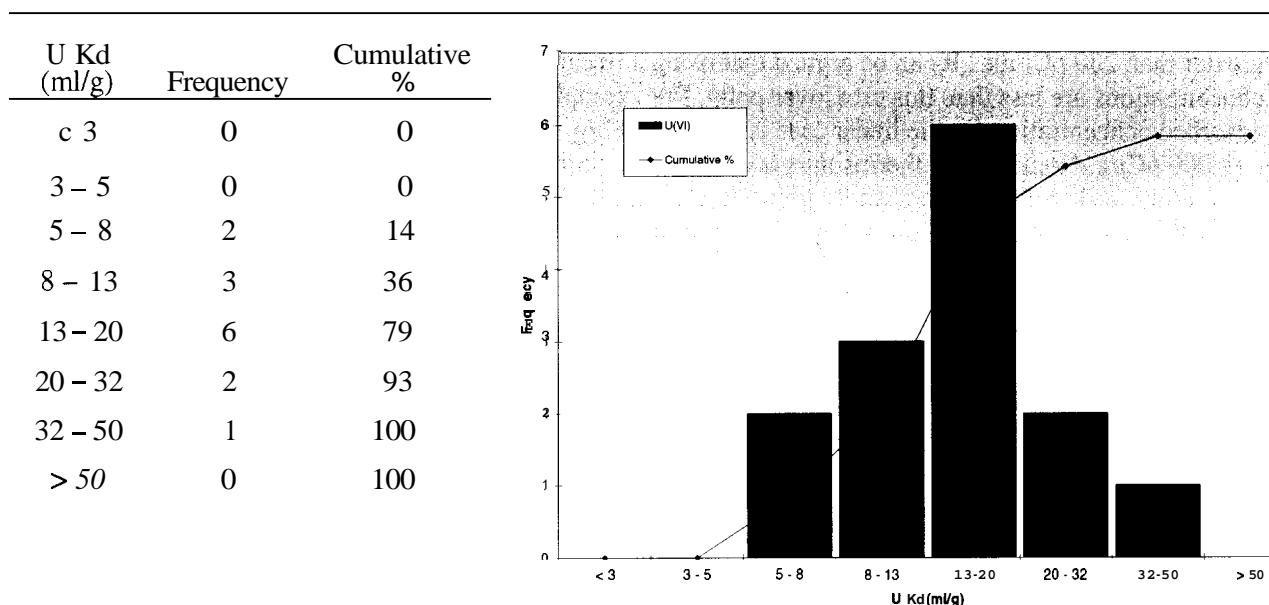Figure 5-33. Fitted linear and nonlinear isotherms for neptunium for sample 7DS00501.

U Kd (ml/g)	Frequency	Cumulative %
c 3	0	0
3 – 5	0	0
5 – 8	2	14
8 – 13	3	36
13 – 20	6	79
20 – 32	2	93
32 – 50	1	100
> 50	0	100

Figure 5-34. Cumulative frequency distribution of uranium K_d values measured on Subsurface Disposal Area sedimentary interbed samples.

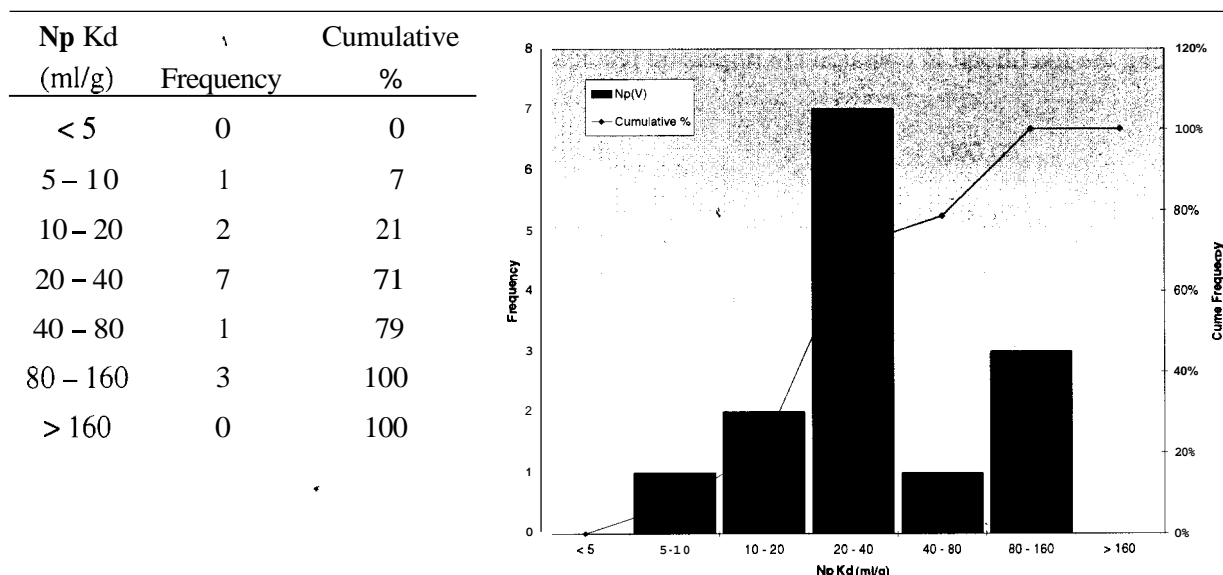| Np Kd (ml/g)	Frequency	Cumulative %
< 5	0	0
5 – 10	1	7
10 – 20	2	21
20 – 40	7	71
40 – 80	1	79
80 – 160	3	100
> 160	0	100

Figure 5-35. Cumulative frequency distribution of neptunium K_d values measured on Subsurface Disposal Area sedimentary interbed samples.

Plutonium behavior in the subsurface at the SDA has continued to receive scrutiny since vadose zone investigations started in the early 1970s. For the base case estimates in the ABRA, the plutonium K_d of 5,100 mL/g is assigned based on the best-available, site-specific data. The assigned value **is** from the low end of the measured K_d values for plutonium(IV), which is the predominant state (Hull 2001). Figure 5-36 shows the cumulative frequency distribution for measured plutonium K_d values, including both plutonium(IV) and plutonium(VI). The topic of facilitated transport of plutonium is addressed below.

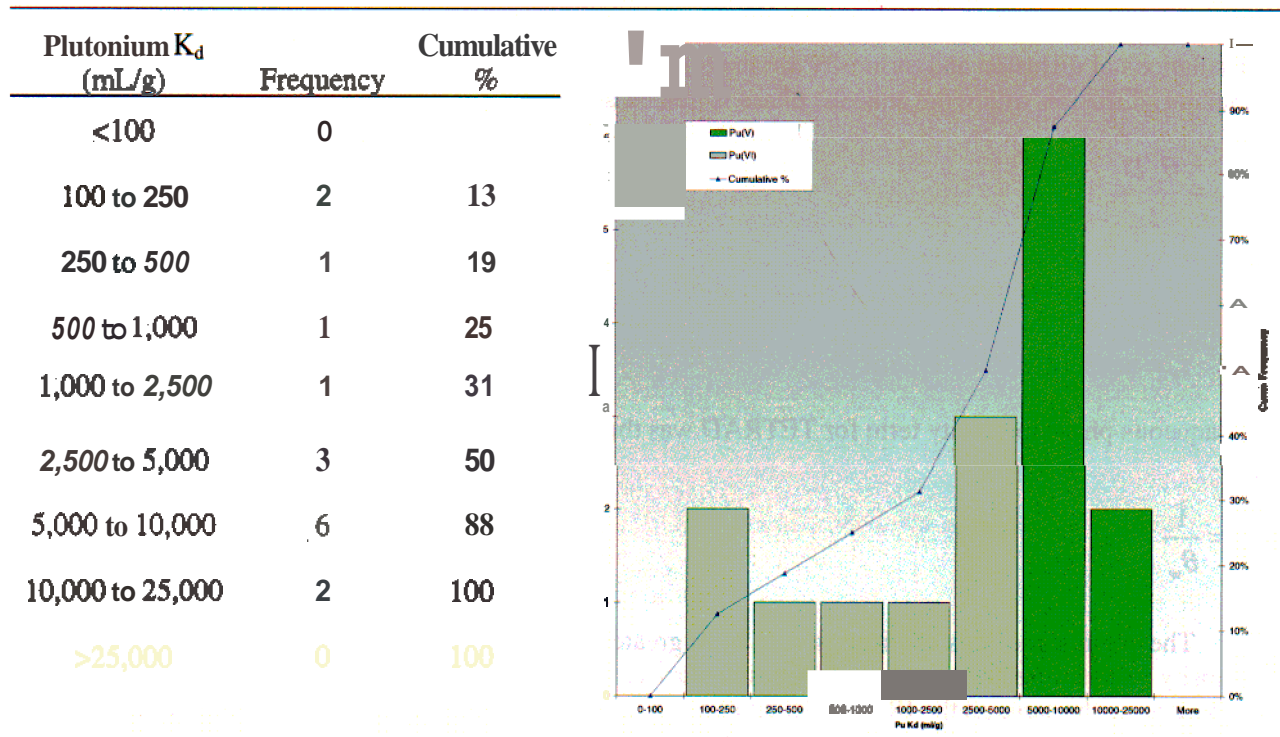| Plutonium K_d (mL/g)	Frequency	Cumulative %
<100	0	
100 to 250	2	13
250 to 500	1	19
500 to 1,000	1	25
1,000 to 2,500	1	31
2,500 to 5,000	3	50
5,000 to 10,000	6	88
10,000 to 25,000	2	100
>25,000	0	100

Figure 5-36. Cumulative frequency distribution of plutonium K_d values measured on Idaho National Engineering and Environmental Laboratory soil and sedimentary interbed materials by Newman and Dunnivant (1995).

5.2.4.4.3 Other Transport Parameters—A variety of additional parameters were required in order to implement the vadose zone transport model. These were the particle density, diffusion coefficients, tortuosity, and half-lives. The particle density was assigned the typical value for sediments of 2,700 kg/m^3 (Freeze and Cherry 1979). This was the same value that was assigned in the IRA model. Since sorption was assumed not to occur in the fractured basalt, the grain density assigned for that portion of the simulation domain did not matter.

Diffusion of contaminants within the aqueous phase was assigned the common literature value of 1×10^{-5} cm^2/s (Freeze and Cherry 1979). This was the same value *that* was assigned in the IRA model. The restriction of diffusion caused by tortuosity also was included based on a relationship from Lerman (1988) used to describe diffusion as follows:

$$D = D_o \theta_w^2 . \tag{5-1}$$

where

D = diffusion in the porous medium (length^2/time)

D_o = free-water diffusion coefficient (length^2/time)

θ_w = volumetric moisture content (unitless).

In any numerical simulation exercise, correct implementation of diffusion is important. Various formulations of diffusion and tortuosity are implemented in different simulators. In the TETRAD simulator, diffusion within the aqueous phase is treated as

$$D_{eff} = \frac{\theta_w D_o}{\tau_w}$$

(5-2)

where D_{eff} = effective diffusion coefficient (length^2/time)

τ_w = aqueous-phase tortuosity.

The aqueous-phase tortuosity term for TETRAD was then calculated as

$$\tau_w = \frac{1}{e_,}$$.

(5-3)

The end result of this application is to have greater tortuosities assigned for drier conditions. Single tortuosity values were assigned for each sedimentary feature and for the fractured basalt; the values assigned were the same as the IRA model and are given in Table **5-14.** The fractured basalt has a very low simulated moisture content, less than **0.01,** and therefore was assigned the highest aqueous-phase tortuosity.

Table **5-14.** Aqueous-phase tortuosities for the baseline risk assessment model.

Material	TETRAD Tortuosity (Dimensionless)
Surficial sediments	**3.4**
A-B interbed	**5.3**
B-C interbed	**3.8**
C-D interbed	**2.1**
Fractured basalt	**133**

Longitudinal and transverse dispersivities of 5.0 and 0.5 m, respectively, were assigned in the vadose zone transport model. The longitudinal value is the same as the IRA model and was originally based on inverse modeling from the Large-Scale Infiltration Test (Magnuson **1995).** The IRA model used a value of 0.0 m for the transverse dispersion in the vadose zone. The ABRA model assigned the value 0.5 m by using the modeling rule-of-thumb that the transverse dispersion is one-tenth of the longitudinal dispersion (Freeze and Cherry **1979).** The 5.0 m longitudinal value is smaller than would be assigned using the general rule of thumb that the dispersivity should be approximately 1/10th of the domain size (Gelhar **1986).** In the absence of calibration data, such as the breakthrough of a nonsorbing contaminant, there is no basis to substantially adjust the dispersivities from those used in the IRA model. Ideally, higher concentrations would result for pulses of mobile contaminants because the simulated front would remain sharper because of the lower dispersivity. For a long slow release, such as a solubility-limited release of a lower-mobility contaminant, the lower dispersivity would ideally result in slightly later first-arrival. However, because dispersion control was not used in the TETRAD simulation, the relative contribution of numerical dispersion compared to simulated dispersion is unknown.

Half-lives for each radioactive COPC were assigned based on literature values (GE **1989)** and were the same as those used in the IRA model.

5.2.4.4.4   Interface from Vadose Zone Model into Aquifer Model—Because of the separation of the vadose zone and aquifer domains, it was necessary to take the mass of water and contaminants emanating from the vadose zone simulation domain and transfer them into the top of the aquifer simulation domain as a boundary condition. This was done on a grid-block-by-grid-block basis; therefore, no spatial averaging was necessary. Refinement was used in the aquifer domain to establish a one-to-one correspondence between grid blocks in each domain. The complete time-history of the flux of water and contaminants from the vadose zone model was transferred into the aquifer model.

5.2.4.5   Aquifer Flow Model. Water levels and flow directions for aquifer simulations were recalibrated with additional data collected after the development of the IRA model. Complete details of aquifer model development and calibration are contained in Whitmire **(2001).**

Calibration of the aquifer model was necessary to take advantage of additional water level data from aquifer monitoring wells that were not present for the calibration of the IRA model. The additional seven aquifer wells were M11S, **M12S, M13S, M14S, M15S, M16S,** and **M17S.** Deviation-corrected water level data from the March and April measurements and the October and November measurements in **2000** were used. Figure **5-37** is the water table map that was developed using data collected in March and April of **2000.** Superimposed on the figure is the base aquifer simulation domain, which used grid blocks **305** m **(1,000** ft) on a side. Open circles indicate locations where data were used in creating the water table map. Prescribed boundary conditions for the aquifer simulation were interpolated onto the outer edge of each external grid block based on this water table map. Figure **5-38** illustrates just the aquifer simulation domain with the one level of refinement that was used to match the vadose zone model in the vicinity of the SDA.

The thickness of the aquifer model was kept the same as in the IRA model, namely **76** m **(250** ft). This thickness was again discretized using seven vertical grid blocks varying in size from 8 m **(26** ft) at the top to 18 m **(59** ft) at the bottom. The **76** m **(250** ft) thickness originated from generalizations of Robertson, Schoen, and Barraclough **(1974)** on the depth to which contaminants were detected in plumes in the southern part of the INEEL. This aquifer thickness was first implemented in simulations by Robertson **(1974).** Recent estimates of effective aquifer thickness show that it varies across the INEEL and is approximately **150** m **(490** ft) in Well C1A, immediately northeast of the SDA (Arnett and Smith **2001).** The effect **of** retaining the thinner aquifer in the ABRA simulations is conservative in that there is less aquifer thickness is available for contaminant dispersion. Thus, the resulting estimates of contaminant concentrations are higher than for a larger effective aquifer thickness.
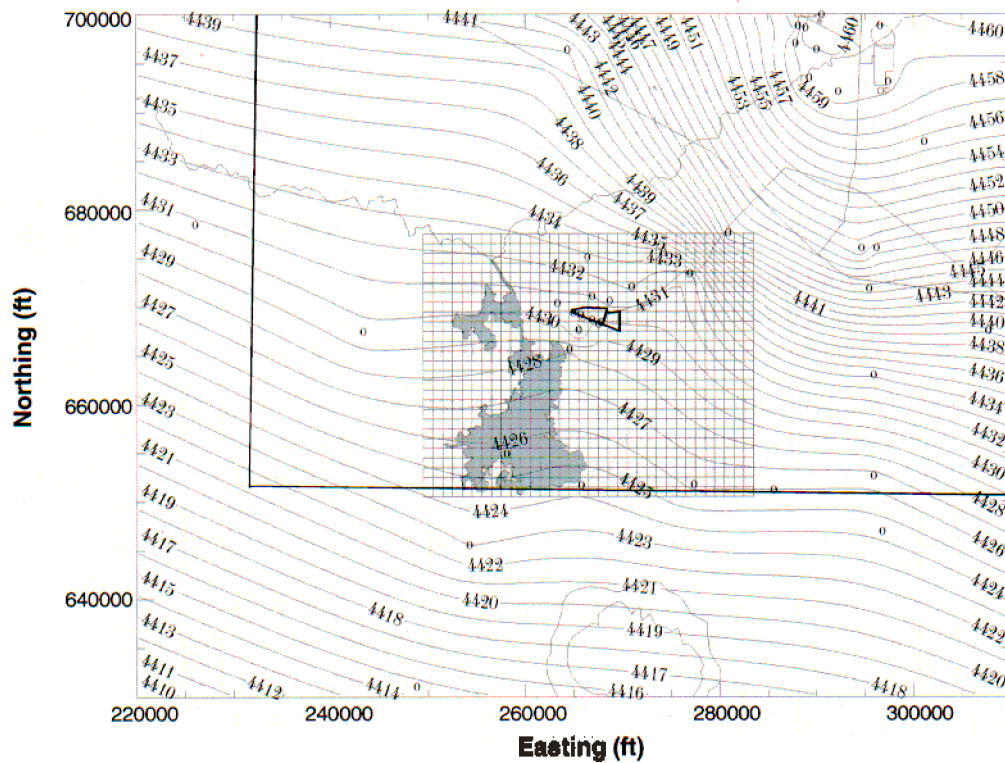
Figure 5-37. Water table *map* generated with deviation-corrected data from March and April 2000. *Also* shown is the base aquifer simulation domain.
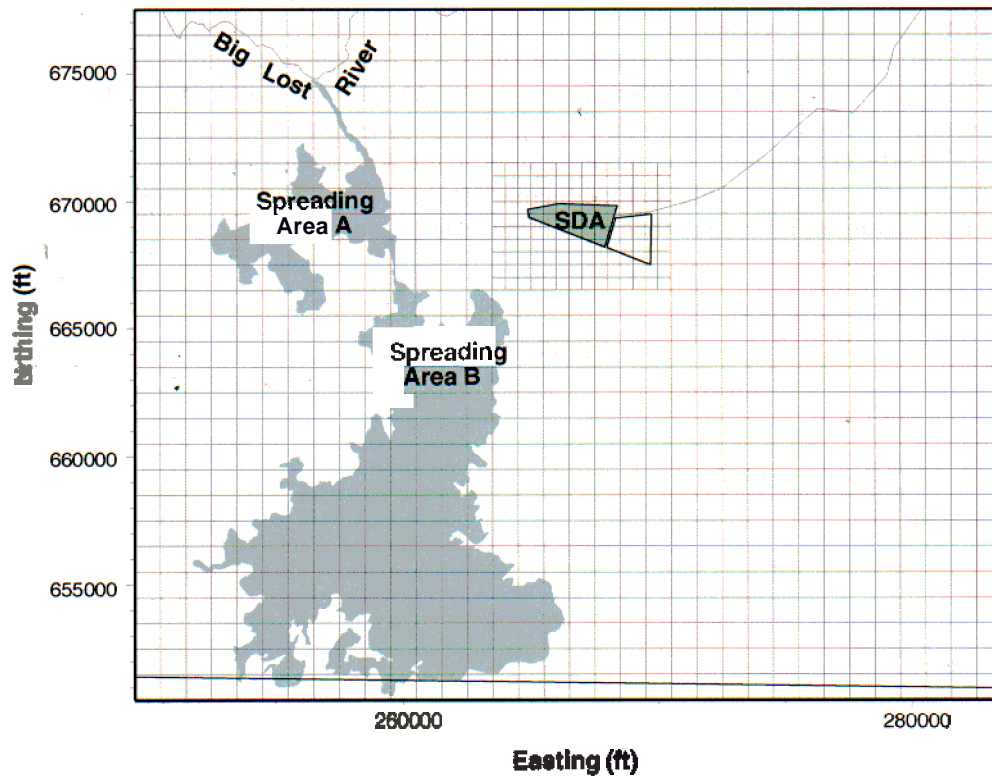

Figure 5-38. Aquifer simulation domain with one level of refinement to match vadose zone model.

Simulated hydraulic heads were compared with values measured from wells across the southern portion of the INEEL. The final optimized simulation results are shown in Figure 5-39 for the base and refined simulation domains. The small localized mound in the refined area is a result of additional water flux being applied inside the refined area from the vadose zone simulation. These heads were optimized through manual trial-and-error by trying different permeability distributions across the aquifer simulation domain. It is recognized that this does not result in a unique solution. The root mean squared error of the residuals, or difference between observed and simulated water levels, was used to judge between results of different attempts to simulate water levels in the aquifer. The value was calculated using

$$RMS = \sqrt{\frac{\sum_{i=1}^{n} (\text{Residuals})_i^2}{n}}$$

(5-4)

where

$RMS =$

Residuals

n = number of locations at which observed water level measurements were available.

The root mean squared error for the optimal fit shown in Figure 5-39 was RMS=0.899 ft. The optimal set of aquifer permeabilities that minimized the root-mean-squared-error differences between measured and simulated water levels is shown in Figure 5-40. The measured water level at Well M13S (close to the EBR-1 facility) exerted the greatest impact in terms of changing the simulated water levels from the IRA model. This optimized set of aquifer permeabilities was used in predictive modeling for the ABRA. The final optimized aquifer permeability set was a combination of the permeabilities and distribution used in the IRA model and the permeabilities and distribution from the WAG 10 model (McCarthy et al. 1995). A difference from the IRA model was that no vertical variation in aquifer permeability was included.

Resulting relative average linear groundwater velocities (also known as seepage or pore velocities) in the uppermost layer are shown in a vector plot in Figure 5-41 for the base and refined domain. Results for successively deeper model layers are essentially identical, given no vertical permeability contrasts in the model. The size of the vectors from each grid point is drawn on a scale relative to the maximum velocity in the model. The bottom plot in the figure is for the refined grid and has velocities in meters per year overlaid at each grid block. The dominant influence of the low-permeability zone to the south and southwest of the SDA can be seen in the results, especially in the refined grid. Water movement is effectively blocked by the low-permeability region and has to diverge around the low-permeability zone. This divergence results in simulated westward velocities just to the northwest of the SDA and simulated southeastward velocities beneath the eastern half of the SDA.

As part of this aquifer calibration effort, kriged permeability distributions based on single-well pump-test results were tested. Kriged aquifer permeability distributions were taken from Leecaster (2002). However, short spatial correlation range and limited data points restricted the accuracy of the kriged aquifer permeabilities and did not result in an accurate prediction of water levels. These results are not shown in this section but are contained in Whitmire (2001).

Possible influences on aquifer velocities from Big Lost River water discharged to the spreading areas were also investigated. Two methods were used to apply additional water in the aquifer simulation and are shown in Figure 5-42. The period from December 1982 through June 1985 was selected for
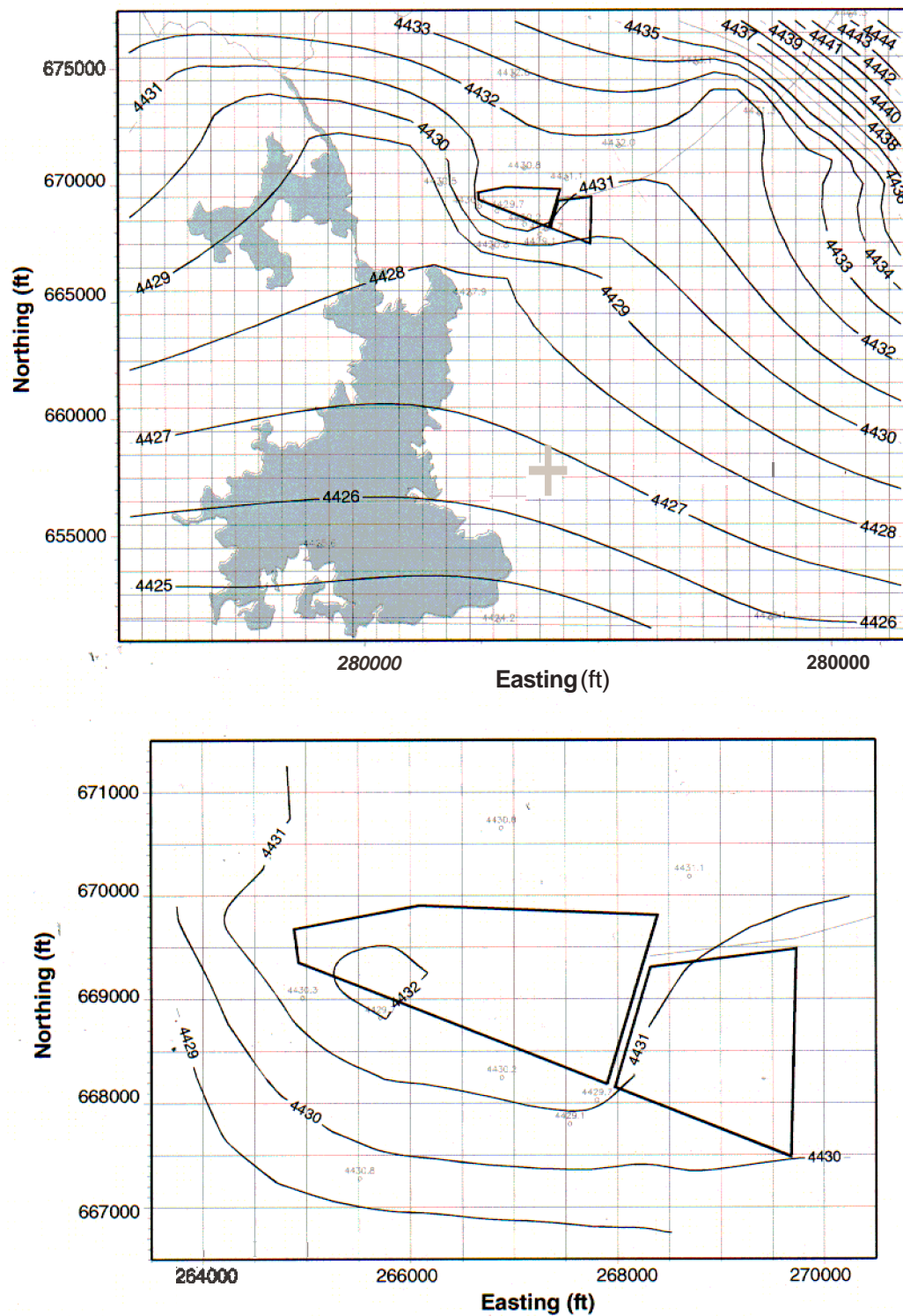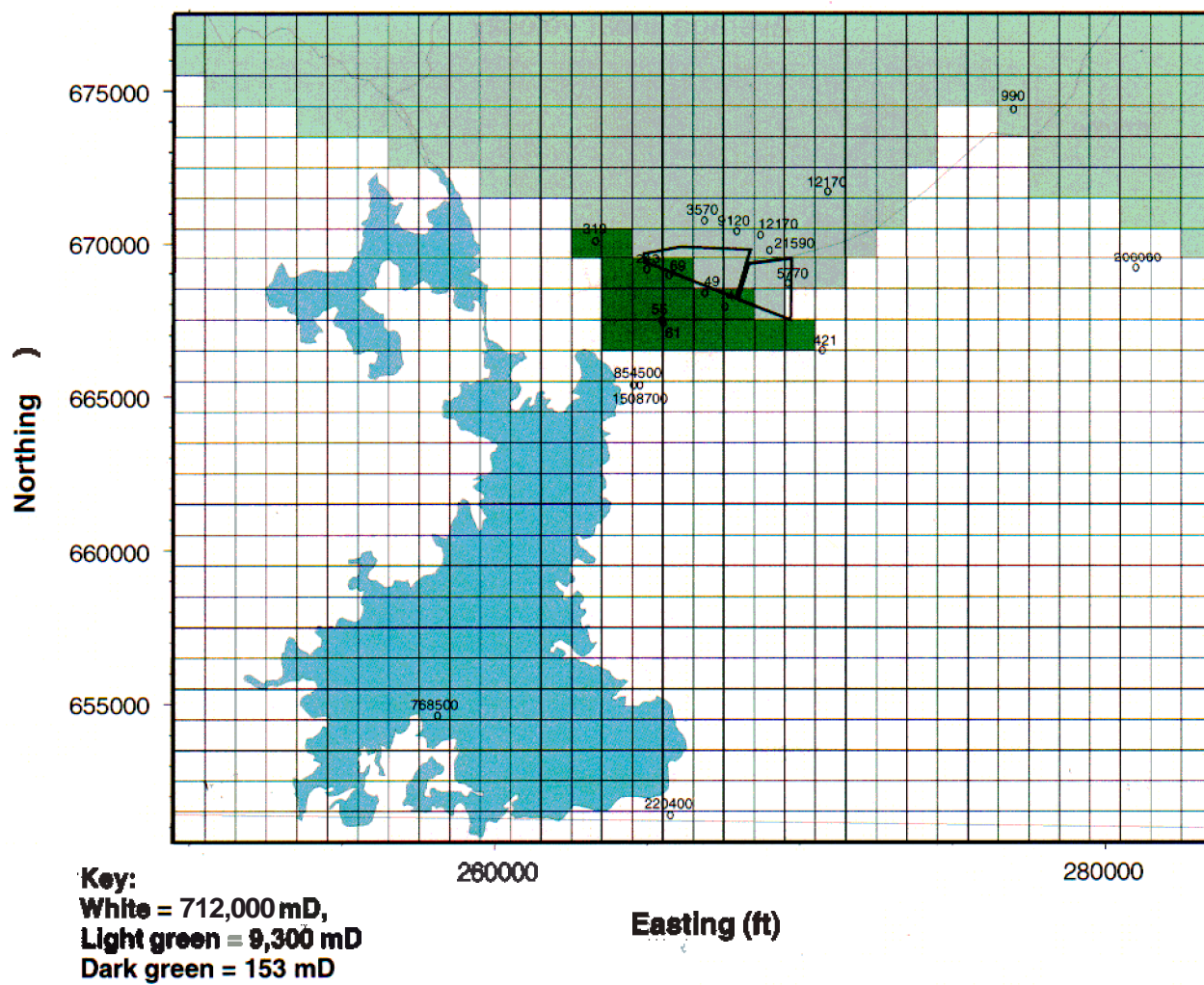
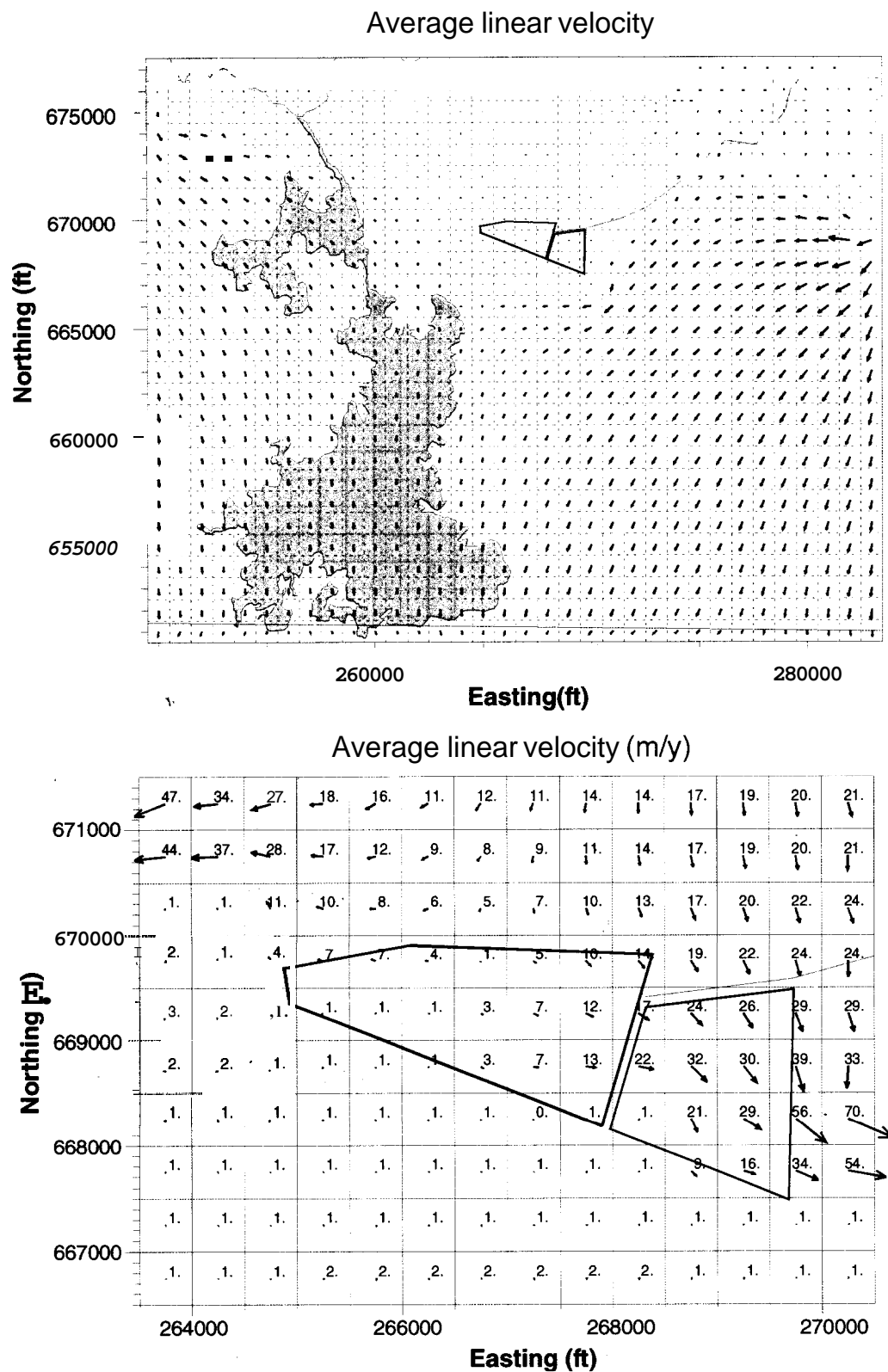Figure 5-39. Best-fitted simulated water levels for base and refined grid.

Figure 5-40. **Final aquifer permeability set used for the baseline risk assessment model.**

Average linear velocity

Average linear velocity (m/y)

Figure 5-41. Simulated groundwater average linear velocities (m/year) for the base and refined simulation domains.

Key:
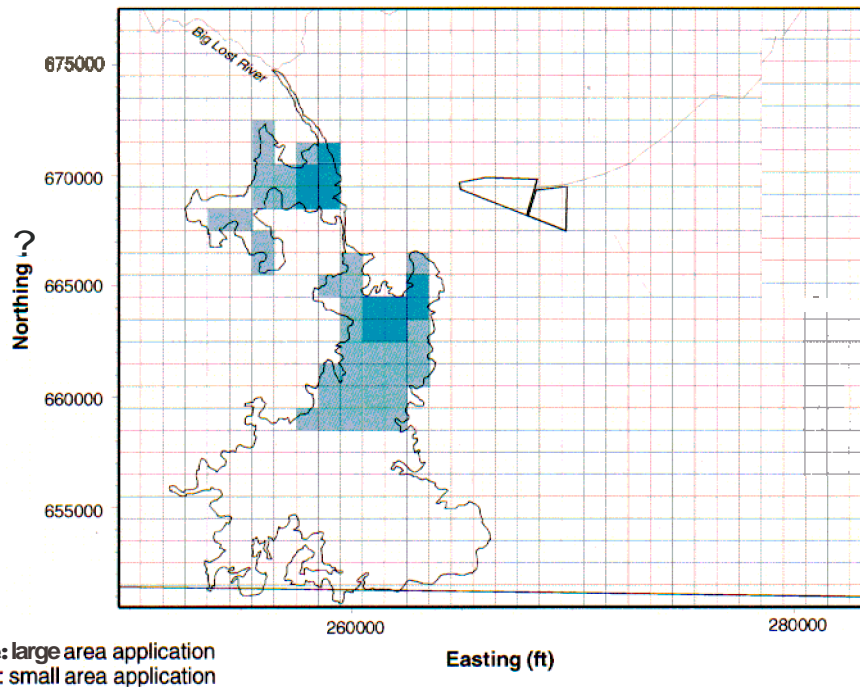Light blue: large area application
Dark blue: small area application

Figure 5-42. Large and small area application regions for spreading area water into the aquifer simulation domain.

simulation because water was diverted continuously to the spreading areas during this period. Average amounts of water discharged to both Spreading Areas A and B were determined based on the gauging results (see Figure 5-29) which show an overall approximate diversion from the river of 16,300 acre-ft/month during this period. In one scenario, this average discharge to the spreading areas was applied over 47 grid blocks to emulate the effect of the entire area of Spreading Areas A and B being filled. This was termed the "large area application." In the second method, the same amount of water was applied over just 11 grid blocks and was termed the "small area application." These water fluxes are applied directly to the top of the aquifer model as if the water transit through the vadose zone was instantaneous and no water was lost either to storage within the vadose zone or to evaporation. Though the modeling for these spreading area simulations was originally performed in Whitmire (2001), the spreading area impact results presented in this section are somewhat different because an implementation error was discovered that resulted in significantly less water being applied than was intended. In this section, the intended fluxes shown in Table 5-15 are applied continuously throughout the period in a step-wise fashion.

Table 5-15. Water fluxes (m/day) applied in spreading area simulations.

Water Flux	Spreading Area A	Spreading Area B
Large area application	*0.29*	0.97
Small area application	0.091	0.19

Simulated water levels for November 1984, near the end of the application of the spreading-area water, are shown for both cases in Figures 5-43 and 5-44. The same March 2000 water level measurements are still included on these figures for reference. In each case a substantial groundwater mound results. The simulated rise in water levels is partly substantiated by the water level measurements from that period (Wood 1989). Table 5-16 shows measured water level rises in four SDA-vicinity wells

5-81

during the period **1982** to **1985** based on the hydrographs presented in Wood **(1989).** The simulated mound is in part limited by the first-type boundaries prescribed at the perimeter of the model. Ideally, the boundary conditions should not impact this simulation and partially limit the results. Well 88 is included in the table, though its rise is considered abnormal (Wood **1989).**

Table **5-16.** Measured and simulated rises in water level for wells in the vicinity of the Radioactive Waste Management Complex during **1982** to **1985** spreading area diversions.

Well	Measured Gross Water Level Rise (ft)	Ancillary Basis for Risk Analysis Model Water Level (ft)	Large Area Application Water Level (ft)	Large Area Application Water Level Rise (ft)	Small Area Application Water Level (ft)	Small Area Application Rise in Water Level Rise (ft)
USGS-87	11	4,431.5	4,436	4.5	4,437.5	6
USGS-89	20	4,429	4,440	11	4,444	15
USGS-90	12	4,430.5	4,434.5	4	4,435.5	5
USGS-88	80	4,429.5	4,439.5	10	4,443	13.5

Rises in the simulated water level, based on comparing the large and small spreading area application simulations to the ABRA model, are shown in Table **5-16** for comparison to the measured rise in water level. Though the simulated rises are less than the observed rises, they show similar characteristics. Simulation could possibly be improved by (a) more closely matching actual discharges to the spreading areas instead of using an averaged step-function, and by (b) either moving simulation boundaries farther away so they do not impact the results or by modifying boundaries temporally to reflect regional changes in water levels.

The resulting velocity distribution in the refined portion of the aquifer grid for these two spreading area impact simulations is shown in Figure **5-45.** Comparing velocities shown previously in Figure **5-41** for the ABRA aquifer simulation shows the increase in the magnitudes of groundwater flow velocity beneath the eastern portion of the SDA when additional water was input into the aquifer at the spreading areas; however, directions shift only slightly and still generally trend southeast. As expected, flow velocity magnitudes increase more when input from the spreading areas is concentrated into a smaller region. In both cases, westward velocities are reversed northwest of the SDA.

In summary, relative to the aquifer flow model calibration, the flatness of the water table coupled with an apparent low permeability region to the south-southwest of the SDA precludes accurate determination of groundwater flow directions. The IRA hypothesis that the flow velocities immediately under the SDA are slow is consistent with new evidence. Before the IRA model, water velocity beneath the SDA was treated as if it were the same as the regional aquifer, with average linear velocities of **0.15** to **4.6** m/day **(0.5** to **15** ft/day) (Maheras et al. **1994).** The ongoing tracer test in Well M17S immediately beneath the SDA has been showing a very slow dilution of tracers introduced directly into the well, indicating slow water movement within the aquifer at that location (see Section 2.3.3). This hypothesis is also consistent with the interpretation by Roback et al. **(2001)** that the RWMC is in a low-permeability region extending southerly from the Lost River Range onto the INEEL. Additional water levels collected during the ongoing WAG 7 quarterly monitoring program will be a key part of conclusively determining the direction and timing of aquifer flow velocities in the SDA region. The use of isobaric techniques may be beneficial in making more accurate quarterly water level measurements in a manner uninfluenced by atmospheric pressure fluctuations.

PW at 12000.0 days, in layer 1, depth = 4.0 meters

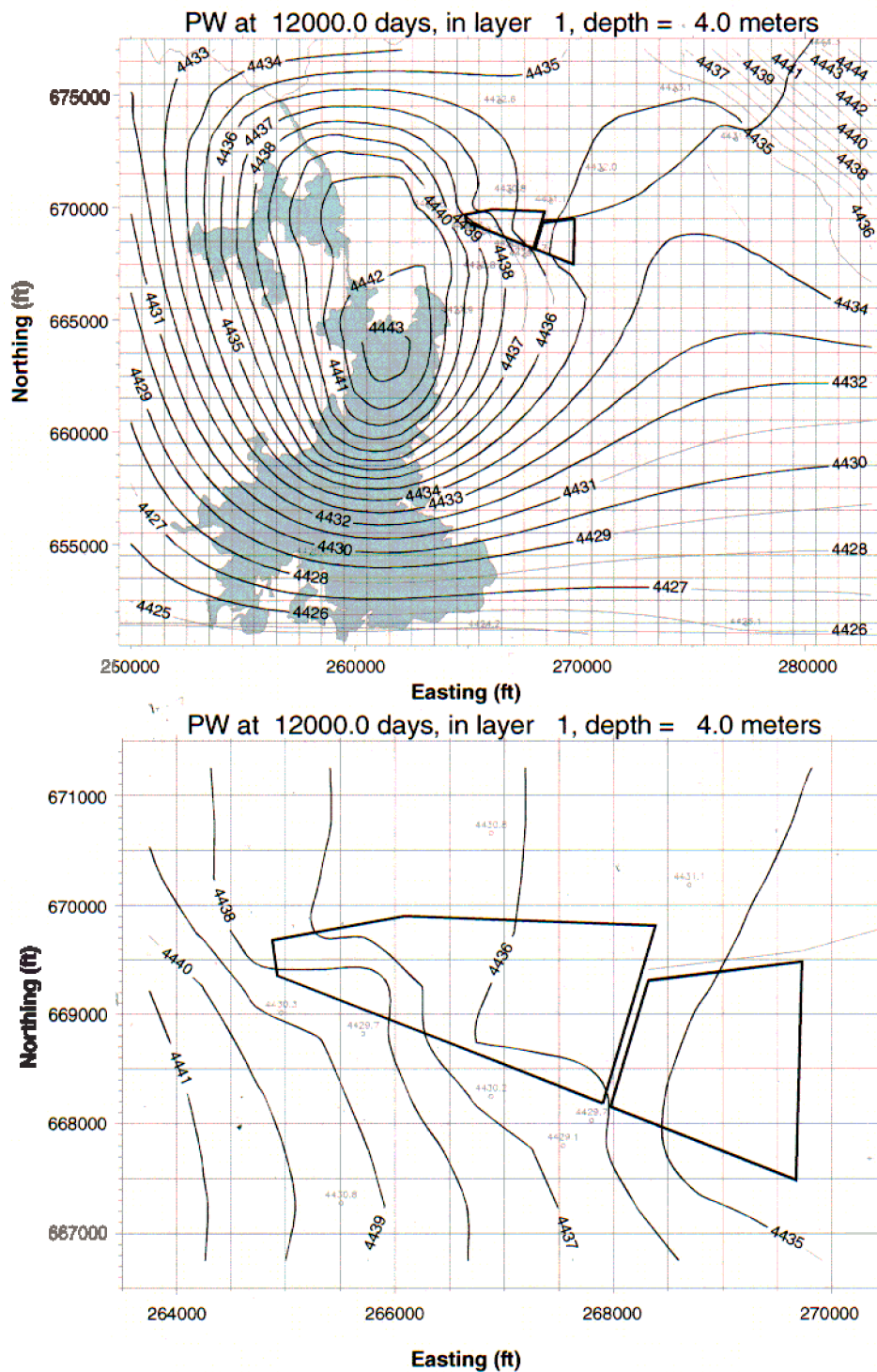PW at 12000.0 days, in layer 1, depth = 4.0 meters

Figure 5-43. Simulated water levels for the base and refined aquifer domain for the large area application of spreading-area water.
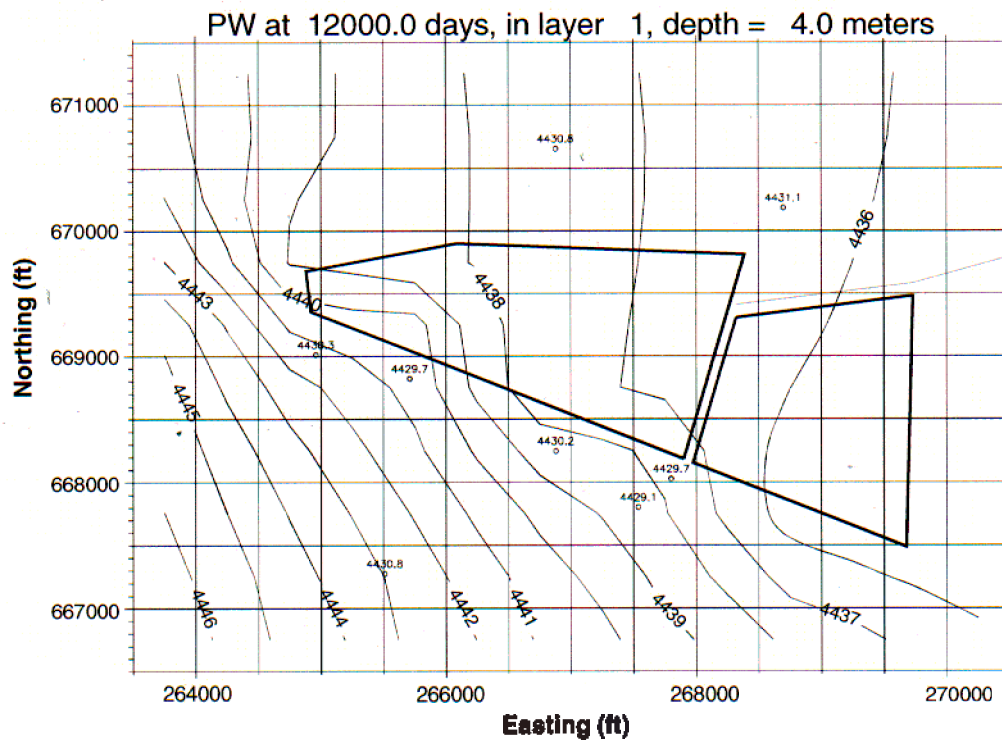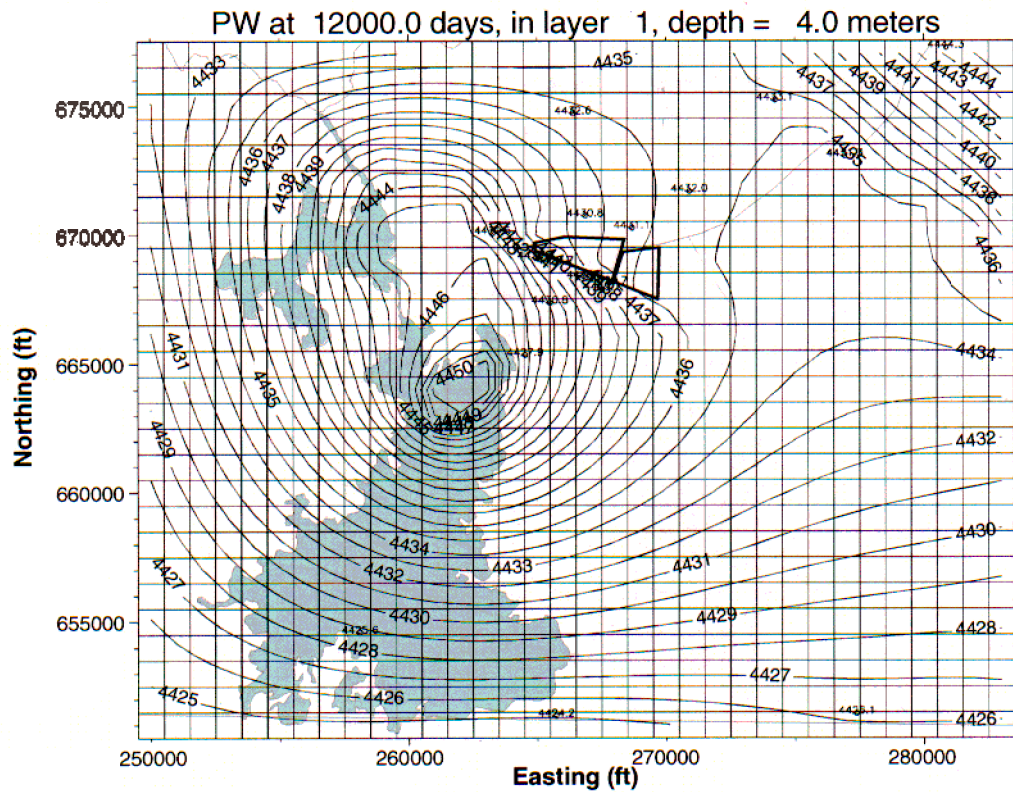
Figure 5-44. Simulated water levels for the base and refined aquifer domain for the small area application of spreading-area water.
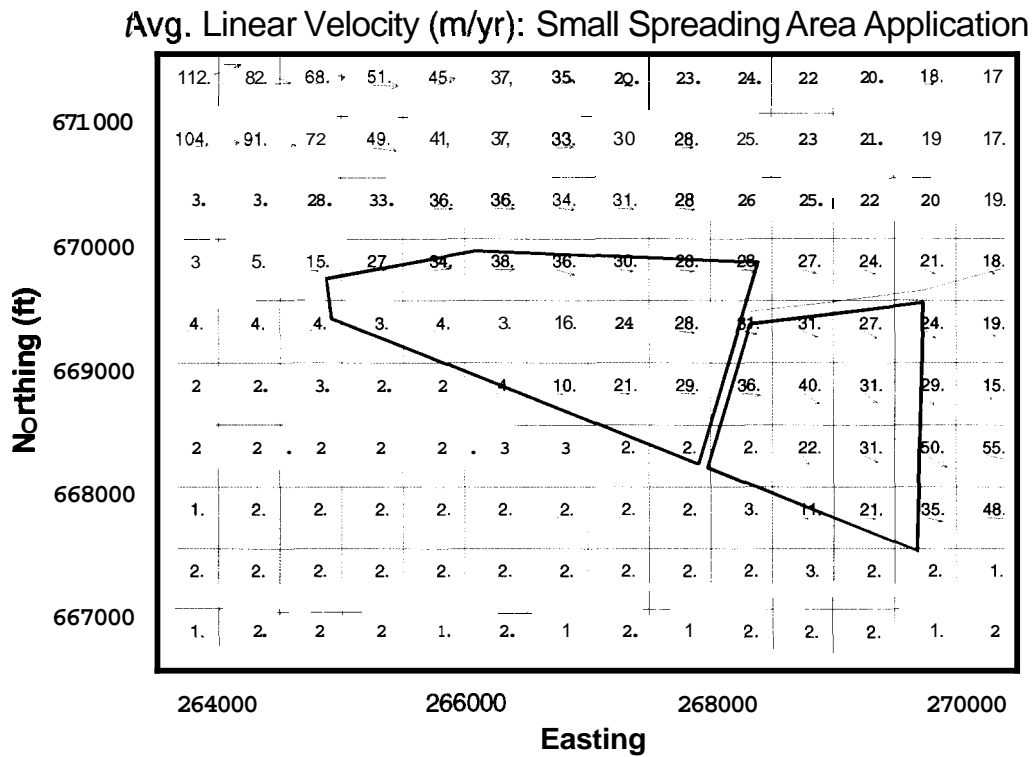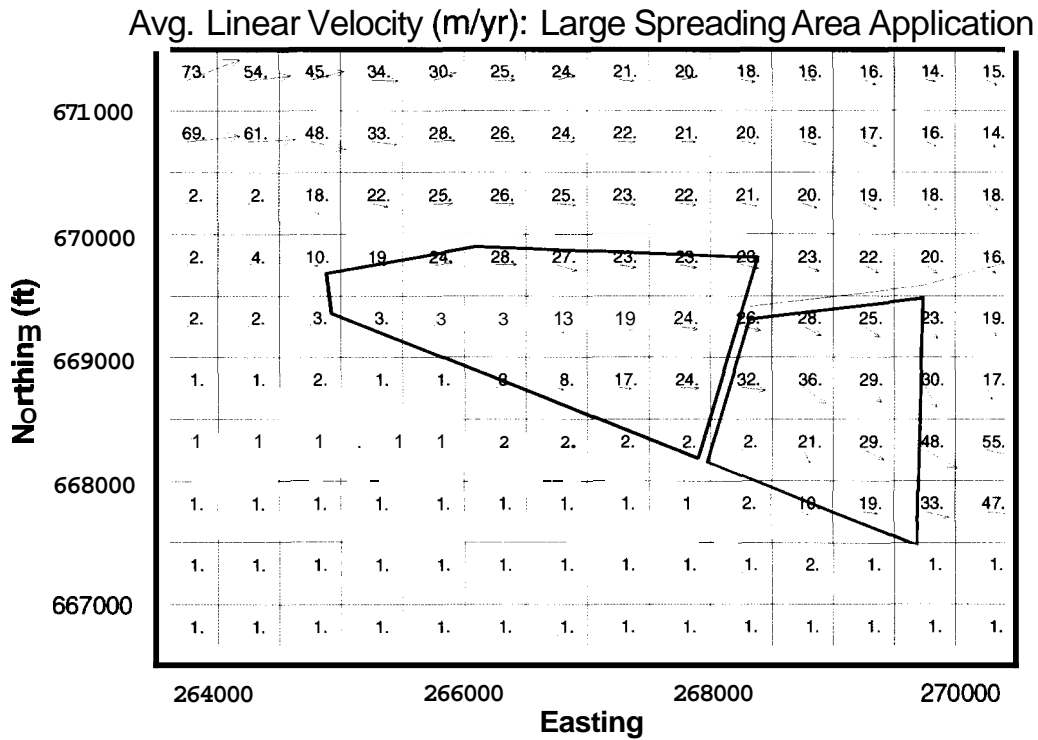
Avg. Linear Velocity (m/yr): Large Spreading Area Application

Avg. Linear Velocity (m/yr): Small Spreading Area Application

Figure 5-45. Simulated groundwater average linear velocities (m/year) in the refined simulation domain with additional water applied at the spreading areas.

5.2.4.6 Aquifer Transport Model. Simulating transport in the aquifer model was straightforward compared to the vadose zone. The flux of water and contaminants from the vadose zone model was applied as an upper boundary condition in the refined portion of the model. The remainder of the upper surface of the model was treated as a no-flux area, as was the bottom surface of the model. Contaminants could advect out external boundaries.

Because it was assumed that sorption did not occur within the fractured basalts, and only fractured basalts were simulated in the aquifer portion of the model, no K_d values were necessary in the aquifer portion of the model. Diffusion was included and was parameterized the same as in the vadose zone model. Tortuosity was assigned using the same approach as in the vadose zone model (i.e., following the approach in Lerman [1988]). Dispersion was parameterized differently in the aquifer model than in the vadose zone model. Longitudinal and transverse dispersivities of 9 and **4** m (30 and 13 ft) were assigned, respectively. These values were the same as those used in the IRA model. Similar to the vadose zone model, assigned dispersivities are small relative to the 1/10th domain size general rule of thumb. However, because dispersion control was not used in the TETRAD simulation, the relative contribution of numerical dispersion compared to simulated dispersion is unknown.

In the remainder of this section are comparisons of simulated and observed nitrate and chromium concentrations. These two contaminants are chosen for scrutiny because they offer the most insight into how the model results compare to data. Both contaminants are conservative in that they do not adsorb and, thus, avoid the complication of assigning a K_d.

5.2.4.6.1 Comparison **of** Simulated and Observed Nitrate Concentrations — This section shows comparisons of simulated results and monitoring results for nitrate as elemental nitrogen. Emphasis is on aquifer results because that is where the longest-term monitoring has occurred. Both time history and contour plots are presented to show spatial resolution. Nitrate is a ubiquitous chemical in groundwater; background concentrations must be considered even though it is assumed for the ABRA modeling that contaminant concentrations in the vicinity of the SDA are not influenced by upgradient sources. The local background concentration was previously estimated as **0.7** mg/L (Burgess 1996). For the time history plots shown in Figure 5-46, the simulation results are added to this background concentration. Time history plots are all shown with a consistent time axis and a consistent concentration axis. The value selected for the maximum on the concentration scale was the maximum observed in field monitoring data. In some cases, predicted values extend above the concentration axis.

These same 16 time histories, with an additional time history for Well 120, are shown again in Figure **5-47** superimposed onto a plan-view map showing their locations with respect to the SDA. As can be seen in the figure, nitrate is sometimes over predicted and sometimes under predicted. Ignoring for the moment the complexity of flow and transport in the vadose zone, nitrate monitoring results in Figure 5-47 highlight what is obviously a complex flow system in the aquifer. Monitoring data for nitrate are not spatially consistent. It is tempting to interpret an influence in aquifer nitrate monitoring results from the Big Lost River water that is discharged into the spreading areas. This could explain elevated concentrations of nitrate above the interpreted local background in Wells 89, M1S, and 88, which are closer to the spreading areas. Concentration of nitrate in Well M4D differs from that in Well 88 but that can be explained by the screened interval being much deeper in Well M4D and, therefore, Well M4D samples were obtained from a different portion of the aquifer. However, by this logic, Well 120 should also show elevated nitrate concentrations above the local background and it does not. Wells M10S and 119 show slightly increased concentrations of nitrate, which may be caused by migration of nitrate disposed of in the SDA. Well M17S, located directly beneath the SDA, has shown no elevated nitrate concentrations in its short monitoring history. Wells **87,** M3S, the RWMC Production Well, M7S, M16S, 90, and M15S all show nitrate concentrations consistent with the estimated local background concentration of **0.7** mg/L. Well M6S, located approximately 914 m (3,000 ft) to the southeast of the
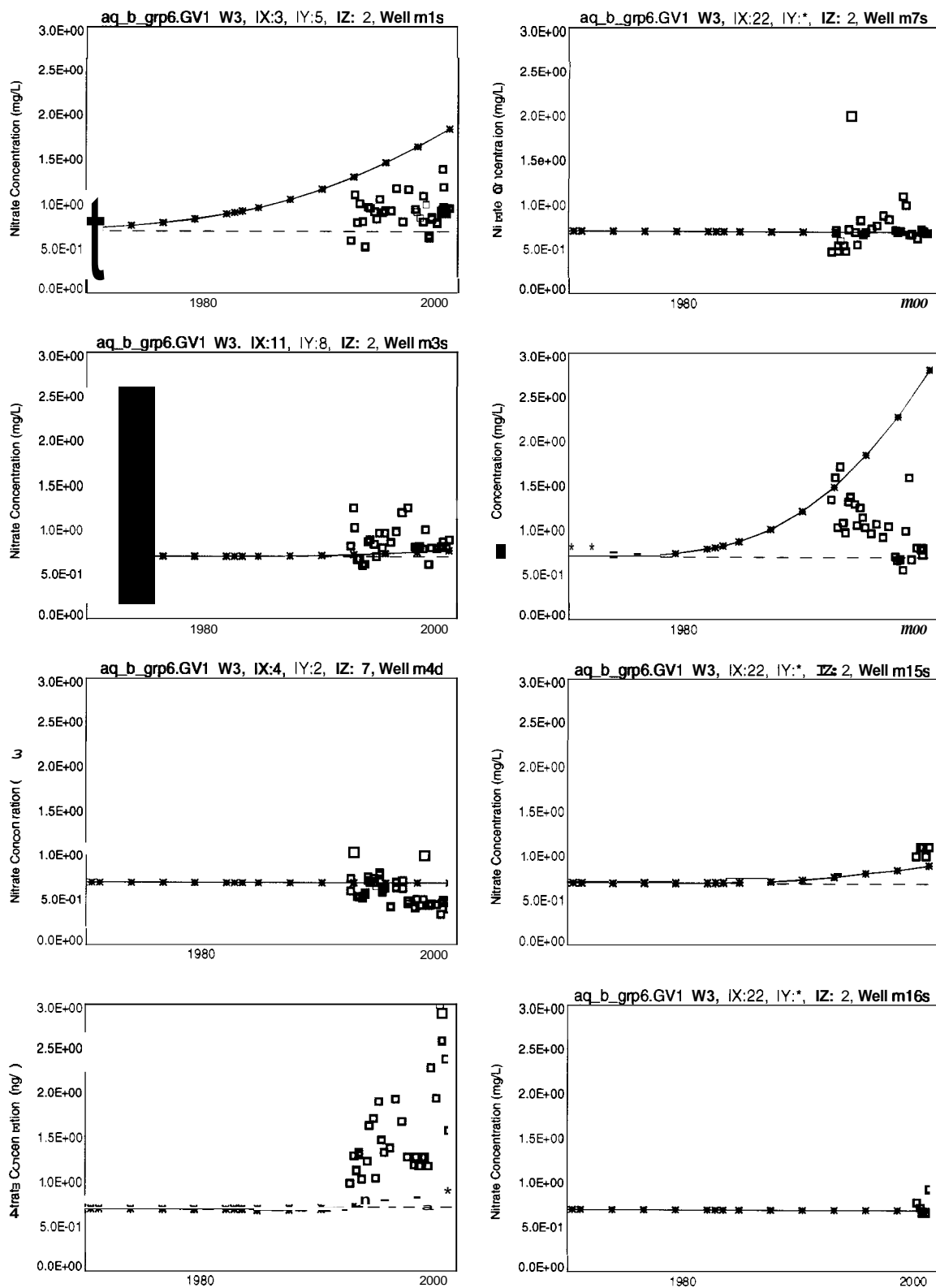
Figure 5-46. Comparison of simulated and observed nitrate (as N) concentration time histories for aquifer monitoring wells in the vicinity of the Subsurface Disposal Area.
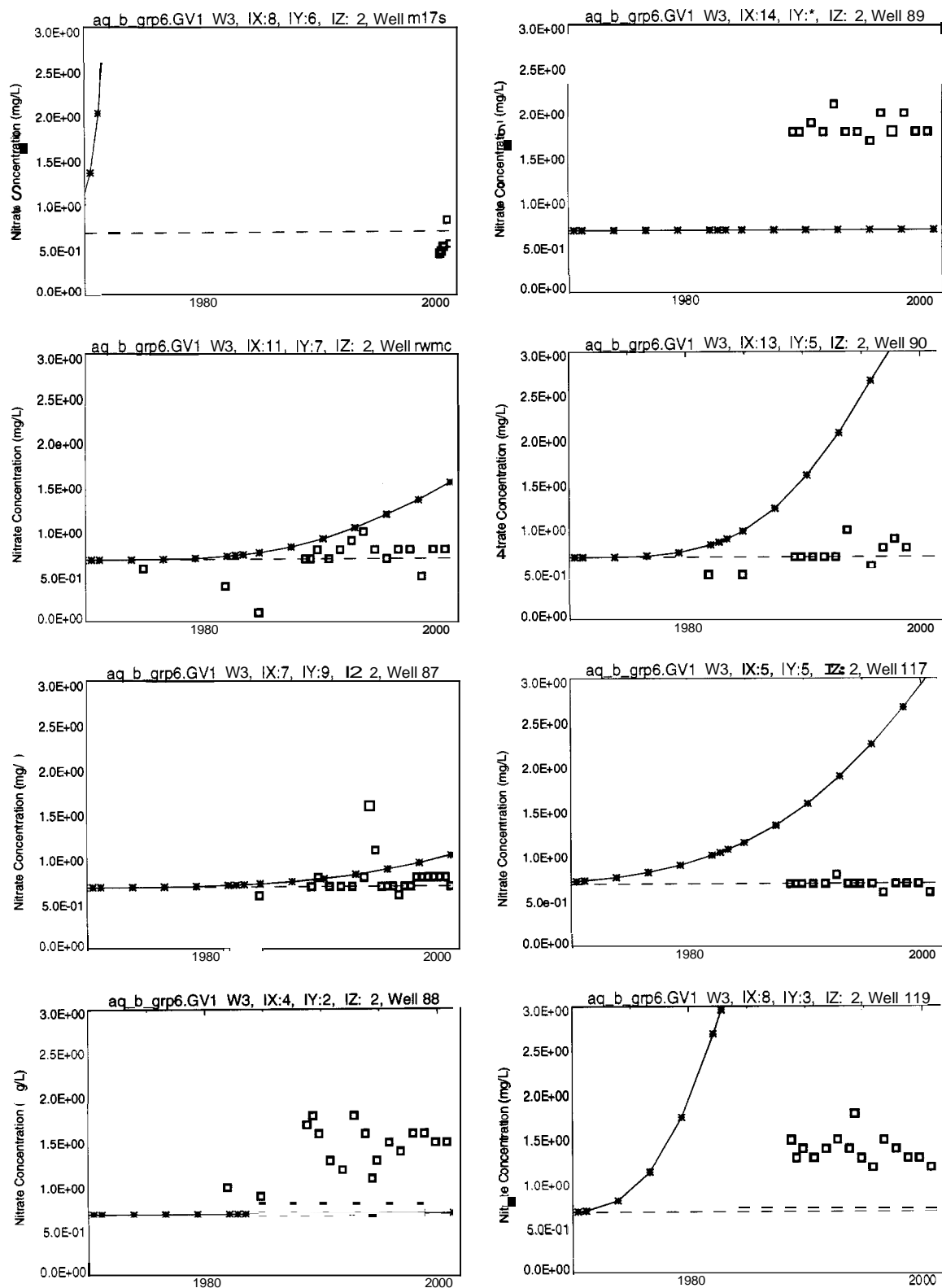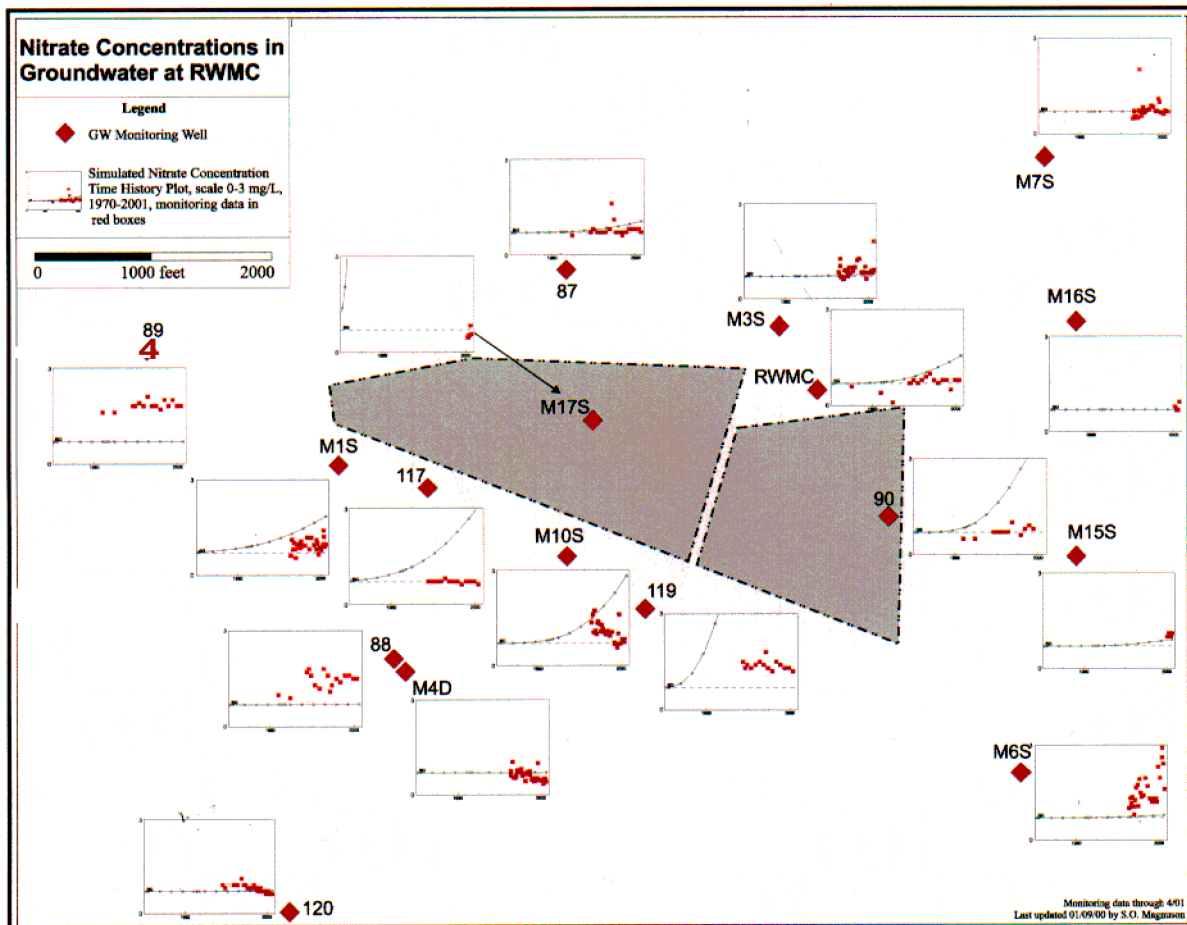
Figure 5-46. (continued).

Figure 5-47. Simulated and observed nitrate concentrations superimposed onto monitoring locations in the vicinity of the Radioactive Waste Management Complex.

SDA, also shows elevated concentrations and the most likely increasing trend that can be identified in any RWMC vicinity wells. Most of these monitoring data are consistent with the conceptual model of the aquifer flow system being dominated by a low-permeability region to the south and southwest of the SDA that directs flow eastward around the low permeability system Well 117 data are contradictory, which may be caused by very low formation permeability at this location limiting communication with the nitrate contaminant plume and resulting in elevated concentrations at Wells M10S and 119. A contour plot of the simulated nitrate concentrations in calendar year 2001 is shown in Figure 5-48 for both the base and refined aquifer simulation domain. The estimated local background of 0.7 mg/L is not added to the simulation results in this figure. The simulated results are similar to those predicted for nitrate in the IRA model (Magnuson and Sondrup 1998).

In *comparing* simulation results to monitoring results, concentrations are over predicted in Wells M1S, I 17, M10S, and 119 immediately south of the SDA; in Well M17S inside the SDA; and in Well 90 and the RWMC Production Well east of the SDA. Concentrations are under predicted in Well M6S to the southeast of the SDA. The observed high nitrate concentrations at the Well M6S aquifer monitoring location are the only monitoring results that appear to show an increasing trend. An eastward component exists in the simulated aquifer water velocities under the eastern portion of the RWMC that results in the simulated nitrate concentrations increasing at the grid block representing Well M6S. However, the simulated concentrations had just barely begun increasing by calendar year 2001. Other factors also contribute to the under prediction at the location of Well M6S. This location is just outside
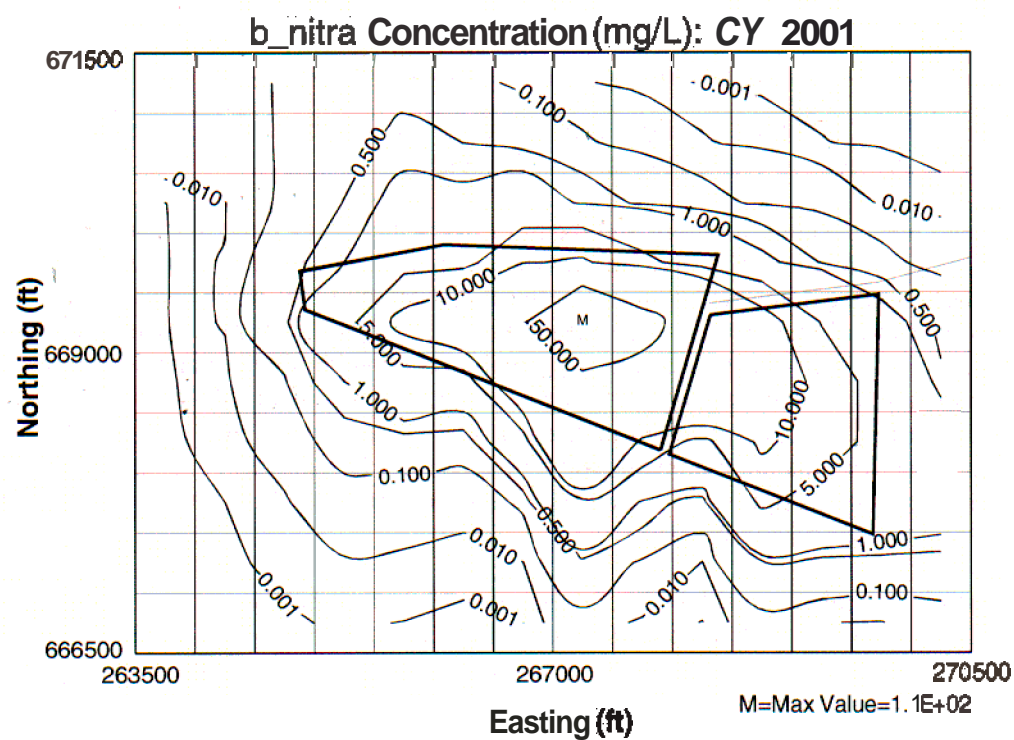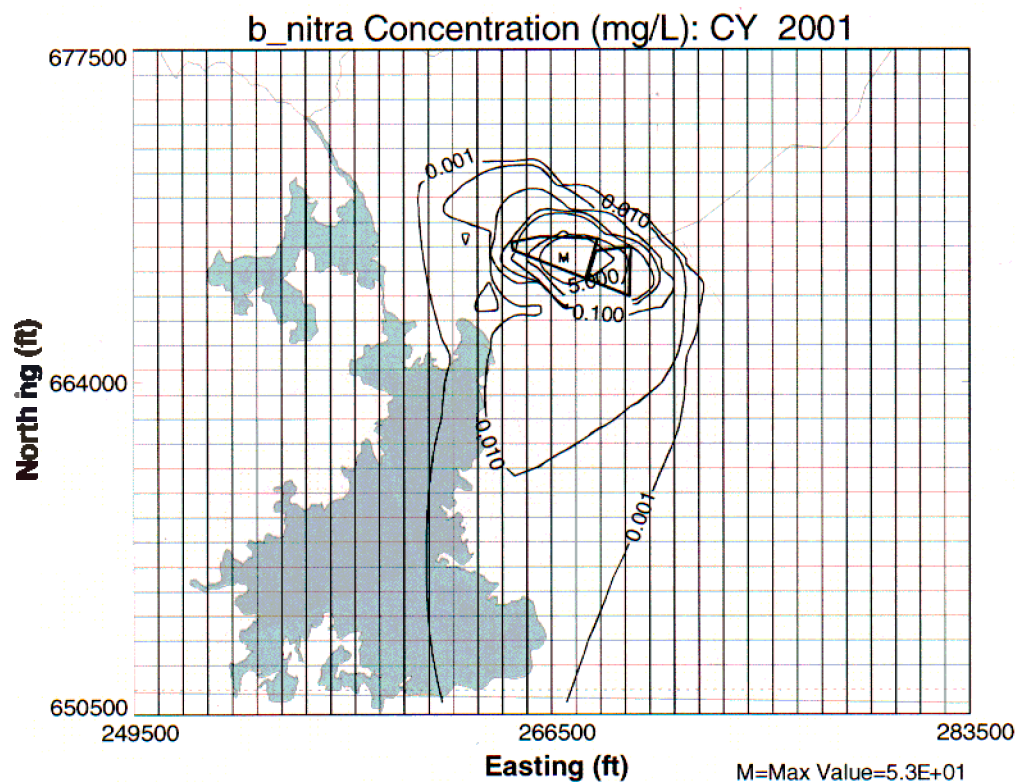
b_nitra Concentration (mg/L): CY 2001

M=Max Value=5.3E+01

b_nitra Concentration (mg/L): CY 2001

M=Max Value=1.1E+02

Figure 5-48. Simulated aquifer nitrate concentrations for calendar year 2001.
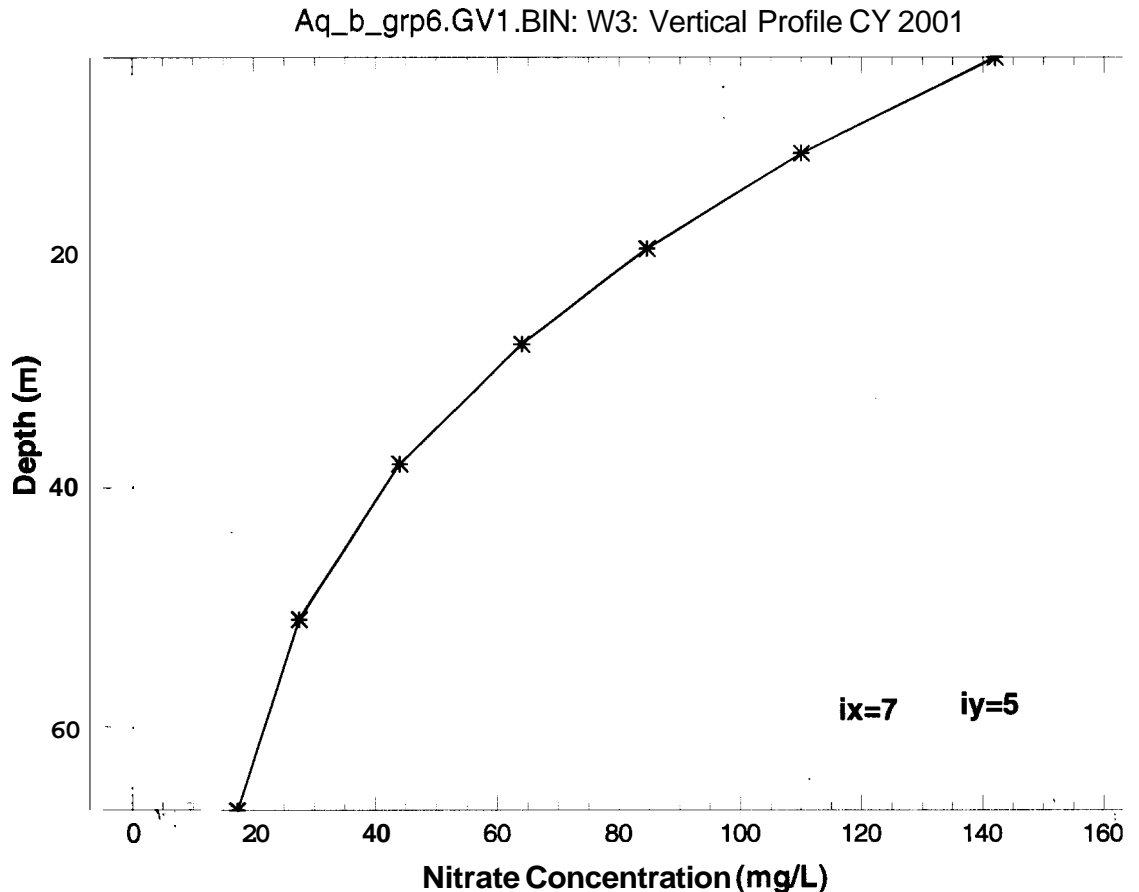
Figure 5-49. Simulated aquifer nitrate concentration profile beneath the Subsurface Disposal Area for calendar year 2001.

the area of grid refinement, so the concentrations are averaged over a grid block volume four times as large. In addition, the low-permeability region is simulated as if it extends almost to the M6S location. This causes simulated contaminants to continue to migrate eastward around this location.

A vertical profile of simulated nitrate concentrations in calendar year 2001 is shown in Figure 5-49. The concentrations decrease throughout the profile at each of the seven grid blocks representing the aquifer. As discussed below, concentrations used for determining risk are taken from the second grid block down, based on the typical screened interval in wells.

Calibration of simulated nitrate concentrations to the observed aquifer nitrate concentrations was not attempted for these simulations. Rather, simulations for both the vadose zone and the aquifer were developed based on best-available information. The only calibration consisted of optimizing agreement between the simulated and observed aquifer water levels. Simulations were then run once in a forward mode. With the exception of Well M6S, simulated concentrations at all locations are either over predicted when compared to measured values, or match measured values as long as the estimated background concentration of 0.7 mg/L is assumed. Except for the under prediction at Well M6S, it would be possible to make a claim of conservatism for the transport model. Well M6S is located farthest southeast of the SDA and, therefore, the well most likely to be affected by an upgradient facility influence, if such an influence exists.

Obviously, the system is more complex than has been represented in the model. However, the model does provide a foundation for explaining most of the observed behavior and, thus, meets the goal of general representability. There is, however, substantial uncertainty associated with the results because of what is not explained by the model. This discussion has focused on the subsurface flow and transport model and does not address the lack of calibration for the source term model (see Section **5.1**). Results of the subsurface model are highly sensitive to the source-term inputs.

5.2.4.6.2 *Comparison of Simulated and Observed Chromium Concentrations —*
Chromium is another contaminant that was buried in the SDA for which transport was simulated. In these transport simulations, chromium was assumed to remain in the mobile hexavalent state. Though chromium is not considered as a COPC in the **ABRA,** an examination of how the subsurface model predictions for chromium compare to measured values is useful. Time histories of simulated chromium concentrations are compared to observed aquifer concentrations in Figure **5-50.** The monitored concentrations are inferred to represent hexavalent chromium also. The time history plots are all scaled consistently to the maximum observed field value, which was just under $100 \mu g/L$ in Well **M3S.** Similar to the time history plots for nitrate concentrations, the simulated chromium concentrations are added onto the estimated regional background concentration of **2.5** $\mu g/L$ for the Snake River Plain Aquifer (Orr, Cecil, and Knobel **1991).** Only simulated chromium concentrations for Well **M17S** begin to be discernable above background for the **1970** to calendar year **2001** timeframe presented in Figure 5-50. The maximum simulated chromium concentration anywhere in the aquifer through calendar year **2001** is **3.7** $\mu g/L$, including background. This is approximately an order of magnitude greater than the maximum simulated chromium concentration through the same period for the IRA model. Both models under predict observed values.

Field data for chromium are all greater than the reported background value, which gives rise to several interpretations. Elevated chromium concentrations could indicate that either the local background is greater than indicated in Orr, Knobel, and Cecil **(1991)** or that the SDA may be contributing to elevated chromium concentrations in these monitoring wells. Conversely, elevated chromium concentrations could imply that the interpretation is incorrect that SDA-vicinity aquifer concentrations are not affected by upgradient facilities such as the TRA.

5.2.5 Base Case Simulations for the Baseline Risk Assessment

The model developed for the ABRA was run for each COPC. This section presents concentration results from those simulations and makes comparisons to observed values. Results are presented graphically as time history comparisons to field monitoring results at grid locations representing SDA aquifer monitoring wells (Figures **5-51** through **5-57).** In contrast to results presented previously for nitrate and chromium, no background concentration is added to these simulation results. Local background concentrations are zero for the COPCs presented in Figures **5-51** through **5-57,** based either on evaluations in Section **4** or in Orr, Cecil, and Knobel **(1991).** Results also are presented below in a table comparing simulated maximums through calendar year **2001** to observed values. Refer to Figure **5-47** when locating wells indicated in the figures. Monitoring results for radionuclide COPCs that represent 3σ detections or greater are included as blue diamonds on the time history plots along with a whisker-style indication of their associated **1o** uncertainties. In cases where analyses were performed but no COPCs were detected, nondetects are plotted in red at the extreme lower bound of the plot. Simulation results are portrayed as a continuous line with black asterisks. Simulation results representing all wells, except Well **M4D,** are taken from the second slice down in the aquifer model. Well M4D is unique in that it is screened much deeper, so simulated concentrations from deeper in the model are used. The second slice of grid blocks was from a depth of 8 to **16** m (**26** to **52** ft) in the aquifer domain and is similar to
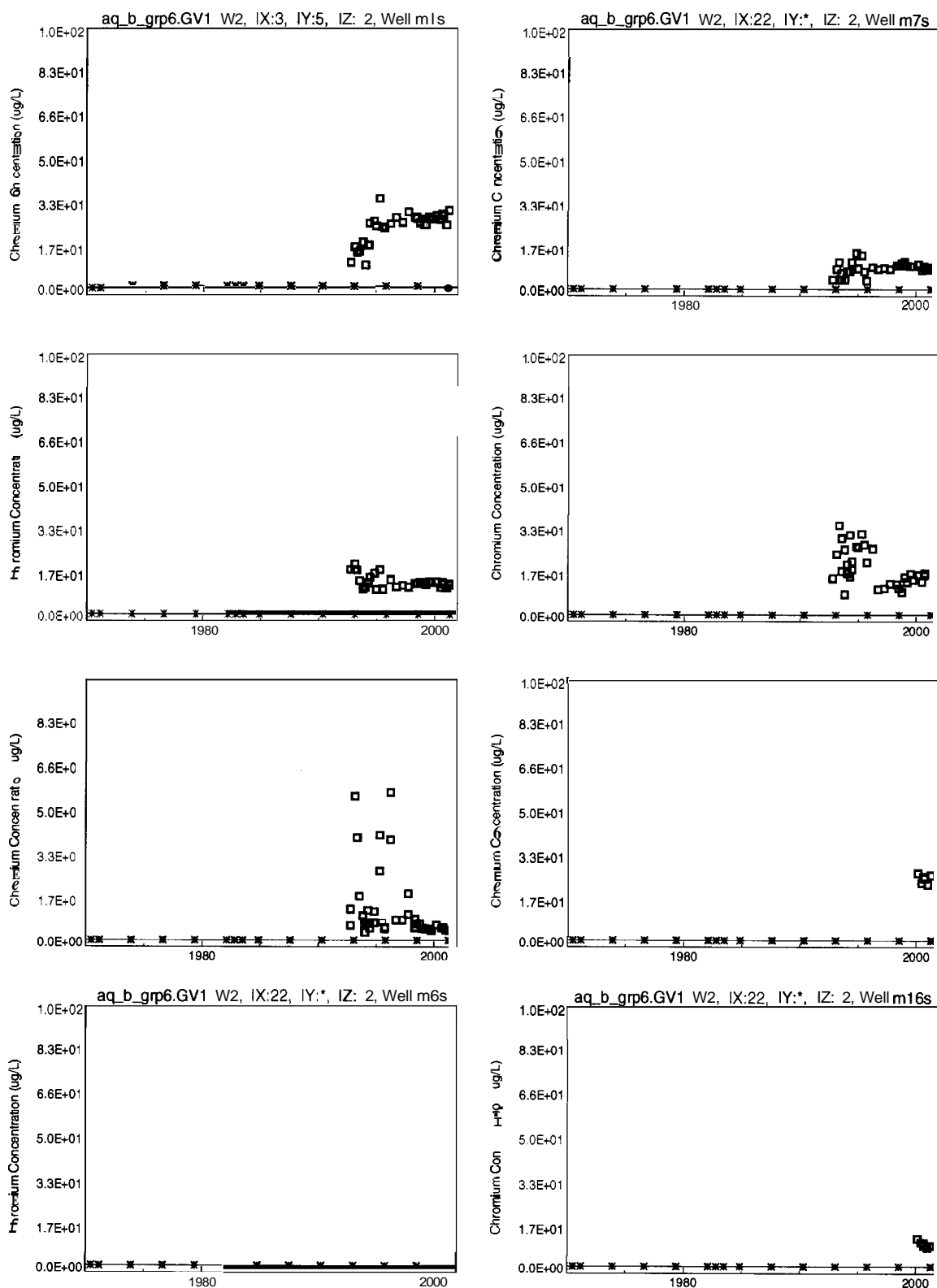
Figure *5-50.* **Comparison of simulated and observed chromium concentration time histories for aquifer monitoring wells in the vicinity of the Subsurface Disposal Area.**
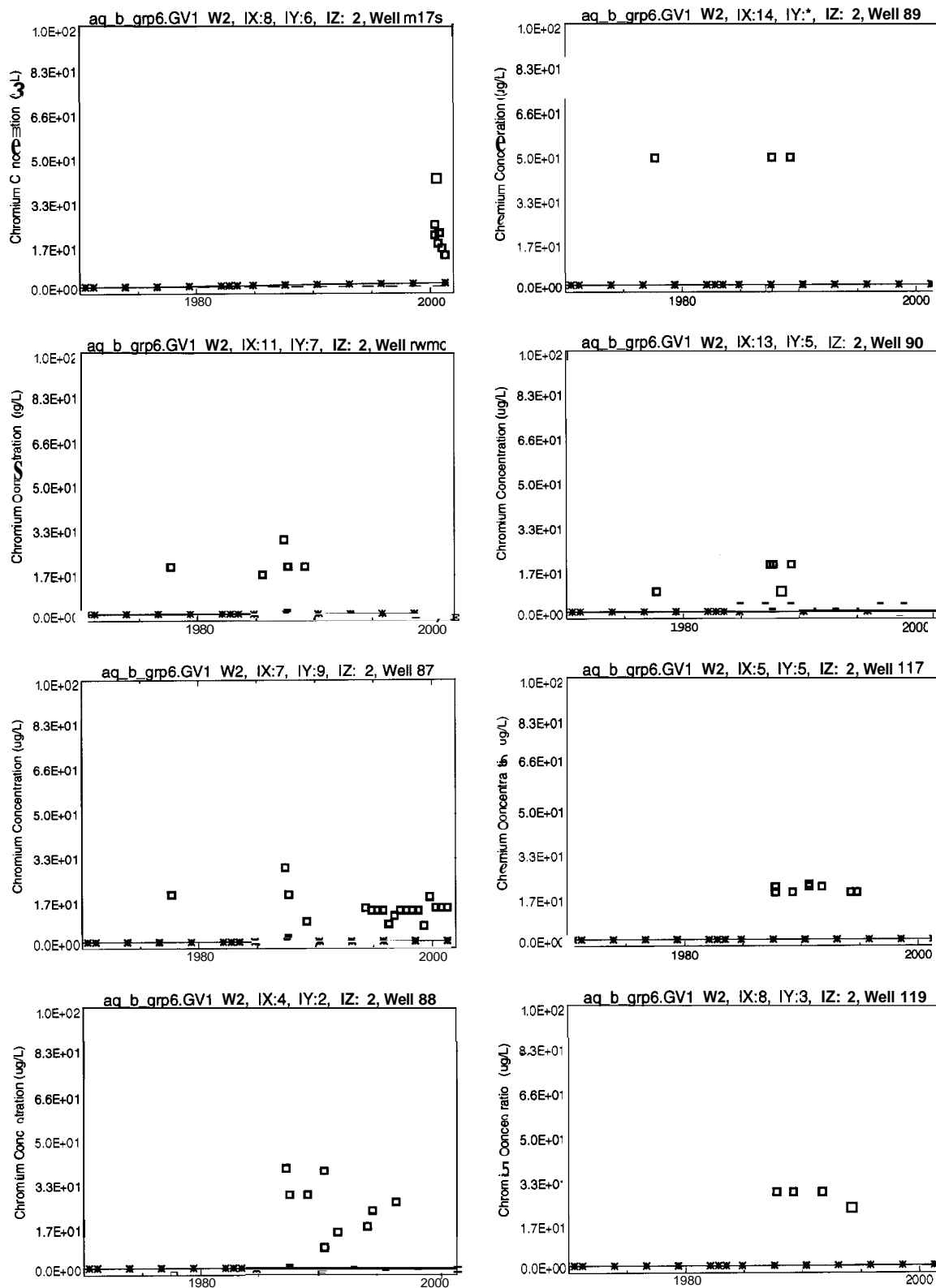
Figure 5-50. (continued).

most of the screened intervals in the monitoring wells. As such, simulated concentrations represent concentrations at a depth of 12 m (39 ft) below the water table.

Results in Figures 5-51 through 5-57 highlight the erratic nature of detections compared to the majority of nondetect results. Sporadic detections include low-level actinide concentrations that are just at instrument detection limits and may be false-positives.

Table 5-17 lists maximum simulated concentration anywhere in the aquifer through calendar year 2001 for chromium and all human health COPCs and their long-lived decay-chain progeny. No background concentrations are added to any of the simulated results. Almost all of the simulated peak values in Table 5-17 occur during calendar year 2001, indicating that concentrations were still increasing at that time. Two exceptions were Pu-238, which was simulated to not be in the aquifer anywhere at any concentration, and Cl-36, which peaked earlier in 1994. For comparison, the corresponding maximum simulated chromium concentrations through 1995 from the IRA model are given in the third column of the table. Estimated background concentrations from Knobel, Orr, and Cecil (1992) are shown in the fourth column of the table. Uranium isotopes were estimated from proportioning the total uranium background concentration of 3 μg/L contained in Knobel, Orr, and Cecil (1992) into the respective isotopes in accordance with their known specific activity and isotopic abundance (weight percent) known to exist in nature. The last two columns present the range of observed values taken from the nature and extent discussion in Section 4 along with comments concerning some of those values. Observed values from earlier than 1987 are not presented in Table 5-17. Numerous COPCs do not have corresponding analyses, as indicated in the table.

Changes in simulated values between the **ABRA** model and the IRA model result primarily from the following: (a) differences in the use of best-estimate and revised inventories, (b) different source release rates for activation and fission products attributable to changes in the assigned corrosion rates, (c) use of smaller partition coefficients for C-14, (d) differences in simulated water travel times through the vadose zone caused by including spatially variable hydrologic properties for the B-C and C-D interbeds, and (e) the conformable gridding approach. Regarding the latter, using a conformable grid most likely resulted in less numerical dispersion because of improved uniformity of grid sizes across lithologic interfaces. Less numerical dispersion would result in lower simulated concentrations for those contaminants that strongly adsorb, such as Am-241 and the plutonium isotopes, because a contaminant would not be artificially "smeared" ahead of its advective front.

In comparing simulated results from the ABRA model to the range of observed 3σ detections or the background concentrations, several patterns emerge. Simulated aquifer concentrations for fission products (i.e., Tc-99 and I-129) and the activation products (i.e., C-14 and Cl-36) are all over predicted to varying degrees compared to observed monitoring results. This over prediction is thought to be more likely caused by inadequacies in the source release model than in the subsurface flow and transport model. Monitoring results for U-234, U-235, and U-238 are similar to reported background values. Simulated uranium isotope values are slightly less than observed values or background values, indicating that simulated anthropogenic uranium is migrating but has not reached the aquifer in high enough concentrations to be detected yet. All other contaminants are predicted to be either not in the aquifer yet or to be present at concentrations below detectable levels. If it is assumed that background concentrations for anthropogenic radioisotopes are zero for those Contaminants not explicitly identified in Knobel, Orr, and Cecil (1992), then model results are in agreement with nondetections for this last group of contaminants. This statement disregards sporadic detections of plutonium isotopes and Am-241 as anomalies. At a minimum, for this latter set of contaminants, model results are not in conflict with observed results.
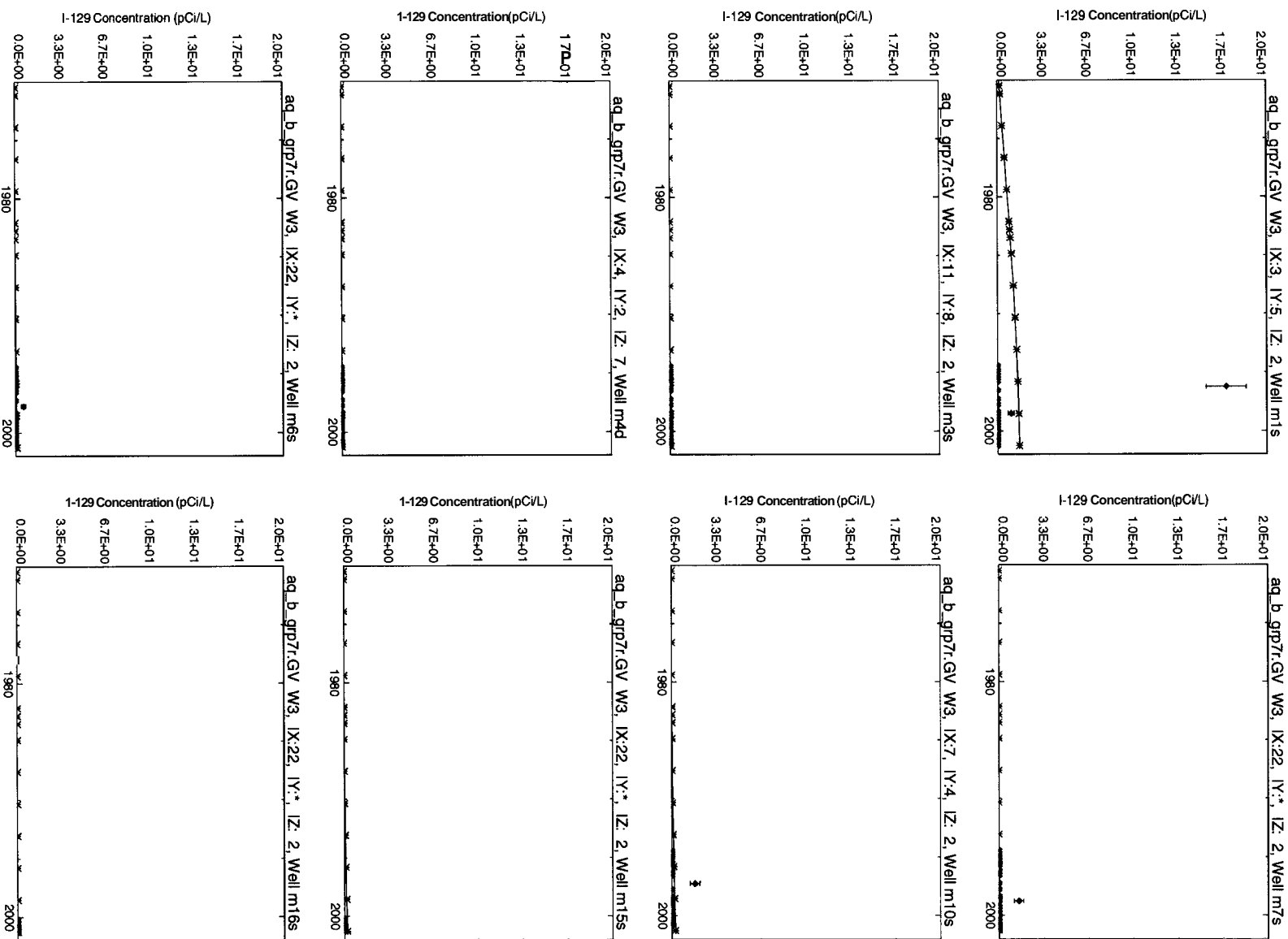
Figure 5-51. Comparison of simulated and observed I-129 concentration time histories for aquifer monitoring wells in the vicinity of the Subsurface Disposal Area.
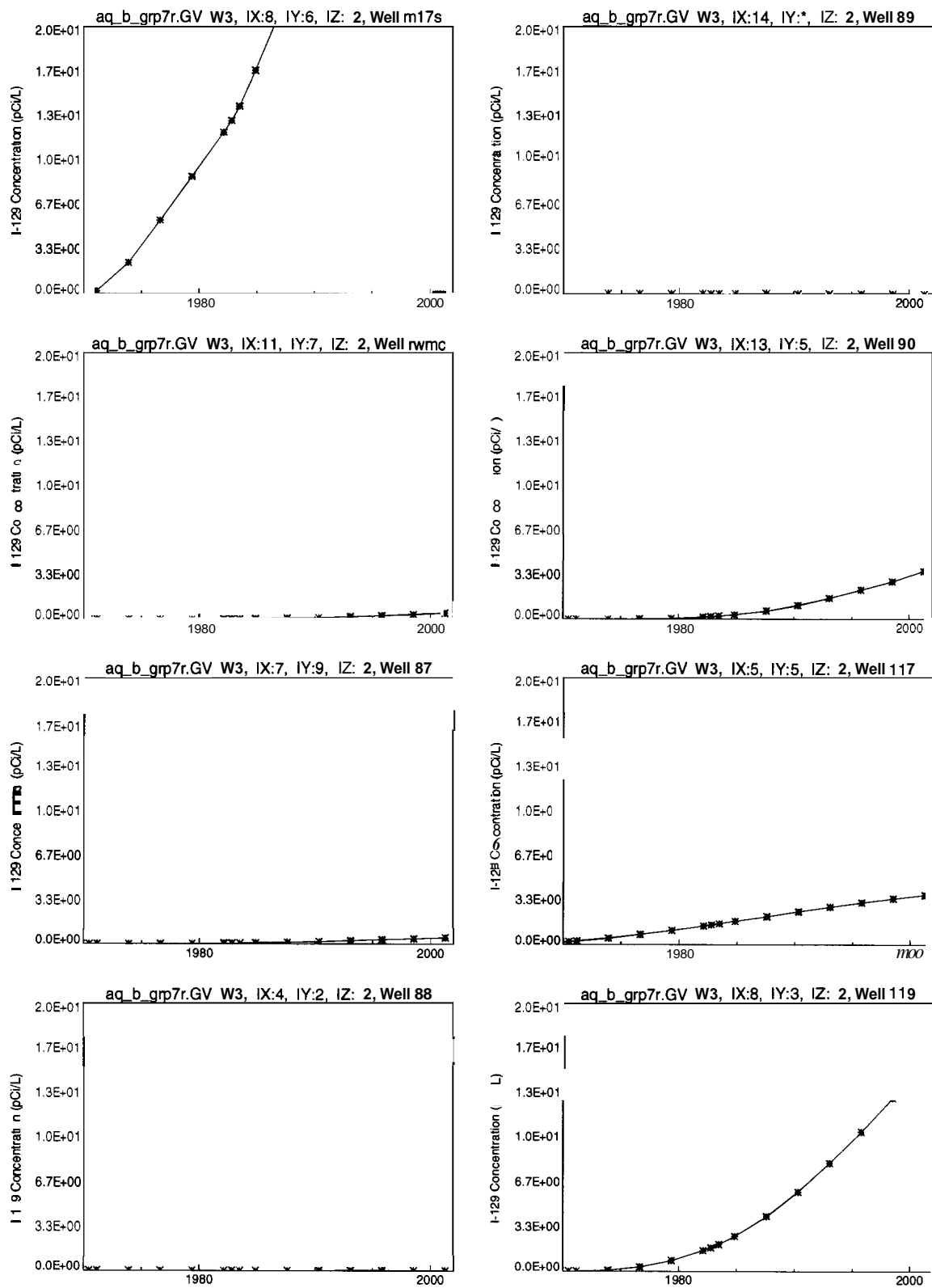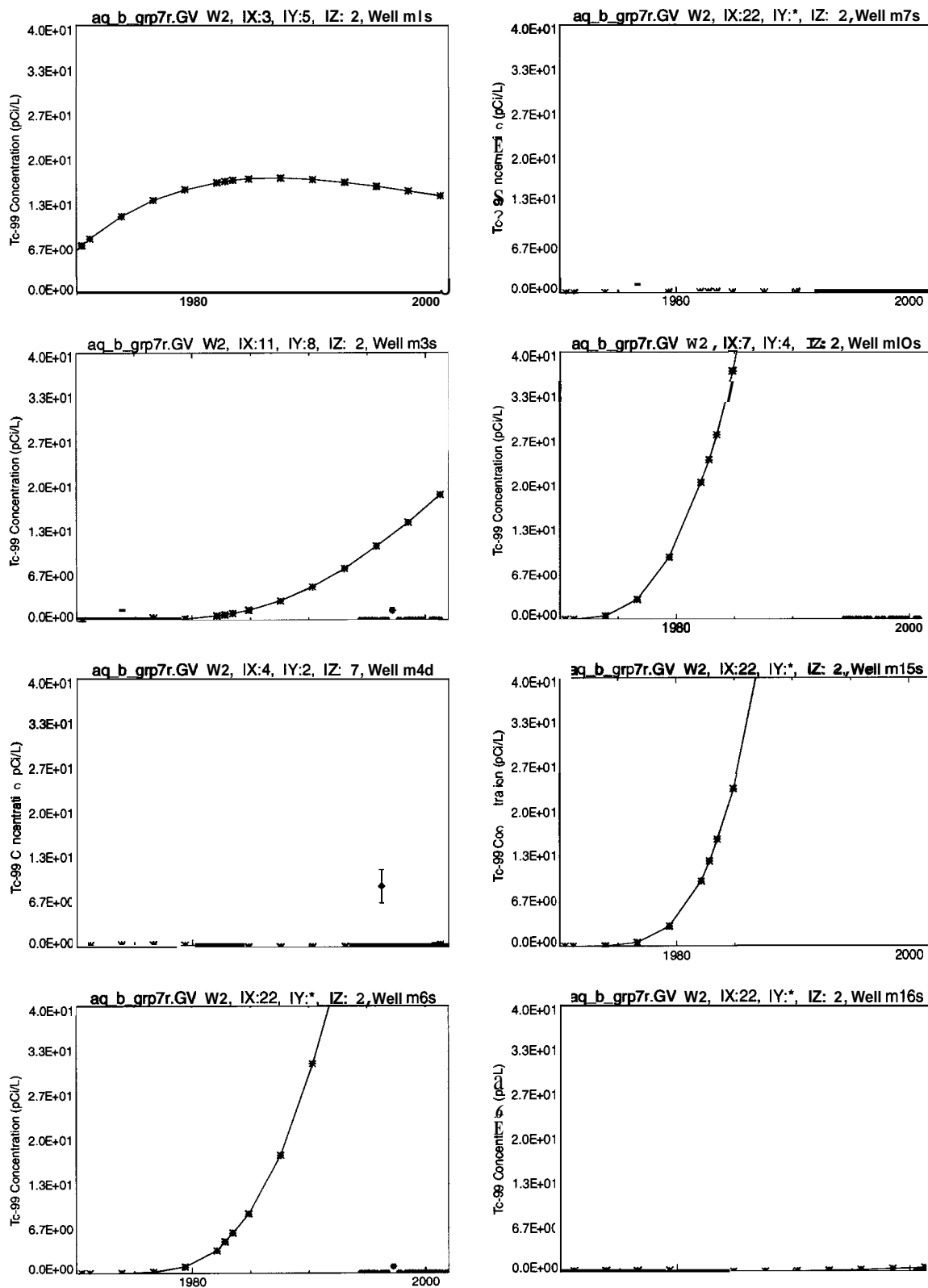
Figure 5-51. (continued).

Figure 5-52. Comparison of simulated and observed technetium-99 concentration time histories for aquifer monitoring wells in the vicinity of the Subsurface Disposal Area.
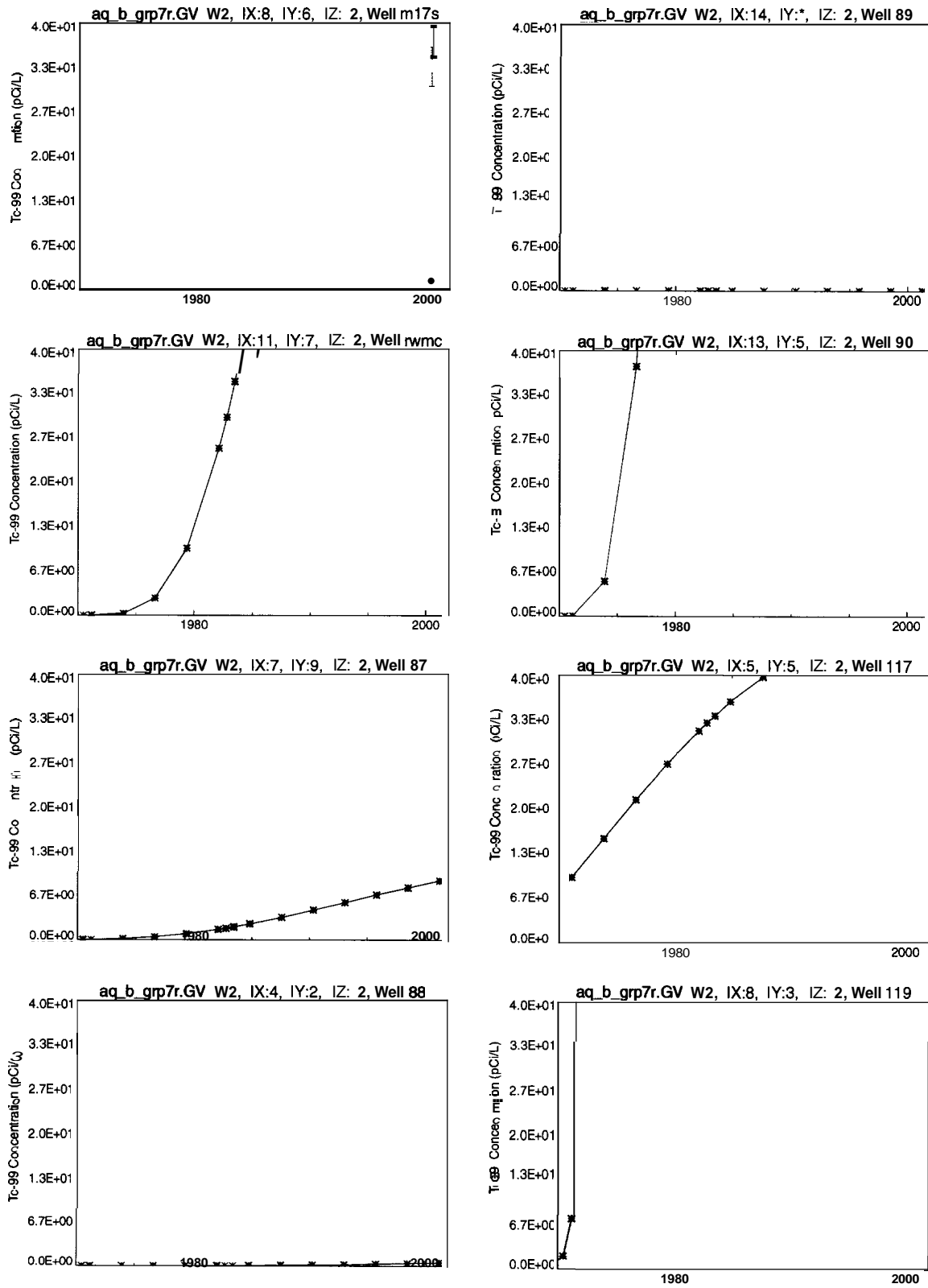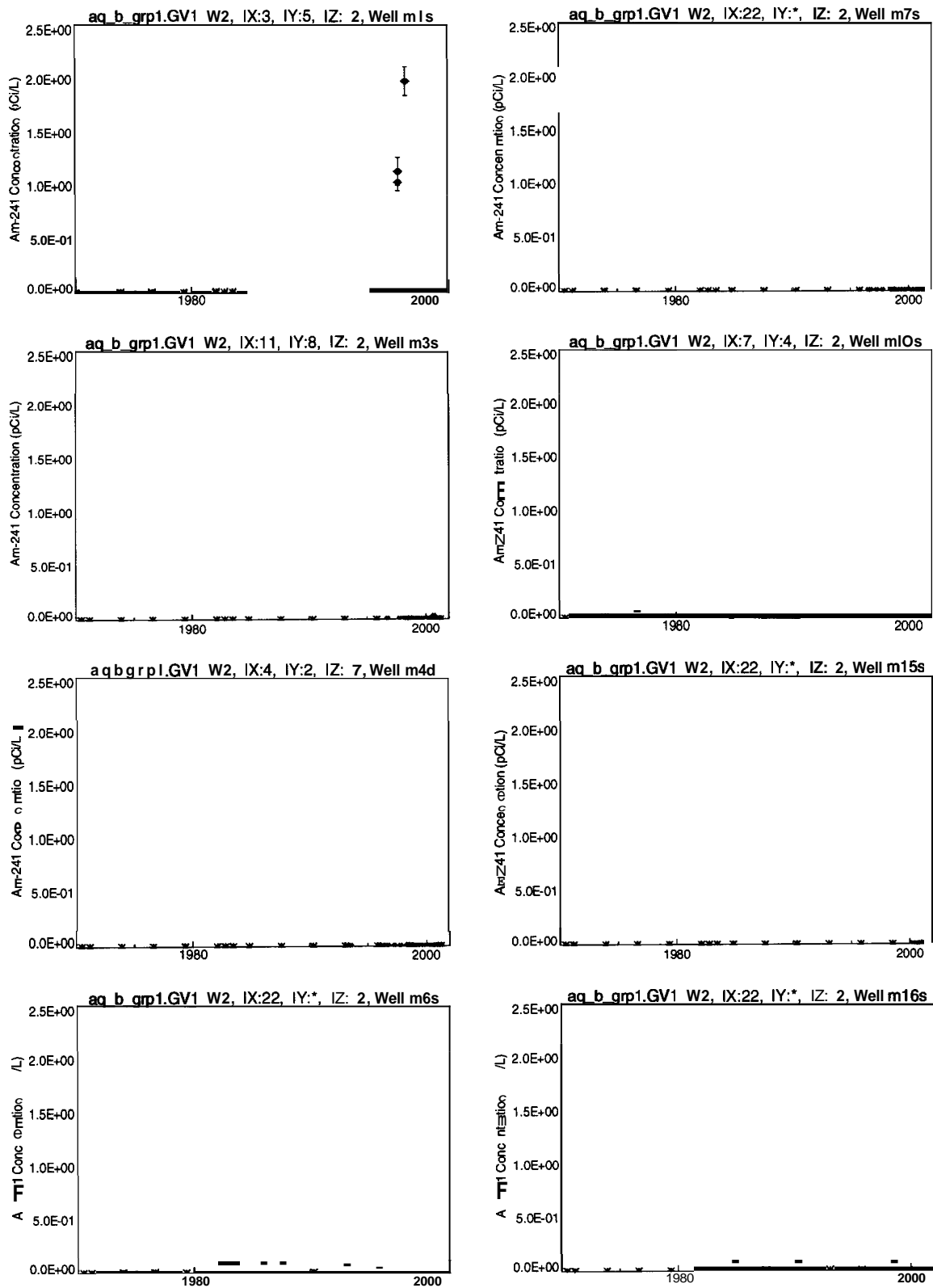
Figure 5-52. (continued).

Figure 5-53. Comparison of simulated and observed Am-241 concentration time histories for aquifer monitoring wells in the vicinity of the Subsurface Disposal Area.
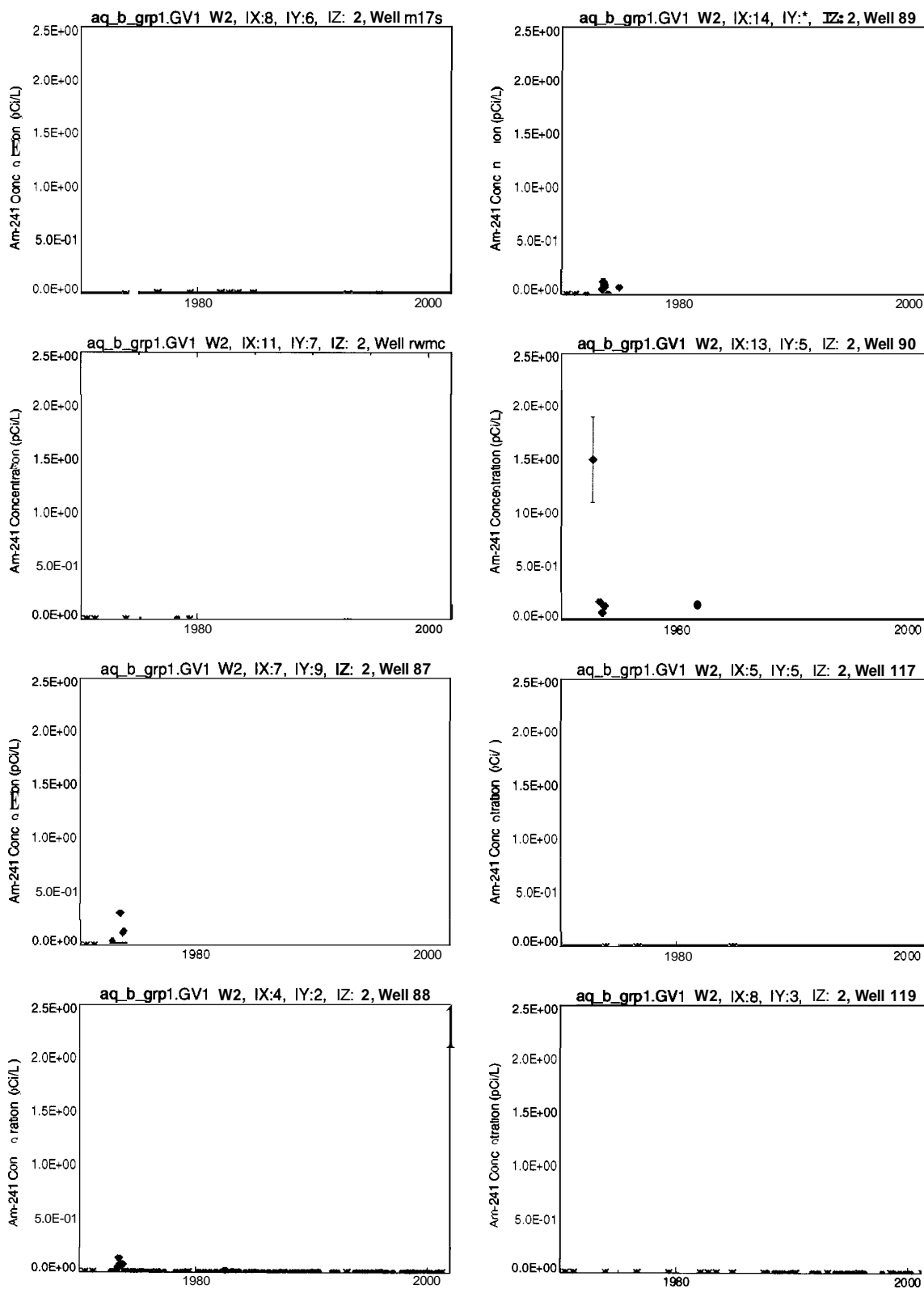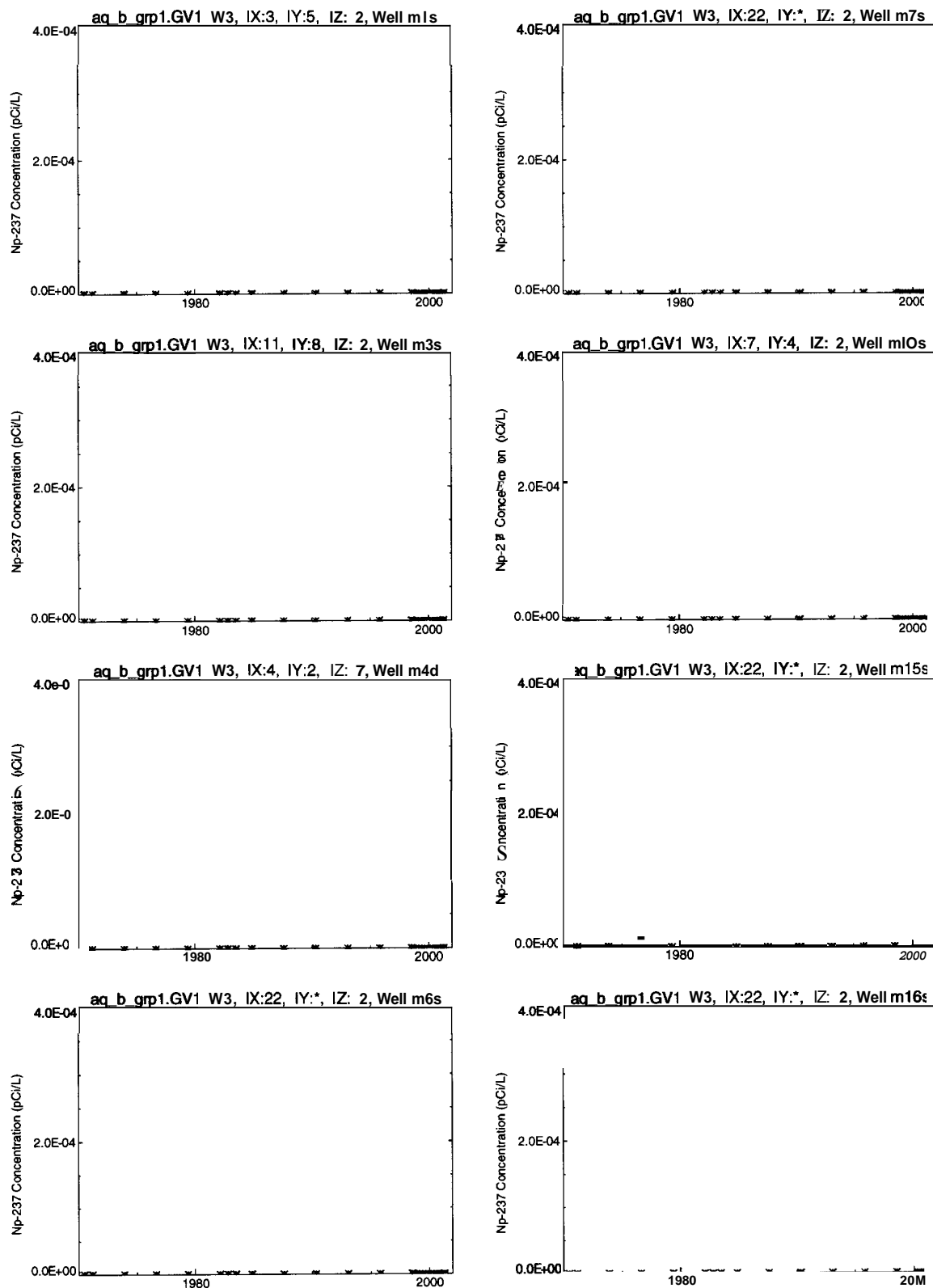
Figure 5-53. (continued).

Figure 5-54. Comparison of simulated and observed Np-237 concentration time histones for aquifer monitoring wells in the vicinity of the Subsurface Disposal Area.

Figure 5-54. (continued).

Np-237 Concentration (pCi/L)

4.0E-04   2.0E-04   0.0E+00

aq_b_grp1.GV1_W3, IX:8, IY:6, IZ: 2, Well m17s

Np-237 Concentration (pCi/L)

4.0E-04   2.0E-04   0.0E+00

aq_b_grp1.GV1_W3, IX:11, IY:7, IZ: 2, Well rwmc

Np-237 Concentration (pCi/L)

4.0E-04   2.0E-04   0.0E+00

aq_b_grp1.GV1_W3, IX:7, IY:9, IZ: 2, Well 87

Np-237 Concentration (pCi/L)

4.0E-04   2.0E-04   0.0E+00

aq_b_grp1.GV1_W3, IX:4, IY:2, IZ: 2, Well 88

Np-237 Concentration (pCi/L)

4.0E-04   2.0E-04   0.0E+00

aq_b_grp1.GV1_W3, IX:14, IY:*, IZ: 2, Well 89

Np-237 Concentration (pCi/L)

4.0E-04   2.0E-04   0.0E+00

aq_b_grp1.GV1_W3, IX:13, IY:5, IZ: 2, Well 90

Np-237 Concentration (pCi/L)

E-04

a_b_grp1_GV1 W3, IX:5, IY:5, IZ: 2, Well 117

Np-237 Concentration (pCi/L)

4.0E-04   2.0E-04   0.0E+00

aq_b_grp1.GV1_W3, IX:8, IY:3, IZ: 2, Well 119

1980   2000

Figure 5-55. Comparison of simulated and observed Pu-238 concentration time histories for aquifer monitoring wells in the vicinity of the Subsurface Disposal Area.
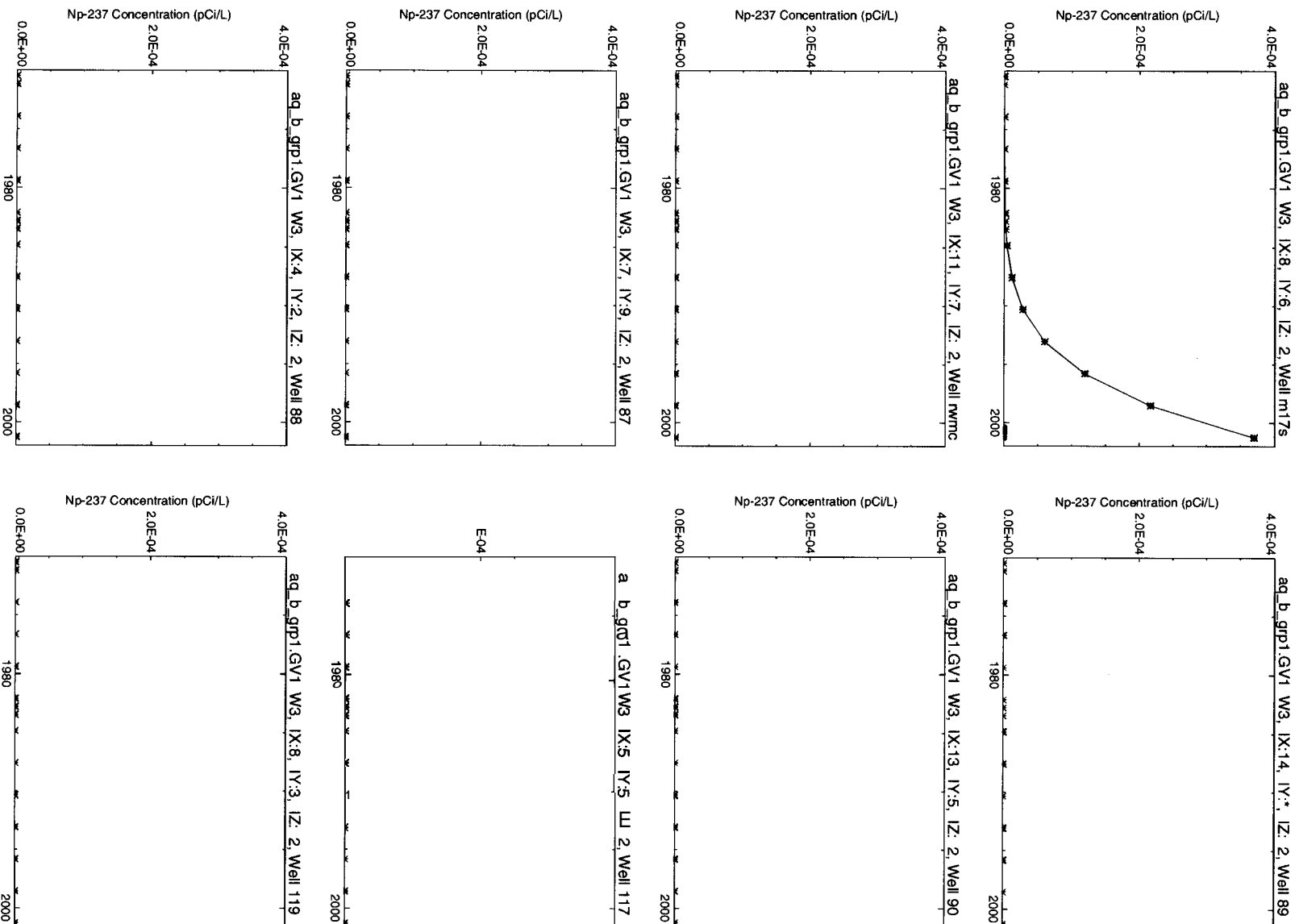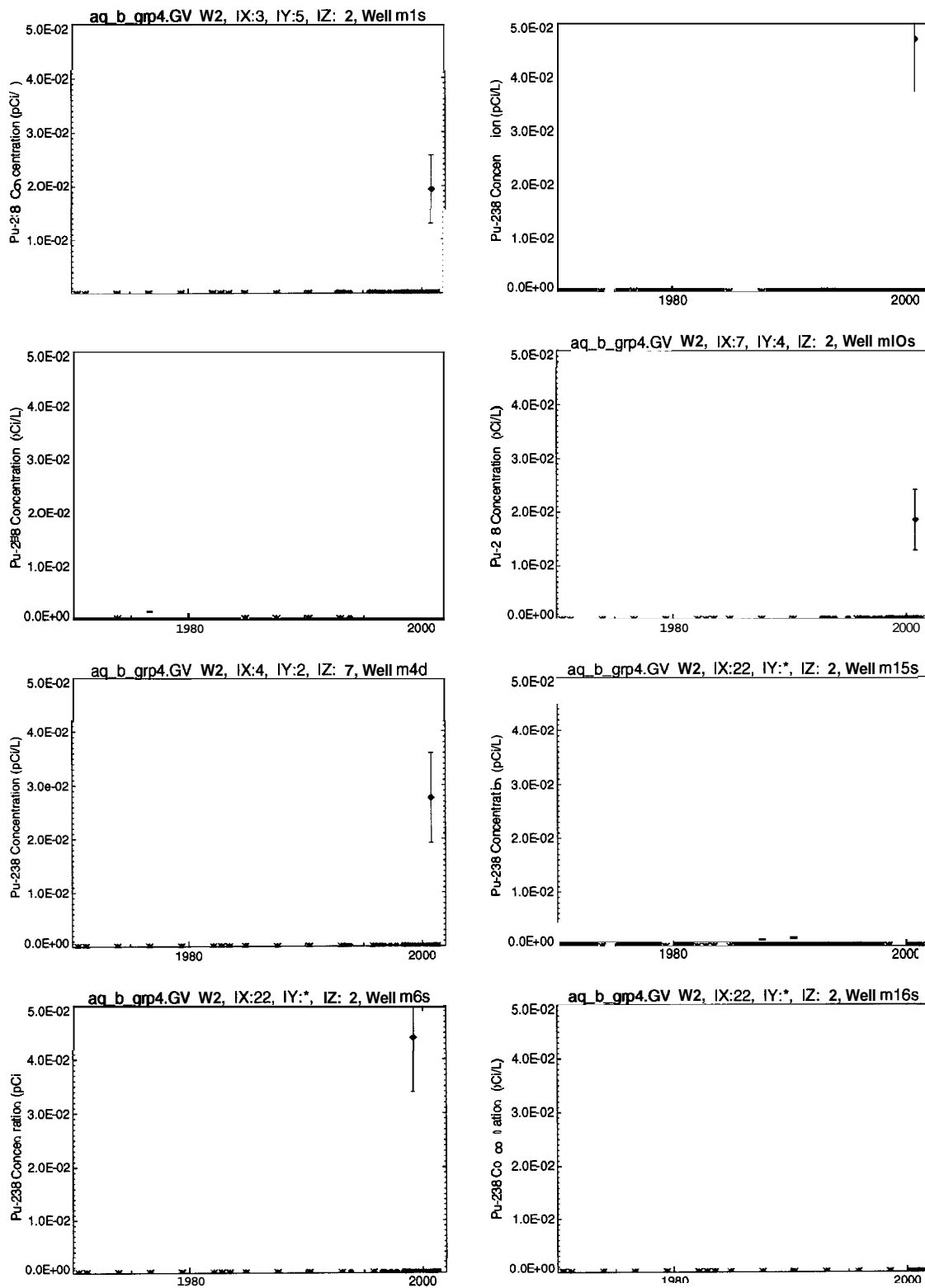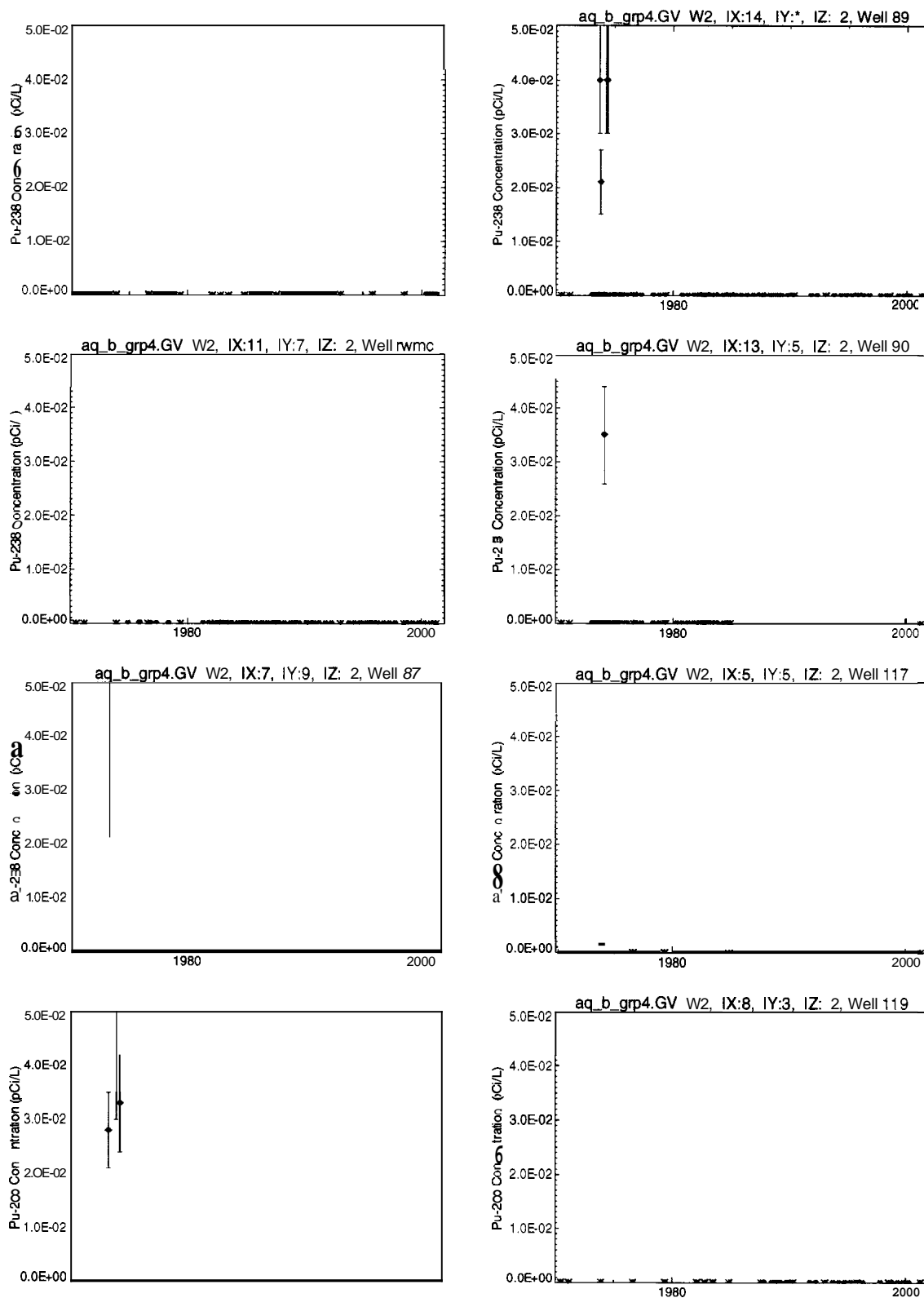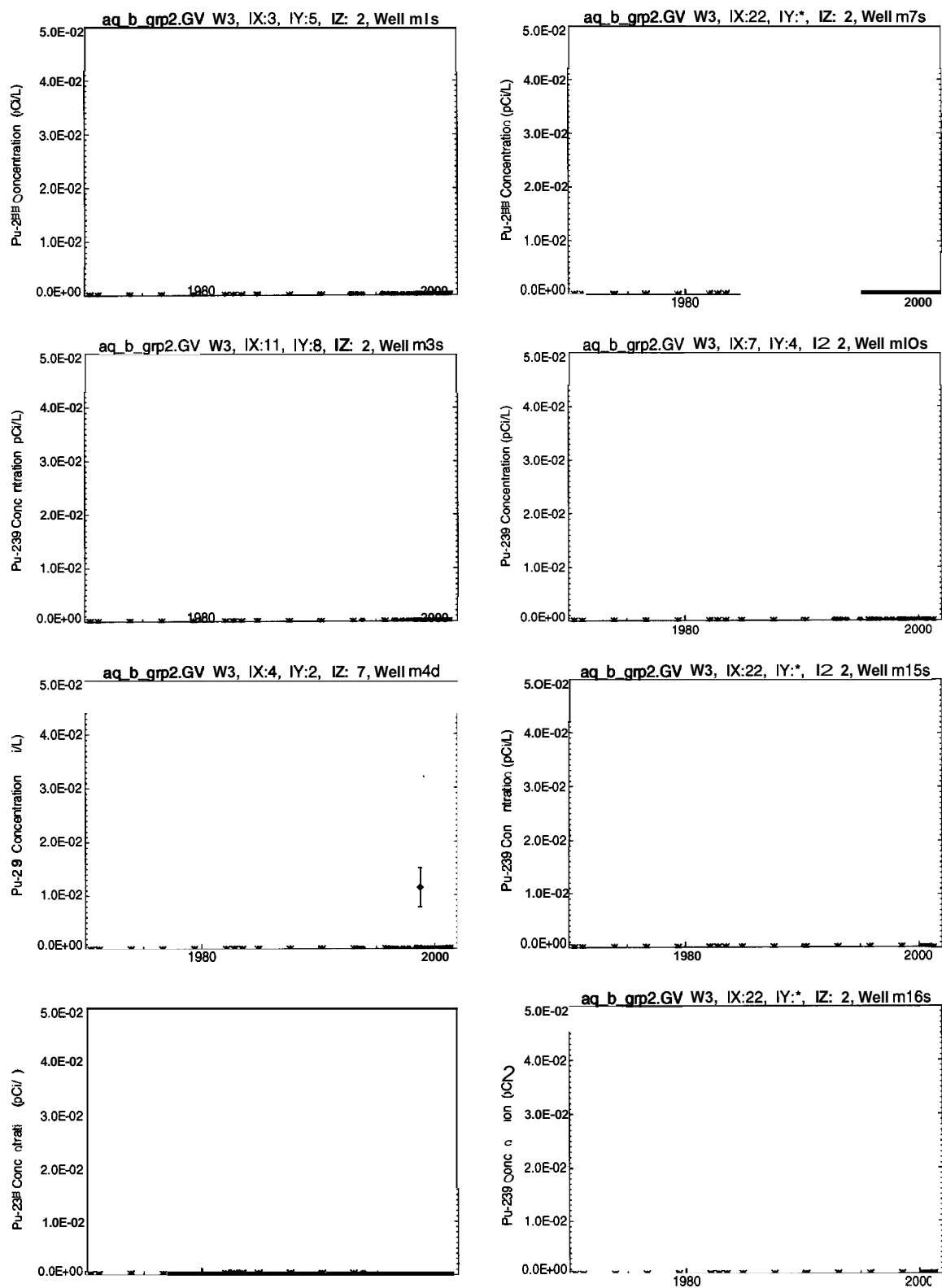
Figure 5-55. (continued).

Figure 5-56. Comparison of simulated and observed Pu-239 and Pu-240 concentration time histories for aquifer monitoring wells in the vicinity of the Subsurface Disposal Area.
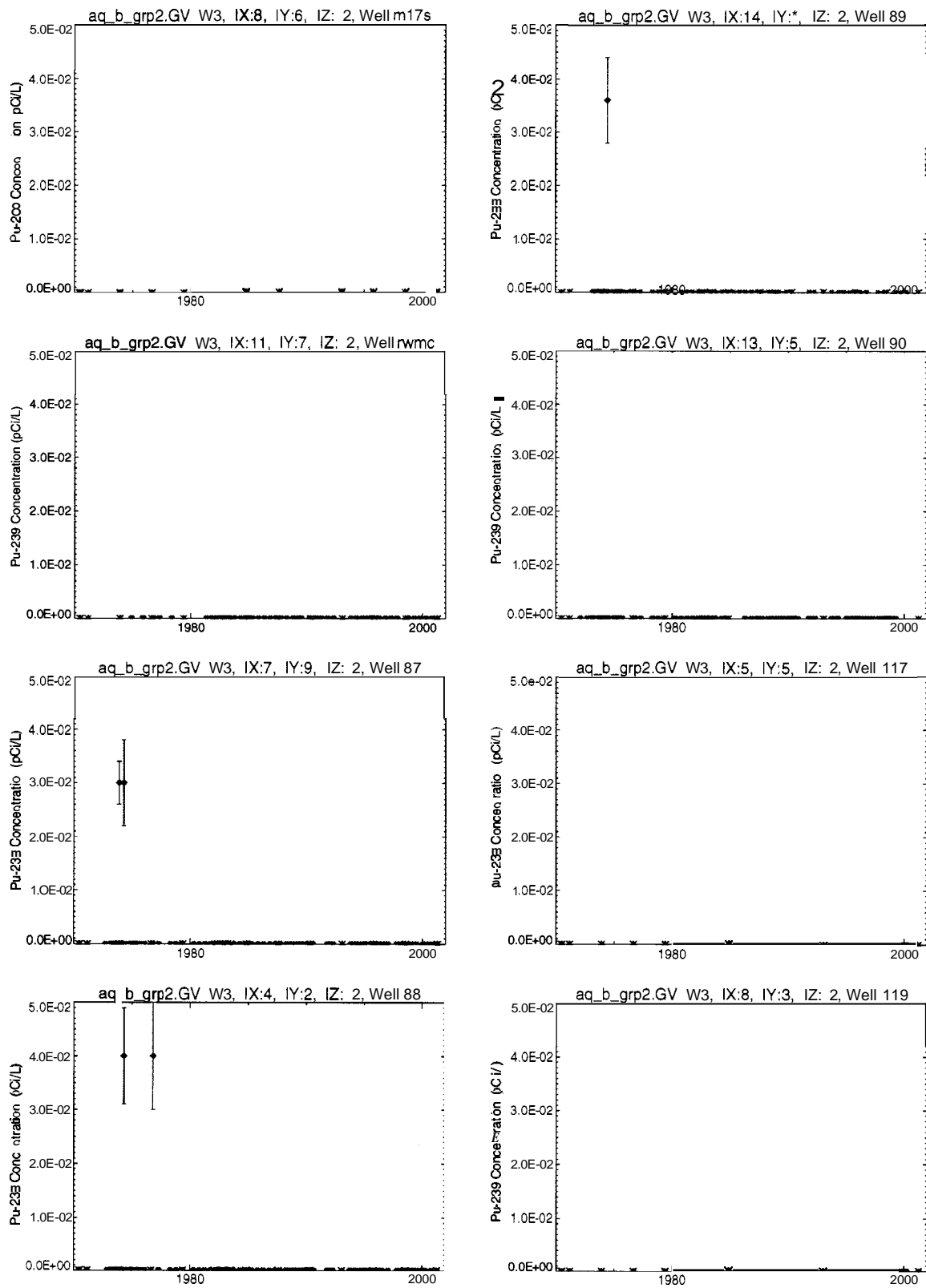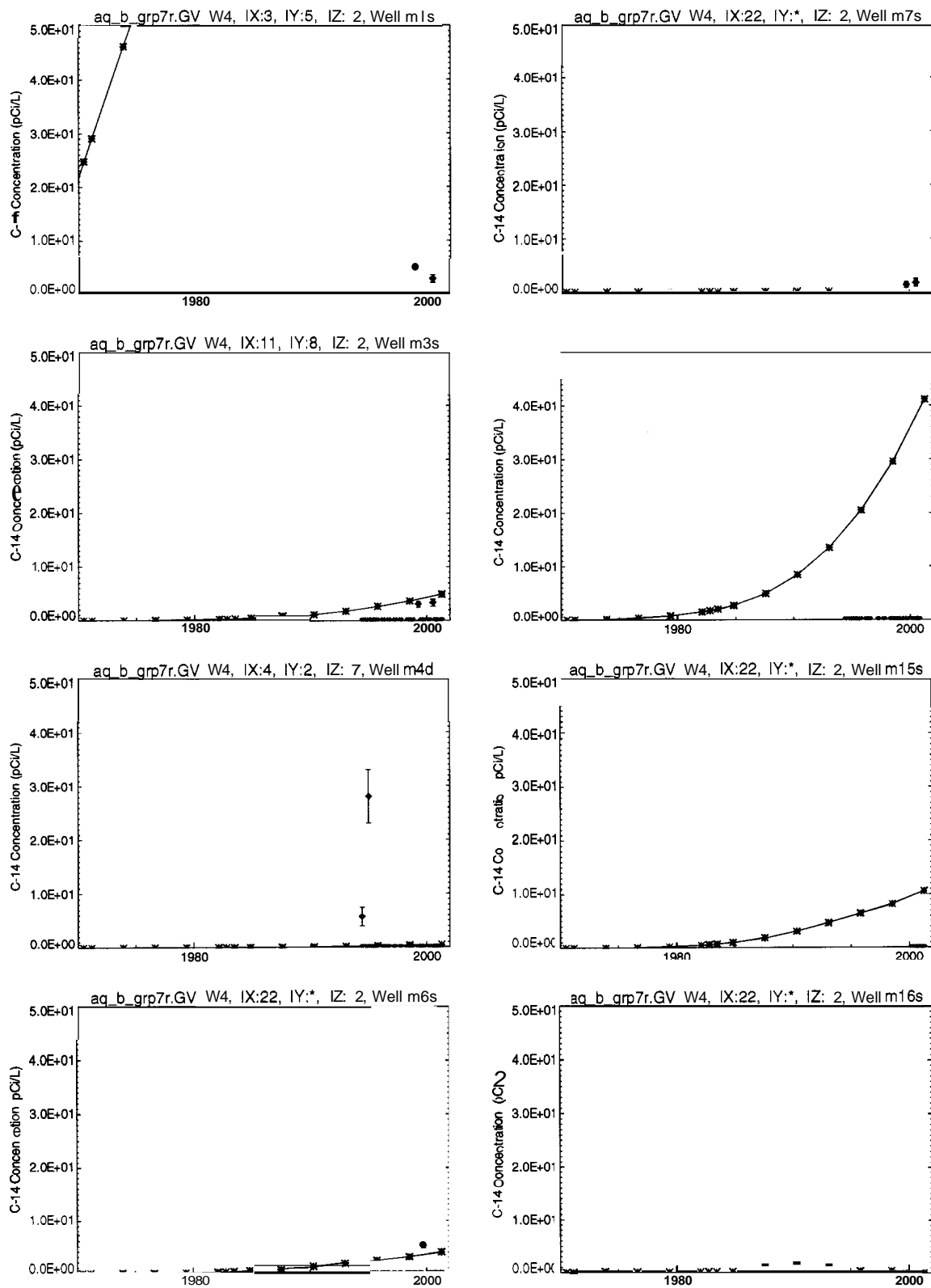
Figure *5-56.* (continued).

Figure 5-57. Comparison of simulated and observed C-14 concentration time histories for aquifer monitoring wells in the vicinity of the Subsurface Disposal Area.
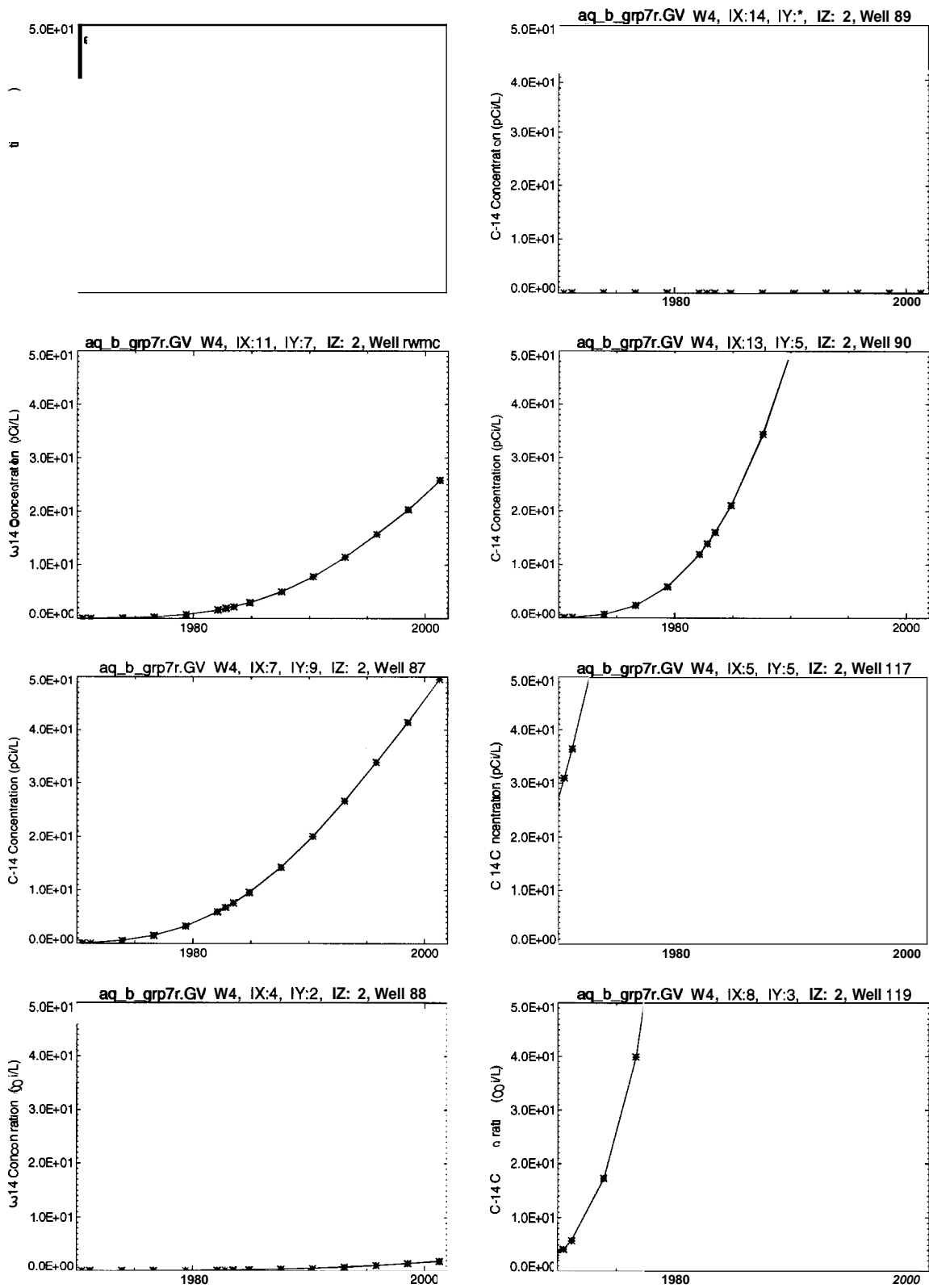
Figure 5-57. (continued).

Table **5-**17. Comparison of model concentrations and observed concentrations with no adjustments for background concentrations.

Contaminant of Potential Concern[a]	Baseline Risk Assessment Model Maximum Simulated Concentration at 12-m Depth through Year 2001 (pCi/L)	Interim Risk Assessment Model Maximum Simulated Concentration at 12-m Depth through Year 1995 (pCi/L)	Background Concentrations (Oк, Cecil, and Knobel 1992) (pCi/L)[b]	Range of Observed 1σ Concentrations in Subsurface Disposal Area Vicinity Wells Since 1987 (pCi/L or µg/L)[c]	Comments on Observed 3σ Concentrations'
Ac-227	5E-07	6E-08	NA	No analyses[d]	None
Am-241	9E-17	1E-06	0	0.026 to 1.97	None
Am-243	7E-24	2E-11	0	No analyses	None
C-14	3E+03	5 E+00	NA	1.8 to 28.0	Analysis began in 1994.
Cl-l36	3E+02	1E+00	NA	All nondetects	Analyses for Cl-36 began in year 2001. Cl-36 analysis will be done annually.
1-129	5E+01	4E+00	0	0.59 to 17.0	None
Nb-94	1E-23	1E-14	NA	No analyses	None
Np-237	4E-04	8E-04	NA	All nondetects	None
Pa-231	7E-06	1E-06	NA	No analyses	None
Pb-210	3E-10	4E-08	NA	No analyses	None
Pu-238	0	1E-12	0	0.018 to 0.37	NA
Pu-239	5E-28	2E-11	0	0.094 to 4.3	None
Pu-240	3E-30	7E-12	0	0.094 to 4.3	None
Ra-226	4E-09	1E-08	0.0 to 0.1	4.0 to 5.4	Gamma spectroscopy results with inadequate sensitivity. Values shown are near detection limits, use with caution.
Tc-99	4E+04	5E+01	NA	0.97 to 35.4	None
Th-229	1E-06	4E-08	NA	No analyses	None
Th-230	3E-06	8E-7	NA	No analyses	None
Th-232	6E-13	1E-11	NA	No analyses	None
U-233	4E-03	3E-04	0.	No analyses	NA
U-234	1E-01	5E-02	1.1	1.0 to 1.84	None

Table 5-17. (continued).

Contaminant of Potential Concern[a]	Baseline Risk Assessment Model Maximum Simulated Concentration at 12-m Depth through Year 2001 (pCi/L)	Interim Risk Assessment Model Maximum Simulated Concentration at 12-m Depth through Year 1995 (pCi/L)	Background Concentrations (Orr, Cecil, and Knobel 1992) (pCi/L)[b]	Range of Observed 1σ Concentrations in Subsurface Disposal Area Vicinity Wells Since 1987 (pCi/L or μg/L)[c]	Comments on Observed 3σ concentrations[d]
U-235	2E-02	3E-03	0.05	0.003 to 0.18	Gamma spectroscopy results with inadequate sensitivity. Values shown are near detection limits, use with caution.
U-236	4E-03	2E-03	0.	No analyses	None
U-238	3E-01	4E-02	1.1	0.21 to 0.88	Gamma spectroscopy results with inadequate sensitivity. Values shown are near detection limits, use with caution.
Nitrate (as N)	1E+02 mg/L	1.4E+01 mg/L	1.0 to 2.0 mg/L	0.28 to 2.9 mg/L	None
Chromium	1E+00 μg/L	1E-01 μg/L	2.0 to 3.0 μg/L	5.5 to 99.6 μg/L	Most other high chromium values were approximately 40 to 60 pCi/L

a. Observed values from earlier than 1987 are not presented in this table.

b. NA = information not available on background concentrations.

c. The range of observed values is taken from the nature and extent discussion in Section 4.

d. See the respective contaminant discussions in Section 4 regarding lack of analysis.

5.2.6   Baseline Risk Assessment Sensitivity Simulations

This section discusses the implementation of the simulations for the **ABRA** sensitivity analyses. Results, when presented, are in terms of water travel times and concentrations. Risk results are presented in Section 6. Often, these sensitivity simulations test assumptions used in the model and, as such, the simulations represent an assessment of conceptual uncertainty. For each sensitivity simulation of this type, the entire suite of potential contaminants was simulated. Other sensitivity simulations tested contaminant-specific parameters assigned in the model, and only those contaminants directly affected were evaluated.

5.2.6.1   Upper-Bound Inventories. A simulation suite was performed in which the upper-bound inventories were used instead of the best estimates. The only difference in the subsurface flow and transport models was that a different source term was supplied. Differences in risks are discussed in Section 6.

5.2.6.2   B-C Interbed Gaps. The method used to create the interbed upper surfaces and interbed thicknesses resulted from a consistent statistical approach that was based on all lithologic data available. The use of geostatistics to incorporate spatial variability was implemented and robustly tested by Leecaster (2002). For the **ABRA** model, kriging results were used without imposing any bias into them. In contrast, the kriging results for the IRA model were modified to enforce gaps in the interbeds in grid block locations containing wells that showed an interbed was missing at that location.

To determine the effect of including gaps, a simulation suite was performed where gaps were enforced in the model for three locations having a grid block that contained a well where the **B-C** interbed was known to be absent. These interbed gaps were created in the model by modifying the hydrologic properties of the entire interbed at that location so that it consisted of fractured basalt instead of sediment. Locations that had **B-C** interbed gaps superimposed in the first level of grid refinement are shown in Figure 5-58. No gaps were simulated in the **C-D** interbed because the one location where a gap has been observed is in Well M7S. Well M7S is located outside the base vadose zone simulation domain. In two out of three locations where the gaps were superimposed in the **B-C** interbed, other wells that had nonzero thicknesses were present in the grid block.

The effect on predicted risks of including these gaps is discussed in Section 6. Simulated water travel times in the vadose zone, with gaps included in the **B-C** interbed, are shown in Figure 5-59. Note that travel times are only determined for the base vadose zone domain grid, while the gaps are superimposed in the first level of refinement grid. By comparing travel times in Figure 5-59 to those shown previously for the base simulation (see Figure 5-30), the primary simulated impact is along the northern edge of the **SDA,** where water travel times are reduced anywhere from 2 to 8 years. Inclusion of the gap to the east of the SDA within the **TSA** facility causes, at most, a 2-year reduction in water travel time in the vadose zone.